

Mechanical principles of engineering fibrous tissues with programmable shape

Présentée le 9 avril 2021

Faculté des sciences et techniques de l'ingénieur
Laboratoire de Systèmes MicroBioRobotiques
Programme doctoral en biotechnologie et génie biologique

pour l'obtention du grade de Docteur ès Sciences

par

Erik MAILAND

Acceptée sur proposition du jury

Prof. A. C. Oates, président du jury
Prof. M. S. Sakar, directeur de thèse
Prof. J. Snedeker, rapporteur
Prof. A. Hughes, rapporteur
Prof. A. Persat, rapporteur

Abstract

The form and structure of biological tissues define their function. The emergence of tissue morphology during development is one of the wonders of nature. Cells mechanically probe and manipulate their surroundings while constructing structures from the extracellular matrix that they produce. Self-assembly of tissues is essentially a mechanical process, touching various engineering disciplines including solid and fluid mechanics as well as thermodynamics. Recent advancements in materials science, molecular biology, and microtechnology enabled the engineering of living tissues *in vitro* as a means to discover the physical principles of morphogenesis. The quest is far from being completed, particularly for the cases where cells are interacting through a fibrous matrix. There is no algorithm or protocol that can prescribe long-lasting shapes to these constructs with arbitrary complexity. Considering the potential impact of this endeavor in regenerative medicine and drug screening, novel perspectives are urgently needed.

The objective of this thesis is to provide an experimental and computational framework that would together enable the researcher to perform system identification and sculpturing on small scale biological samples. System identification involves dissecting the contributions of forces and motion on the evolution of the tissue shape. Sculpturing living matter means guiding the morphogenesis process through pre-programmed mechanical perturbations. Computational modeling of tissue mechanics aid both the interrogation and engineering phases. As the biological sample, a very simple composition that is based on a cell-laden collagen gel was used. Two novel technologies are introduced: (1) a fully-motorized robotic micromanipulation system and (2) a spatiotemporally resolved optochemical stimulation protocol. The platforms are integrated with modern imaging systems for real-time recording and automation.

The thesis starts with a detailed investigation of constrained fibrous microtissues where the emphasis was placed on the controlled perturbation of the mechanical state. Experiments revealed an opportunity and an important challenge. The study showed that surface stresses were as important as bulk stresses in the equilibrium configuration of the tissues. A physics-based computational model was developed that accurately captured tissue morphology by only considering bulk and surface contraction. The challenge is that tissues under the influence of these contractile stresses are inherently unstable and they are always inclined to deviate from the prescribed

shape. Epithelial tissues undergo a fluid to solid transition. In the second part, this transition was harnessed to stabilize the tissue shape and enable reshaping upon mechanically induced fluidization. Unconstrained fibrous microtissues with an epithelial shell were successfully morphed into prescribed shapes and re-shaped under the guidance of precise mechanical manipulations. The final part of the thesis suggests various future directions that would capitalize on the presented results and advance the concept towards a robust and versatile tissue engineering solution.

keywords: morphogenesis, microfabrication, mechanobiology, tissue engineering, robotic manipulation

Zusammenfassung

Die Form und Struktur von biologischen Geweben definiert deren Funktion. Die Entstehung der Gewebestruktur in der Entwicklung ist ein Wunder der Natur. Zellen erforschen und manipulieren ihre Umgebung und strukturieren die umliegende extrazelluläre Matrix, die von ihnen selbst produziert wird. Im Grunde ist die Bildung von Geweben ein mechanischer Prozess und kann mit Ingenieurwissenschaften wie Festkörper- und Strömungsmechanik aber auch Thermodynamik beschrieben werden. Neuste Entwicklungen in Materialwissenschaften, Molekularbiologie, und Mikrotechnologie ermöglichten die Herstellung von lebendem Gewebe *in vitro*, an welchen die physikalischen Prinzipien der Morphogenese erforscht werden können. Doch die Entwicklung ist längst nicht fertig, insbesondere für den Fall wenn Zellen durch eine fibröse Matrix miteinander interagieren. Es gibt noch keinen definierten Algorithmus oder ein Protokoll, mit dessen Hilfe solche Konstrukte in eine stabile Form mit gewünschter Komplexität vorhersehbar verändert werden können. Neue Ansatzweisen sind absolut notwendig, da jeder Schritt in diese Richtung grossen Einfluss für die regenerative Medizin und pharmakologische Wirkstoffforschung haben könnte.

Mit dieser Doktorarbeit wird ein sowohl experimentell als auch computersimulationsgestütztes Konzept geliefert, dass es dem Wissenschaftler ermöglicht, kleine biologische Proben als mechanisches System zu analysieren und kontrolliert in eine definierte Form zu bringen. Die Systemanalyse involviert die Untersuchung von Kräften und Bewegungen die zur Entstehung der Gewebeform beitragen. Das Formen involviert die Kontrolle über die morphogenetischen Prozesse mithilfe vorprogrammierten mechanischen Störungen. Computersimierte Modellierungen der Gewebemechanik dienen einerseits als Hilfsmittel bei der Gewebeanalyse, aber auch der Herstellung. Als biologische Probe wurde eine einfache Kombination aus Zellen, welche sich in einem Kollagengel befinden benutzt. Zwei neue Technologien wurden eingeführt: (1) ein motorisiertes robotisches System und (2) ein räumlich-zeitlich aufgelöstes optochemisches Stimulationsprotokoll. Die Technologieplattformen wurden in moderne Mikroskopsysteme integriert, welche Echtzeitaufnahme und Automatisierung ermöglichen.

Die Doktorarbeit beginnt mit der Untersuchung von mechanisch fixierten Mikro-Fasergeweben, wobei der Schwerpunkt auf der kontrollierten Störung des mechanischen Zustands lag. Mit den

Experimenten wurde eine neue Möglichkeit und eine wichtige Herausforderung erkannt. Die Untersuchungen zeigten, dass im Gleichgewichtszustand des Gewebes die Oberflächenspannung genau so wichtig war wie die Spannung im Gewebevolumen. Eine auf Physik basierende Computersimulation wurde erstellt, welche die Form des Gewebes nur unter der Berücksichtigung der Kontraktionskräfte an der Oberfläche und im Gewebevolumen bestimmen kann. Die Herausforderung ist, dass diese Kontraktionskräfte die Gewebestrukturen an sich instabil machen und die Gewebe immer von der vorgegebenen Form abweichen. Epithelialgewebe haben die interessante Eigenschaft, dass sie von einem eher flüssigen in einen eher festen Zustand übergehen können. Im zweiten Teil wurde dieser Übergang genutzt um die Form des Gewebes zu stabilisieren und durch mechanisch induzierte Verflüssigung wieder zu deformieren. Unbefestigte Mikro-Fasergewebe umrunden von Epithelialzellen wurden erfolgreich geformt und mithilfe präziser mechanischer Manipulationen deformiert. Der letzte Teil der Doktorarbeit schlägt verschiedene zukünftige Richtungen vor, wie die gezeigten Resultate und fortgeschrittenen Konzepte als vielseitige und robuste Lösung bei der Züchtung von Geweben genutzt werden könnten.

Schlüsselwörter: Morphogenese, Mikrofabrikation, Mechanobiologie, Gewebezüchtung, Roboter-manipulation

Acknowledgments

I would like to express my sincere gratitude to my thesis advisor Prof. Selman Sakar. He was supportive throughout my entire PhD and always available to discuss new ideas, find solutions for problems, or simply discuss science. He built up an unique multidisciplinary research environment and brings an immense dedication and expertise for science combined with optimism and an open mind. I'm very grateful for the opportunity and trust he was giving me, which allowed me to grow as a scientist and as a person. Also I would like to thank Prof. Nikolaos Bouklas, who was always available for scientific discussions in our collaborative work.

Moreover, I would like to thank Prof. Jess Snedeker, Prof. Alex Hughes, Prof. Alex Persat and Prof. Andy Oates for dedicating their time and expertise to review my work.

My time in the laboratory would have not been as fruitful and fun without all my colleagues from MICROBS. I would like to thank all of you. Matthias Rüegg, for your scientific help, a great collaborative work, as well as climbing and other social events. Lucio Pancaldi, for all your valuable inputs and our discussions about science and everything else. Ece Ozelci, for a fruitful collaboration and great discussions. Fazil Uslu, for a great work together and many philosophical discussions at tennis and breakfast. Raquel Parreira, for the bio and chemistry support and countless coffee conversations. Murat Kaynak, for all scientific discussions and sharing the office together. Haiyan Jia, for a great collaboration and all scientific discussions.

Many students helped me in my PhD project and I would like to thank for their excellent work. Special thanks to Alex Horvath, Gregoire Repond, Ece Yildiz, Quentin Wannebroucq, Ece Su Ildiz, Jon Märki, and Odysseas Chaliotis. Microscopy was a critical part in my project and I would like to thank the Bioimaging and Optics Platform team and the members from the Oates lab for their help.

Also I would like to thank all my friends beyond the laboratory, that all had an important part during my education and are still around today. Thank you Timo Rey, Thomas Franc, Severin Etzensberger, Nathan Baumli, Patrick Helbling, Johanna Diener, Claudia Peter, and Nina Merdas.

Thank you Marco Mailand, Susanne Mailand, Timo Rey, Lucio Pancaldi, and Soham Basu for

your endless scientific support and proof-reading this work.

Very special thanks go to Margaux Dastor, a wonderful person who continuously supported me throughout my entire PhD and helped me to grow not only as a person, but also as a scientist. This work would have not been possible without her.

Finally and most important, I'm deeply grateful to my family Irene Mailand, Marco Mailand, Susanne Mailand, and Thomas Zraggen. From the very beginning you were supporting every step I am taking and believe in my future plans. Thank you very much for always being here.

Contents

Abstract (English/Deutsch)	iii
Acknowledgments	ix
Contents	xi
List of Figures	xiv
1 Introduction	I
1.1 Problem Statement	I
1.1.1 General Objectives and Approach	4
1.2 Organization of the Thesis	6
2 Background	7
2.1 Mechanotransduction	8
2.2 In vitro Models to Study Mechanics of Tissue Morphogenesis	10
2.2.1 Epithelial Monolayers	11
2.2.2 Mesenchymal Tissues	12
2.3 Phase Transitions During Morphogenesis	14
2.4 Physical Models of Morphogenesis	15
2.4.1 The Liquid	17
2.4.2 The Colloidal Soft Material	18
3 Robotic Micromanipulation Platform	21

3.1	Introduction	23
3.2	Robotic Micromanipulation System	24
3.2.1	Concept	24
3.2.2	System Validation	30
3.3	Optochemical Control over Cell Viability	31
3.4	3D Live Imaging during Robotic Manipulation	32
3.5	Discussion	34
3.6	Technical Details	38
4	Surface and Bulk Stresses Drive Morphological Changes in Fibrous Microtissues	41
4.1	Introduction	43
4.2	A New Equilibrium Theory for Contractile Microtissues	44
4.3	Results	48
4.3.1	Shape Evolution of Fibroblast-Populated Collagen Microtissues	48
4.3.2	Finite Element Simulations Capture (Re)Shaping of Microtissues	52
4.3.3	Elastocapillary Length and Boundary Restoration	55
4.3.4	Activity of the Fibroblasts at the Wound Edge is Indispensable for Closure	56
4.3.5	Shape Restoration at the Tissue Periphery	59
4.3.6	3D Finite Element Simulations Capture 3D Shaping of Microtissues	61
4.4	Discussion	62
4.5	Materials and Methods	66
5	Tissue Sculpting by Mechanically Induced Solid-Fluid Transitions	69
5.1	Introduction	71
5.2	Results	73
5.2.1	Fluid to Solid Transition Stabilizes Engineered Tissue Morphology	73
5.2.2	Slip Casting and Plastic Forming	76
5.2.3	Subtractive Sculpturing using Plastic Microsurgery	77
5.2.4	Assembling Complex Tissues from Building Blocks	78
5.2.5	Tissue Folding Through Spatially Patterned Cell Death	81
5.3	Discussion	83

5.4	Materials and Methods	85
6	Conclusion and Future Work	89
6.1	Conclusion	89
6.2	Future Work on Biomanipulation	91
6.3	Future Work on Mechanobiology	93
6.4	Future Work on Engineered Morphogenesis	94
	Bibliography	95

List of Figures

2.1	Cells residing on or within a fibrous matrix	10
2.2	Biological tissues show fluid-like behavior	16
3.1	6-DOF robotic micromanipulation system	25
3.2	Schematic illustration of the software architecture and controller	28
3.3	Teleoperated manipulation and automated repetition of motion	30
3.4	Plastic surgery to repair a sidecut in tethered collagenous microtissues	32
3.5	Spatiotemporally controlled photoconversion of blebbistatin and cell death in microtissues.	33
3.6	Light sheet microscopy for 3D live imaging	34
3.7	Smart actuated hydrogel allows gripping and placing of microtissues	35
3.8	Microtissue manipulation over a long duration of time	36
3.9	Spatiotemporal controlled protein localization in single cells	38
4.1	Engineered 3D fibrous microtissues display fluid-like behavior	49
4.2	Experimental platform	50
4.3	Closure of incision wounds and damage-free holes	51
4.4	Predicted microtissue shapes resemble empirical observations	54
4.5	Deactivation of surface effects in the experiments and simulations	56
4.6	Deactivation of surface effects during tissue formation	58
4.7	Surface stresses drive restoration at the tissue periphery	60
4.8	3D simulations and reconstructed images of 3D fibrous microtissues	62
4.9	Tissue architecture suggests the presence of surface stresses	63

5.1	Self-assembly of capsule-shaped microtissues	73
5.2	Stability of engineered microtissues	75
5.3	Slowdown of cell motion in MDCKII monolayer	76
5.4	Slip casting and plastic forming of microtissues	77
5.5	Plastic microsurgery and microtissue assembly	78
5.6	Tissue folding through cell death	80
5.7	Cell extrusion in monolayers on flat collagen substrates	82
5.8	Traction forces at the wound edge lead to tissue folding	83

Chapter I

Introduction

I.1 Problem Statement

Living cells actively change the structure and mechanics of the tissues that they built in response to biochemical and mechanical signals. This out-of-equilibrium assembly process endows living matter with almost unlimited shaping capability. During embryogenesis, a microscale agglomerate of stem cells grows and morphs into a highly structured and compartmentalized body with extraordinary functionality. In addition to cells, the other main constituent of embryonic tissues is the extracellular matrix (ECM) - a fibrous net produced and organized by the cells. Cells have the ability to move with respect to the tissue or remodel the surrounding matrix, depending on the state of the cells and the ECM. As a result, they can populate the matrix (e.g. stroma) or spread on an underlying matrix (e.g. basement membrane), as individuals or as multicellular collectives. The mechanical interactions among cells through tight junctions and cell-ECM interactions guided by mechanosensitive proteins such as integrins define the boundaries and mechanical properties of the self-assembled tissues.

Discovering the physical principles of cell-cell and cell-ECM interactions underlying tissue motion and deformation is not only instrumental for understanding morphogenesis. These principles may aid the development of novel methods for tissue engineering and regenerative medicine. Experiments with living embryos provided key information on the complexity and robustness

of morphogenic processes. Nevertheless, making precise perturbations and sensitive measurements in a well-controlled environment is essential to pinpoint the contributions of each physical mechanism. Recent advancements in microtechnology, materials science, molecular biology, and optics introduced *in vitro* platforms that recapitulate many aspects of embryonic development and pathogenic conditions such as cancer that abruptly trigger morphogenic programs in adult organs. The field has reached the point where physics-based computational models manage to accurately predict experimental observations.

The research in the mechanobiology of morphogenesis has primarily focused on tissues in the form of two-dimensional (2D) monolayers (e.g. epithelium) on a planar substrate or three-dimensional (3D) cell clusters (e.g. spheroids, cysts, acini, and organoids) that are embedded in a hydrogel (e.g. Matrigel). Microfabrication enables precise control over the distribution and geometry of the cell clusters while material science provides static or dynamic control over the substrate. Synthetic and reconstituted natural hydrogels are extensively used due to their tunable properties and ease of production. One important configuration that has been overlooked is the case where the size of the tissue is in the microscale and, as a result, the cells residing on or inside the gel can deform the gel in bulk. This scenario is quite relevant to embryogenesis. When the gel is fibrous and macroporous (e.g. collagen), several nonlinear mechanical phenomena may take place such as fiber recruitment and alignment, viscoplasticity, and long-range multicellular communication and organization. Collagen is the main structural protein in the ECM of connective tissues, making it the most abundant protein in mammals, making up from 25% to 35% of the whole-body protein content.

The study of the mechanics of (un)constrained microscopic fibrous tissues has several peaks and a few challenges. The challenges will be described in detail in the following sections. The advantages that come with the small size are:

- The characteristic dimensions allow the diffusion of nutrients and small molecules into the core of the tissue. Therefore, cells can stay alive everywhere within the tissue and their action plays a role in the shaping process. Furthermore, molecular agents and pharmaceuticals can reach all the cells.
- The cells and the surrounding matrix can be visualized in real-time using fluorescent mark-

ers or optical techniques such as second harmonic generation.

- Many tissue samples can be studied in parallel and various conditions can be tested with high throughput.

1.1.1 General Objectives and Approach

The overall objective of this thesis is to develop a methodology for engineering microscale fibrous tissues in any desired shape with long-term stability. One of the grand challenges in the field is to enable the cells to organize following their natural programs while prescribing a form and function to the construct with the aid of materials and external perturbations in a deterministic way. Addressing this challenge is important because the shapes prescribed using traditional manufacturing techniques such as 3D printing are not in equilibrium and cellular activity almost always disrupts the shape towards a more symmetric and less functional configuration. Scientists in this field have been developing tools to control the properties of the microenvironment; decorating matrix proteins with various ligands, using morphogens or growth factors to differentiate cells in space and time, and engineering biomaterials with tunable properties. In this thesis, I focus on the mechanical factors, specifically on the boundary conditions and external mechanical loading, as a means to trigger multicellular events that would change the distribution of forces within the tissue and as a result, morph the tissue. To be more specific, I aimed to discover a methodology that would fluidize the tissue for freeform shaping and solidify the tissue to preserve this shape until the next shaping episode.

Various tools and techniques must be invented that would aid the discovery of the dominant physical forces that act to shape the fibrous tissues and control these forces to guide the shaping process. The work is built upon recent advances in microengineering, particularly photolithography and replica molding, and medical robotics. Established methods are used to cast biomaterials with desired geometry and boundary conditions. Time-lapse and confocal microscopy are routinely used throughout the project to make morphological and structural characterizations. The main technical challenges the thesis aims to address are:

- Handling and mechanical testing of microscopic biological samples with precision and dexterity. To this end, the advancements in robotics and automation are explored. The robotic end-effectors are inspired by commercially available tools developed for ophthalmic and neuro microsurgery or tools made by researchers working with embryos.
- Aside from mechanical perturbations, a proper protocol to mechanically (de)activate or kill cells without disrupting the ECM is required. To this end, optogenetic and optochem-

ical methods are explored.

- A computational modeling framework is necessary to learn physical laws from empirical data. Computational models also suggest specific experiments to extract important parameters and decouple the effects of different forces or biological processes. I aim to develop a continuum framework that calculates mesoscale forces and large deformations without dealing with extensive computation time or losing the biological relevance.

1.2 Organization of the Thesis

The following chapters are organized to highlight the three major contributions of the presented work. The tissue sculpturing paradigm presented in chapter 5 relies on the technological and scientific accomplishments presented in chapters 3 and 4 as well as the work of others in the field summarized in chapter 2. In chapter 2, I review the literature to answer the following question: If we have contractile cells (epithelial or mesenchymal in origin) distributed inside or around a collagenous microtissue, what do we expect to observe in the course of morphogenesis? Cells are mechanical machines that can move inside or on top of fibrous substrates, they can remodel their surrounding matrix, and they can attach to each other to form multicellular structures such as cysts and tubes. The cellular response is tightly regulated by internal control systems and executed by molecular machinery, all made out of proteins. After introducing the capabilities of cells, I summarize *in vitro* platforms developed for studying tissue mechanics, specifically gap closure and tissue compaction. I summarize modeling efforts and proposed physical laws. In chapter 3, a robotic manipulation platform is presented that can mechanically perturb and probe microtissues. Furthermore, a novel optochemical method is described that initiates spatiotemporally resolved cell death upon blue light illumination. The platform is tailored for future integration with a fully automated light-sheet imaging system allowing real-time 3D visualization. In chapter 4, we study the mechanics of constrained contractile microtissues under mechanical perturbations. This work led to the discovery that fibroblasts at the surface may generate high enough stresses that deform the bulk tissue according to an elastocapillary length scale. The results have shown that, analogous to the fluid-like behavior of cellular aggregates, surface stresses manifest in fibrous microtissues. We explored the origin and shaping power of surface effects, which led us to the development of the methodology presented in chapter 5. We have also developed a continuum model that considers bulk contraction and surface forces, building the foundation for a computational framework to design experimental manipulations that would generate tissues with desired shapes. In chapter 5, we introduce a set of novel manufacturing methods that harnesses the reversible phase transitions of an engineered epithelial shell. Similar to granular media, we apply mechanical inputs to locally fluidize the layer and reshape the tissue. Implications of these discoveries and work that must be done to generalize the results are discussed in chapter 6.

Chapter 2

Background

Every tissue engineering approach must consider the needs and respect the dynamics of the living matter. Otherwise, the engineered tissues are doomed to lose their structure and, as a result, their intended function. In this thesis, I aim to establish a technique that harness and guide self-organization principles of cells. Thus, it is essential to start with a review of tissue mechanobiology, a field that investigates physical interactions among cells as well as between cells and the surrounding ECM.

Morphogenesis, the shaping of biological tissues, plays a crucial role during embryonic development. As an important remark, adult cells do not completely lose the ability to perform morphogenesis. Indeed, morphogenic events are triggered during regeneration and cancer. Our understanding of multicellular sculpturing of biological tissues is based on the experiments performed in all these three fields of research (i.e. development, regeneration, cancer). Cells are highly complex microscopic machines that can move, apply contractile forces, and construct scaffolds from fibrous ECM [1]. A major difference between man made buildings and tissues is that these scaffolds are continuously remodeled [2]. These structural processes are guided by biochemical signals and physical cues [3]. The chapter starts with a brief summary on the cells as mechanical agents of morphogenesis. Later, *in vitro* models and microengineering approaches to study the mechanics of morphogenesis are introduced. Finally, experimental observations regarding mechanics of various morphogenic events and associated physical models are explained.

2.1 Mechanotransduction

Cells physically interact with the structures around them using a complex protein machinery that includes the actin cytoskeleton, myosin as molecular motors, membrane proteins that are responsible for transmitting and sensing mechanical loads (such as channel proteins, cadherins, and integrins), and intracellular proteins that process signals and regulate the cellular response such as Rho GTPases and transcriptional regulators.

Actin filaments are composed of polar monomers that constantly polymerize and depolymerize to form complex branched networks. These networks define the overall cell shape. During cell migration, directed actin polymerization pushes the membrane forward causing rearward motion and retrograde actin flow. A large number of associated helper proteins coordinate spatial network dynamics [4]. Myosin II is a molecular motor that actively moves along actin filaments. Assembled as oligomeric structures, the motors can attach to, bundle, and pull on actin filaments [5]. Aside from pulling on or pushing the neighboring cells or fibers, contractile forces generated by the actomyosin network regulate the cell shape and stiffness [6].

Transmembrane adhesion molecules connect cells to each other or to the surrounding ECM. Cell-cell adhesion is mediated by tight junctions that transmit forces. Connections are strengthened by force application and subsequent stiffening of the actomyosin network. Cell-cell junctions, in particular cadherin-mediated adherens junctions, endow tissues with cohesion energy and surface tension [7, 8]. The adhesion to the ECM is mediated by integrin-family proteins, which bind to characteristic peptides on ECM polymers. Similar to cell-cell junctions, these transmembrane molecules physically connect the actomyosin network to the external world for force transmission. Adhesion sites get mature and form focal adhesions that are micrometer-scale clusters of integrins. The emergence of focal adhesions coincides with the formation of densely packed actomyosin structures called stress fibers. This positive feedback leads to actin filament accumulation in direction of maximal tensile stress. The dynamic link between adhesion strength and actomyosin maturation is known as the molecular clutch [9].

The conversion of forces into biochemical signals allows cells to sense mechanical cues including substrate stiffness and tensile loading. Mechanosensitive adaptor proteins such as talin, vinculin

and lamin are coupled to integrins and unfold when force is applied. Unfolding leads to the exposure of hidden peptide sequences, which triggers interactions with downstream proteins. In a similar way, stretch-activated transmembrane ion channels such as piezo-family proteins are activated upon the application of tensile forces. The subsequent influx of ions, such as Ca^{2+} , results in conformational changes of effector proteins. These events initiate downstream signaling that eventually leads to the translocation of transcriptional regulators (such as YAP) into the nucleus. Up- or downregulation of gene expression by transcriptional regulators modulate the activity of Rho GTPases such as RhoA and Rac1. RhoA and its effector ROCK control myosin II activity through phosphorylation. Moreover, Rac 1 mediates the formation of lamellipodia, and together with RhoA, controls cell migration. A biochemical process that transforms forces into biochemical signals is referred to as mechanotransduction. Mechanotransduction not only leads to immediate changes such as spreading, migration, and ECM remodeling, but also leads to long-term important commitments including proliferation, death, and differentiation [10–12].

Different cell types, displaying distinct organization of the intracellular machinery, show distinct interactions with their surroundings. Epithelial cells form two-dimensional sheets by directly attaching to each other through cadherin mediated cell-cell adhesions. Furthermore, these cells display an apico-basal polarity whereas the basal side of the cells is attached to a basement membrane made out of ECM. These monolayers cover the surfaces of every organ and cavity, and serve as barriers and maintain integrity. On the other hand, mesenchymal cells do not like to attach to each other and instead they invade, produce and interact with the ECM [13]. Mesenchymal tissues condensate to form muscle, tendon, cartilage, tooth, or bone or remain as interstitial tissues that fill the mesodermal space to connect and support organs [14]. Considering a fibrous gel, such as collagen, epithelial cells will attach to each other and cover the surface, whereas mesenchymal cells are expected to reside inside (Figure 2.1a). These generic principles will be the basis of a much richer repertoire of morphogenic programs that are explained in the following section.

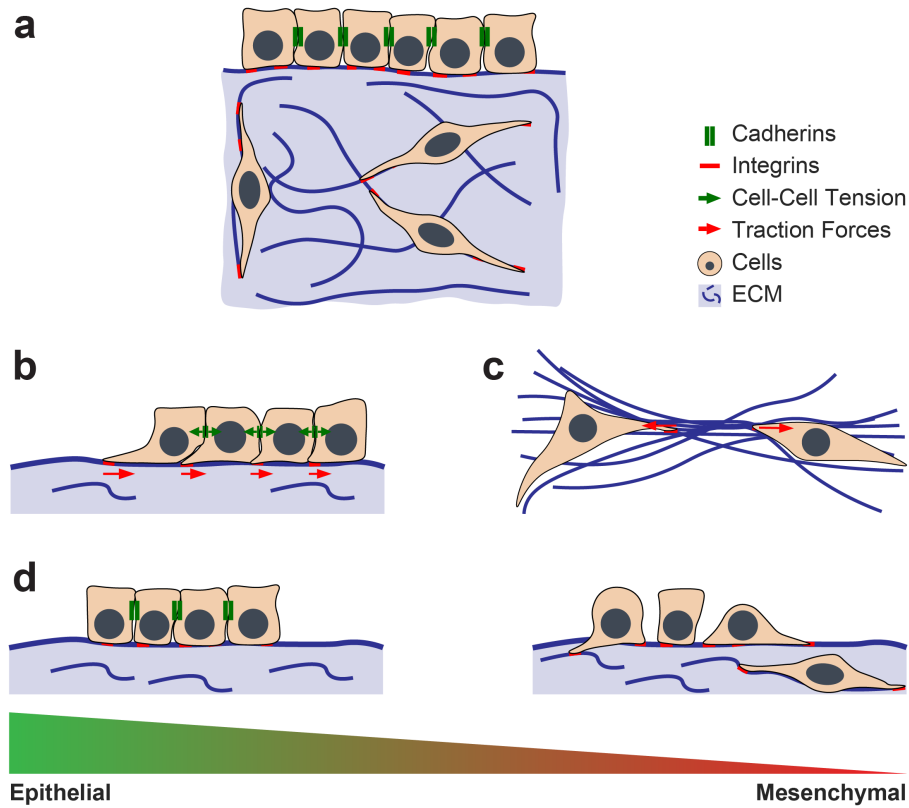


Figure 2.1: Cells residing on or within a fibrous matrix. (a) Epithelial cells can form coherent monolayers on surfaces. They attach to the surface by integrins and adhere to each other by cadherin mediated cell-cell junctions. Mesenchymal cells can reside within the fibrous matrix, attaching to fibers via integrins. (b) Epithelial cells apply traction forces on the substrate to migrate and maintain integrity via contractile intercellular forces. (c) Mesenchymal cells apply traction forces on the fibers and reorganize it. (d) Epithelial and mesenchymal cell states can be seen as the extremes of a continuous transition. Green indicates the epithelial cell state with cells attaching to each other and displaying an apico-basal polarity. Red indicates the mesenchymal cell state with cells invading, producing and interacting with the ECM as single agents.

2.2 In vitro Models to Study Mechanics of Tissue Morphogenesis

An effective way of studying the mechanics of morphogenesis is reducing the complexity and focusing on a single multicellular process at a time using *in vitro* cell culture systems.

2.2.1 Epithelial Monolayers

In a number of morphogenic events, cohesive epithelial sheets move over or along with a provisional fibrous substrate [15]. Notably, the epithelium seals gaps spontaneously occurring during development, during dorsal closure in *Drosophila*, eyelid closure in mouse, or ventral enclosure in *C. elegans* [3]. The closure of gaps in embryonic tissues has been extensively studied because the closure is perfect that leaves no scar tissue behind. The associated conditions are expected to provide critical insights for wound healing in adult tissues. In the context of this thesis, these studies are relevant because they reveal certain aspects of epithelial morphogenesis.

State-of-the-art 2D *in vitro* culture models are sophisticated enough to recapitulate epithelial morphogenesis. The model systems allow precise control over tissue boundaries and geometry through various microengineering techniques such as microcontact printing of ECM proteins [16] and microfabricated elastomer stamps [17]. Well-controlled mechanical perturbation has been applied such as scratching [18], laser ablation [19], or tensile stretch [20]. Tissue dynamics have been assessed non-invasively using time-lapse microscopy and fluorescence labeling. Traction force microscopy (TFM) reported traction forces from the deformation of linearly elastic substrates with calibrated rheology [21].

In vitro studies revealed that epithelial monolayers collectively migrate towards uncovered areas on an adhesive substrate. Collective migration is governed by the balance of mechanical stresses acting at the cell interfaces and between cell and the substrate [22–25]. Leader-like cells extend their lamellipodia towards the protruding edge and show polarized morphologies with stress fibers and focal adhesion alignment towards the free edge. Together with this morphological changes, mechanical traction and intercellular stress are the highest at the protruding edges. Forward motion occurs because the tissue needs to balance the internal stresses. The protruding edge moves forward by pulling itself along the substrate, a mechanism referred to as cell crawling [19, 22] (Figure 2.1b).

Early work on a variety of model organisms indicated that these contractile forces of the epithelial tissues are critical for skin wound closure [26, 27]. However, it is not cell crawling but the purse-string mechanism that drives closure in embryonic tissues. Namely, the cells at the border are connected by a supracellular actomyosin ring leading to multiscale contractile forces [28, 29].

In adult tissues, cells migrate on the adhesive dermal layer by lamellipodia-driven crawling at the onset of wound closure. At later stages during the healing process, cell crawling correlates with an actomyosin ring at the leading edge [30]. *In vitro* studies revealed that the presence of a supracellular actomyosin cable and closure dynamics depend on curvature of the gap and can be present on adherent or non-adherent gaps [16, 17]. The actomyosin cable generates tensile forces tangentially to the edge and pulls cells towards the gap in a purse-string manner [19]. The relative contributions of the two mechanisms have been shown to depend on substrate stiffness, actomyosin composition, and focal adhesion stability [31]. Similar to gap closure, cortical tensions of epithelial cells surrounding a dying cell are elevated for dead cell extrusion. This process has been shown to be driven either by cell crawling or the purse-string based mechanism depending on monolayer cell density [32, 33].

Both, wound closure and collective cell migration have been associated to the reduction of internal stresses and tissue fluidization, defined by the increase of cell rearrangements and loss of cell-cell junctions [25, 34]. The concept of fluidization will be discussed in the following sections. Interestingly, not only in gap closure but also collective migration, a supracellular actomyosin cable forms at the leading edge, most likely to stabilise plasticity of directional migration [35].

In early development these morphogenic processes together with asymmetric contractions of cells within the monolayer apply significant forces to shape the soft embryo. A variety of *in vitro* models were developed where epithelial cells are guided into 3D structures within a hydrogel [36, 37]. We are only starting to explore tissue mechanics of shape emergence in these systems.

2.2.2 Mesenchymal Tissues

At later stages in development, the fibrous tissue forms a stable network connecting epithelial sheets. Shape emergence and maintenance relies on the continuous interaction between the two constituents. Local accumulation and contraction of freely migrating mesenchymal cells influences the adjacent epithelial layer and can drive tissue morphogenesis [38]. Epithelial skin wound closure is supported by traction forces generated by the cells in the underlying mesenchyme [39, 40]. Furthermore, skin hair-follicle folding in bird is initiated by the aggregation and contraction of mesenchymal cells [41]. Foldings during intestinal villi and tooth formation in mouse are crit-

ically influenced by the aggregation of mesenchymal cells [42, 43]. In chick, developed smooth muscle layers generate compressive stresses critical for intestinal vili formation [44].

To study the interactions between cells and ECM, cells are encapsulated within soft 3D hydrogels mainly composed of reconstituted collagen type I due to the abundance of collagen in connective tissues [45–48]. Cells attach to, and contract the fibers which leads to tissue compaction [49–51]. Remarkably, fiber interaction allows mesenchymal cells to transmit forces over longer distances and collectively remodel the tissue. Likewise, the mechanical properties and boundary conditions provided by the ECM critically influence cell behavior. When cells pull on and align fibers, the matrix plastically deforms and stiffens, which in return, promotes cell polarization and emergence of collective tissue tension [52, 53] (Figure 2.1c). The degree of strain-induced fiber alignment and matrix stiffening critically influences long-range force transmission within the network [54]. When the collagenous tissue is free-floating, it compacts into an isotropic sphere whereas cells generate tensile circumferential stresses at the periphery and compressive stresses in the center [55]. However, fibrous tissues *in vivo* are attached to their surrounding and are often under mechanical load. To mimic this conditions, pioneering work showed that the compaction event can be constrained by adding pins [56]. Introduced boundaries dictate fiber alignment and distribution of tissue tension. Uniaxially constrained gels show mechanical anisotropy due the alignment of cells and ECM along the direction of the pillars, mimicking the architecture of muscle and tendon. Biaxially constraint gels remain in the center mechanically isotropic and resemble flat tissues such as skin [57]. Advancements in microfabrication led to the design of microscale pillars, which enabled the engineering of large numbers of microscale fibrous tissues under tension enabling cell resolution imaging [53]. The model system is relevant in this thesis and will be introduced in chapter 5.

Understanding how cell-generated forces within the fibrous matrix drive tissue deformations potentially allows predictable design of complex free-standing tissues. Considering a collagenous gel with cells residing within, the tissue contracts in a way that depends on cell number and distribution. Initial work has been done to quantitatively describe this evolution, laying a foundation for potential 3D bioprinting in space and time [58, 59]. Remarkable precise prediction over fibrous tissue shaping has been achieved by prepatterned islands of contractile mesenchymal cells within

a collagen gel. Attachment sites for cells are printed on a solid substrate using DNA-programmed assembly of cells prior adding a collagen layer. Upon release, cells locally contract the gel leading to predictive folds [38]. The technology to predefine strains within the collagen gel has been used further to guide the self-organisation of epithelial tubules over longer distances along forming grooves [60]. This technology holds great promise as it potentially combines the advancements of 3D bioprinting and cellular self-organization guided by reconstituted embryonic cues.

During embryonic development, epithelial and mesenchymal morphogenic programs are coupled, which generates a greater diversity of morphologies and functionalities.

2.3 Phase Transitions During Morphogenesis

Cells display a very particular feature during embryonic morphogenesis. They can switch from epithelial to mesenchymal character on-demand to seamlessly change shape like a fluid and stabilize that shape against deformations like a solid. A solidification of the tissue preserves its elastic energy, which is important to maintain shape and integrity. On the other hand, mechanical instabilities at the tissue boundaries lead to anisotropic stresses, which drive tissue flow and shaping. The mechanical property of the embryonic tissue is largely defined by the strengths of cell adhesion and cell contraction. This will be discussed in more detail in the following section. The epithelial and mesenchymal cell states can be seen as the extremes of a continuous spectrum where epithelial-to-mesenchymal transition (EMT) may also occur partially (pEMT) (Figure 2.1d). In the intermediate states, migrating cells are not fully isolated and remain connected with their neighbors through strong or weak cell-cell junctions. Weak front-rear polarity can be attained, while maintaining partial apico-basal polarity [61]. A number of hybrid epithelial-mesenchymal phenotypes have been described in the context of development, fibrosis, malignant progression of tumors, as well as wound healing [61–66]. Hybrid epithelial-mesenchymal phenotypes have been associated with gap closure and collective migration, which we have seen are related to tissue fluidization. So far the focus was on these specific events, but the dynamic regulation of mechanical properties and fluid-like behavior enables much more versatile and complex shaping events.

Changes to a fluid-like behavior have been proposed not only during wound closure in fly, but

also body elongation in fish [67–69], and gastrulation in frog and fly [70, 71]. When showing fluid-like behavior, adjacent tissues can influence each other analogous to how a drop of water remains round in air but spreads when touching a surface. A surrounding epithelial layer of the mesoderm has been shown to regulate interfacial tensions for tissue elongation in frog [72]. Similarly, in fish epiboly the deep cell mass fluidizes to undergo rapid deformation. Differences in interfacial tensions drive a flow-like movement of an adjacent epithelial layer spreading over the deep cell mass [73–75]. Importantly, ECM components may displace together with cells and contribute to tissue motion while providing structural attachment points for the transmission and equilibration of forces [2, 76–78]. The ECM critically contributes to the mechanical environment as well as balance of stresses during notochord elongation in frog. Displaced components are deposited at the surface and provide attachment points for cells, which leads to a solid-like transition critical for directional elongation [79–81]. Such mechanism has not only been observed in frog but also in fish [82]. Aside from structural components, somite formation in fish is the result of both cell-cell and cell-ECM differential interfacial tension [83, 84]. In fly, ECM components have been reported to provide attachment points and geometrical cues for not only robust tissue elongation but also folding [85–87]. Finally, also during gap closure, specifically in eyelid closure in mice, the underlying ECM provides attachment points for the transmission of forces [88].

The mechanical regulation of a solid-like to fluid-like behavior and vice-versa is clearly a recurrent phenomenon during morphogenesis. With the aim to shape a microscale fibrous tissue, this has to be taken into account. It is important to note that fibrillar network composition and degree of crosslinking strongly influence mechanical properties and the transmission of local cell deformations on tissue motion [89]. How exactly tissue mechanical properties are defined will be discussed in the last section.

2.4 Physical Models of Morphogenesis

Biological tissues are highly dynamic and constantly adapt their mechanical properties in space and time. It is largely unknown at which time and length scales these changes emerge as well as the underlying key molecular drivers. However, the rheology of living matter, defined by the

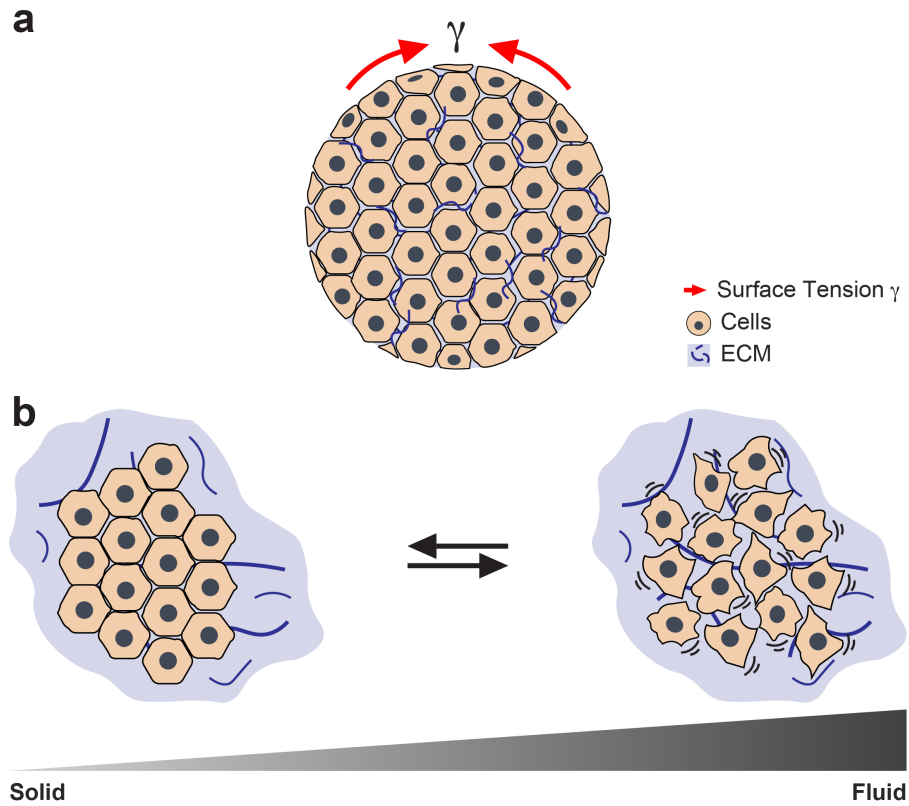


Figure 2.2: Biological tissues show fluid-like behavior. (a) Active forces in multicellular tissues result in surface tension γ . (b) Groups of cells can reversibly switch from solid-like to fluid-like behavior.

fluctuations of cell activity and collective dynamics, may be traced back to established physical and mechanical principles.

The living tissues are generally considered to be viscoelastic [90–92]. In cell clusters, tissue mechanics are regulated by cell cohesion [93], cell contraction [94], and other active processes, such as cell division and extrusion [95]. In presence of the ECM, the structural changes within the fibers as well as the degree of crosslinking, entanglements, and overall porosity of the network influence the mechanical properties [91]. On one extreme is the solid response where the deformation energy can be stored and immediately recovered. On the other extreme is the viscous response, where the energy is dissipated over time, leading to stress-relaxation and viscous flow. Depending on the time scale and the material composition, tissue response can be categorized from elasto-visco-plastic to viscoelastic liquid. Cells as well as the ECM networks show non-linear elasticity [96, 97], which is believed to protect the tissue from damage that could otherwise

be induced by large deformations.

2.4.1 The Liquid

One recurring physical concept that captures the behavior of single cells as well as cell clusters is surface tension. Surface tension (interfacial tension) represents the tendency of two adjacent materials to reduce their contact area. Expressed as energy per unit interface area (in joules per square meter), surface tension describes the excess of free energy due to the imbalance of attracting forces of the molecules at the surface. Surface tension can also be described as a force acting parallel to the interface with the tendency to reduce the area. The force is proportional to the surface area and expressed in newtons per meter. Single cells minimize their mechanical energy by balancing the surface and bulk tension in the course of attachment to surfaces, including other cells [98]. Multicellular tissues self-organize into an energy-minimizing shape dictated by the interfacial tensions, resembling a soap bubble cluster (Figure 2.2a). Analogous to coalescing droplets or wetting of surfaces, cell populations sort, fuse, and spread over surfaces. The morphological outcomes are dictated by the competition between interfacial tensions between cells within a population and their surrounding [99–101]. Surface tension of multicellular aggregates has been quantified by assessing tissues equilibrium shape after centrifugation, parallel microplate compression, or micropipette aspiration [90, 99, 102]. Using different methods and type of tissues, surface tensions have been measured ranging from 0.05 to 56 nN mm⁻¹ [103]. Two kinds of interfacial energies contribute to tissue surface tension in multicellular tissues: the adhesion tension γ_{Γ} that promotes attachment via cadherins, and the cortical tension β that promotes cell ‘rounding’ due to contraction of the cortical cytoskeleton [8, 104]. Cortical tensions are different at free surfaces β_S and cell contact surfaces β_C and the contribution to overall surface tension can be described as $\gamma_{\beta} = \beta_S - \beta_C$ [103]. Tissue surface tension can therefore be defined as $\gamma = \gamma_{\Gamma} + \gamma_{\beta}$. Tensions that can be generated by only cadherin mediated adhesions are ten to hundred fold less than the lowest measured tissue surface tensions. Thus their role may be more a regulatory one through increasing cell-to-cell contact area and decreasing with it β_C [103]. Different than liquids, the wetting of cell aggregates on a surface does not only depend on the competition between cell-substrate and cell-cell adhesion energies, but also on the competition between traction forces and intercellular stresses [105]. Consequently not only ECM composition but also stiffness can influ-

ence interfacial tensions. With the incorporation of ECM components, biological tissues show more solid-like behaviour [106]. Especially when the ECM is present as large collagenous bundles, tissues show mainly a solid character with elasto-visco-plastic properties. Interestingly, *in vitro* experiments showed that the growth and morphology of engineered collagenous tissues can also be described by the rules of fluids [98, 107, 108]. It has been postulated that cellular forces generate surface stresses, and together with active remodeling of the ECM provide the tissue with a fluid-like behaviour. However, very little is known about the underlying mechanism of surface stresses in fibrous tissues and will be further discussed in the following chapters.

Overall, biological tissues show analogies to liquids and exert surface tensions. However, a fundamental difference is the active contractile forces of cells.

2.4.2 The Colloidal Soft Material

To account for the transition from a fluid-like to a solid-like behavior, tissues are modeled as complex disordered soft materials such as granular materials, polymer networks, liquid crystals, and colloidal suspensions [25, 101, 109]. Disordered soft materials can solidify into amorphous solids where no structural order is apparent, a phenomenon that has been extensively studied in glass [110]. A variety of colloidal soft materials display similar behavior through aggregation or gelation. Temperature, mechanical loading, particle density, and adhesion of particles are the variables that regulate the transition state.

Freely migrating cells can collectively reduce their motility and enter a dynamic arrest without any structural order [25] (Figure 2.2b). The jamming transition has been shown to be dependent on cell motility along with cell adhesion and cortical tension. Cell shape and alignment are therefore an indicator of tissues phase [111–113]. Unjamming has commonly been associated to EMT and pEMT due to striking similarities. However, a recent work has shown that chemically-induced pEMT is distinct from the mechanically-induced jamming transition [114].

Computational models consider tissue dynamics spanning from cellular to supracellular scales and are classified as agent-based models, interfacial models, and continuum models [115, 116]. Epithelial monolayers were mainly simulated using agent-based models (such as vertex, voronoi, and potts models) to recapitulate cell-cell interactions. The interfacial energies are considered in

interfacial models (such as phase-field models), whereas the tissue is described as viscous fluid. Continuum models are the common choice for fibrous tissues where the tissue is treated as a continuous bulk material defined by constitutive laws that enable the incorporation of active contraction and non-linear properties of the ECM [117, 118].

The goal of this thesis is to engineer fibrous tissues into defined shapes by using the self-organization capabilities of cells. It has to be taken into account that cells can reside on the gel and apply traction forces or on the other hand, reside within and reorganize the fibers. The choice of cell type will critically influence the outcome, whereas changes in cell behavior induced by mechanical interventions will also have to be accounted for. A solid-like behavior may be needed for long-term stability, whereas a fluid-like state is most likely required when shaping. Lastly, surface effects may play a critical role, particularly on the microscale. A physics-based model will greatly aid to understand and eventually predict the observed behavior. With every step towards engineering control over fibrous tissue shape, more can be learned about the mechanics of morphogenesis.

Chapter 3

Robotic Micromanipulation Platform

The work done on the robotic microsurgery platform is going to be submitted as

Erik Mailand^{*}, Matthias Rüegg^{*}, Jon Märki, and Mahmut Selman Sakar. Dexterous robotic micromanipulation of 3D culture models for high-content experimentation (*equally contributed)'.

The universal soft robotic microgripper concept has been published as

Haiyan Jia, **Erik Mailand**, Jiangtao Zhou, Giovanni Dietler, John Kolinski, Xinling Wang, and Mahmut Selman Sakar. Universal soft robotic microgripper. *Small* (2019) [119]

3.1 Introduction

Engineered 3D culture models emerged as an alternative to animal experimentation in order to study the onset of diseases and test novel therapies. Precise and dynamic control over chemical and physical environment of the cells including the composition of the extracellular matrix ensures robust self-assembly of organ-mimicking 3D constructs [36, 37, 120, 121]. Microfabricated platforms significantly increase the throughput and, combined with modern imaging systems, realize automated control over culture conditions and visual inspection [122]. In health sciences, medical robots are revolutionizing minimally invasive diagnosis and surgical treatment of diseases [123]. Combined with artificial intelligence, surgical robots could potentially outperform physicians on certain medical interventions. Inspired by these advancements, we envision that miniaturized versions of these devices that are integrated with motorized microscopes will provide unprecedented opportunities for life sciences. Tasks that are currently being manually performed such as transport of samples could be automated, which would improve speed, precision, and repeatability. More importantly, a whole new set of manipulation tasks could be performed such as (i) spatiotemporally resolved stimulation of tissues for recapitulating embryonic conditions, (ii) real-time interrogation of tissue mechanics, (iii) collection of biopsies from selected parts of the tissues for omics analysis, and (iv) localized delivery of infectious or pathogenic materials to study progression of diseases.

In vitro bioengineered tissues and organoid systems consist of cell clusters in various configurations including suspended in culture medium, embedded in a hydrogel such as Matrigel, and cultured inside high-throughput microfabricated devices. The constructs are small and delicate, thus any mechanical operation must be done with extreme precision and in a minimally invasive manner. Furthermore, every sample is unique in its shape, size, and composition due to heterogeneity in culture conditions and stochasticity in gene expression. The robotic manipulation technology must work within these constraints and uncertainties, which requires exceptionally high dexterity. Notably, for the dissemination of the tools within the community, it is instrumental to provide a modular solution that readily interfaces with conventional motorized microscopes and open-source control software.

In this chapter, we present a multiple degrees of freedom (DOF) robotic manipulation system

that provides the precision and dexterity required to operate on microscale biological samples. The system is designed to be modular to accommodate a variety of end-effectors commonly used in tissue manipulation. We addressed the heterogeneity challenge by implementing a "learn from the expert" paradigm. The system is capable of recording and repeating tasks performed during the teleoperation mode. The control software of the robot is developed within the micro-manager (μ Manager) framework, an open-source software that aims to bundle proprietary drivers of microscopy components using an application programming interface (API) [124]. μ Manager provides a graphical user interface (GUI) with plugins and libraries necessary to perform teleoperation and a scripting environment to program open-loop automated manipulation tasks. The overall framework is extendable to closed-loop control, particularly based on visual feedback thanks to the availability of a rich computer vision library [125].

In the second part of the chapter, a photochemical manipulation method is introduced that allows spatial and temporal control over cell death. Controlled removal of cells without perturbing the ECM reveals important insight on tissue mechanics, as experimentally demonstrated in the following chapters. Control over cell death has been achieved by exposing cells to UV light [126]. More sophisticated methods have been developed based on optogenetics. Light sensitive proteins have been integrated into the cells, which undergo conformational changes inducing an apoptotic pathway upon light exposure [127, 128]. UV exposure is toxic and must be carefully localized while optogenetic techniques are immature and operate with a low signal to noise ratio. The presented protocol is based on a commercially available chemical, blebbistatin. The method does not require genetic manipulation, high optical intensity or UV light, which makes it applicable to a variety of tissue models.

3.2 Robotic Micromanipulation System

3.2.1 Concept

The actuators that are responsible for controlling the position and orientation of the end-effectors are expected to be compact and portable. Otherwise, the system would have compatibility issues with microscope stages and environmental chambers. Inspired by an ophthalmic microsurgery

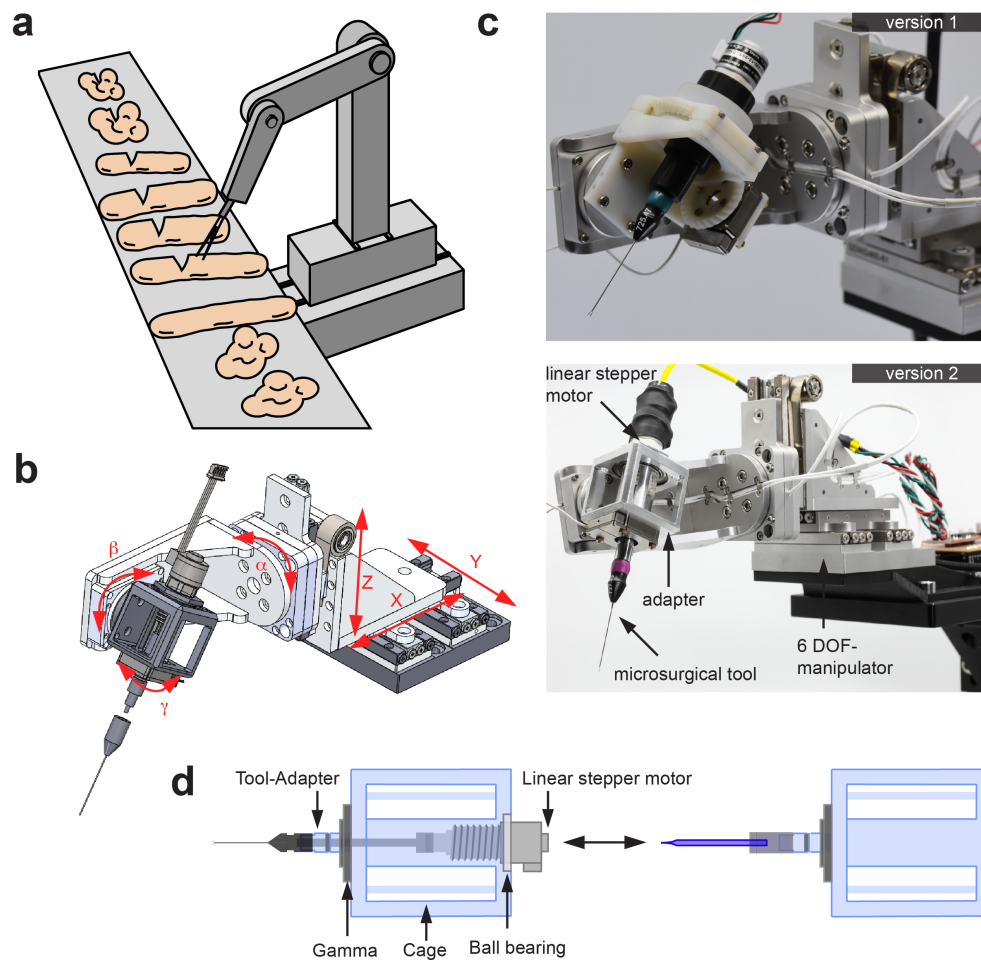


Figure 3.1: 6-DOF robotic micromanipulation system. (a) Schematic illustration showing serial microtissue processing. A compact 6-DOF robot cuts microtissues that vary in size and form. As an example engineered capsule-shaped microtissues (introduced in chapter 5) and organoids are shown. (b) CAD drawing of the robotic system with red arrows indicating the translational axes X, Y, Z and the rotational wrist composed of α , β and γ . (c) Photograph of the 6-DOF system build from piezo-electric stick-slip actuators with adapter for tool actuation. Upper panel: 3D-printed adapter with original design (first version). Lower panel: Machined adapter with new design (second version). (d) Section view of the final adapter along with a disposable surgical instrument actuated by a linear stepper motor (Left), or along with a non-actuated tool (e.g. glass capillary) and without the stepper motor (Right).

platform [129], we designed a 6-DOF robot with nested piezoelectric actuators that occupies a volume of $200 \times 100 \times 70 \text{ mm}^3$. We developed an adapter that allows mounting of actuated tools such as scissors and tweezers along with non-actuated tools such as dissection knives, needles, and glass capillaries (Figure 3.1a).

For serial sample processing, the program has record and replay functions and is integrated into

μ Manager. μ Manager provides a large ecosystem of preexisting device adapters for over 200 hardware drivers. The software platform specifies a device adapter API and unifies the driver interfaces from imaging devices to motorized stages of different vendors. The code is written in C++ programming language and it is amenable to future extensions such as solving the inverse kinematics problem and implementing elaborate referencing schemes. The device adapters are used as building blocks for various experimental units (e.g. microscope stage, syringe pump) on three different levels: (1) Individually compiled device adapters can be linked directly against a C/C++ application, independent from the μ Manager core functionality. (2) The GUI of μ Manager is used to design and script (beanshell) experimental protocols including imaging and automated image processing. (3) Using one of the μ Manager wrappers for MATLAB or Python, the capabilities of specialized software can be tapped on such as machine learning (e.g. Pycro-Manager [125]).

Hardware

The robotic manipulation system is constructed from piezoelectric stick-slip actuators that have sub-micron positioning precision. It has three translation stages (X, Y, Z), two rotary actuators equipped with positional feedback (α (roll), β (pitch)) and a lightweight rotary stage without sensor (γ) in a 'T(X)-T(Y)-T(Z)-R(α)-R(β)-R(γ)'-configuration. To hold and actuate microsurgery tools, a custom designed adapter, mounted on β , incorporates the open-loop γ -stage for infinite axial rotation of the end-effector (Figure 3.1b).

End-effectors The mechanism of actuating microsurgery tools such as microscissors and microtweezers is based on the movement of a plunger against a passive spring-loaded mechanism. The movement of the plunger is coupled to the translation of a metal tube over the blades, controlling the opening and closing of the tool. The original design was optimized for accommodating hand-held surgical tools and quick tool exchange (Figure 3.1c, Top). We altered the original design and added a transmission to improve the accuracy and reduce play, a crucial upgrade for high-throughput automation (Figure 3.1c, Bottom). The adapter with the new design was micro-machined from aluminium. An external cage houses a pivot-mounted tubular motor support that is rotated by the γ -stage. It contains a small lead screw stepper motor that acts as a piston to

push the plunger into the mounted tool. Compared to the original design, overall complexity is reduced by stacking the end-effector directly to the γ -stage. Also it allows the use of a standard ball bearing with small diameter. The original design required a specialized ball bearing with large diameter and thin cross-section, which is significantly more expensive. The operation of the motor is controlled by a programmable single-board Arduino microcontroller. The motor can be quickly removed for the installation of non-actuated tools. We developed a specific tool adapter for glass capillaries connected to a microinjection system (PV830, World Precision Instruments). The adapter design allows the use of different capillary sizes with tubing connection (Figure 3.1d).

Precision and accuracy The translation stages are linear stages with a parallel-rail structure. One rail is the stick-slip actuator and the other a passive guide. Z has in addition a constant-force spring to compensate for the weight of the spherical wrist. α and β are closed-loop rotary stages and γ is an open-loop rotary stage. The linear stages have a range of 40 mm and closed-loop resolution of 4 nm. They can be backdriven by applying a force of 5 N and apply maximum forces of around 4 N during motion. The rotary stages α and β have a resolution of $25 \mu^\circ$ (microdegree), can be backdriven by applying torques of, respectively, 15 N-cm and 6 N-cm and apply maximum torque of, respectively, 6 N-cm and 3 N-cm. γ has a resolution of $3 m^\circ$ (millidegree). The maximum stage speed is around 20 mm/s for the translational stages, 15 degree/s for α and β and around 45 degree/s for γ . The stepper motor has a per step increment of 0.02 mm delivering up to 35 N of force.

Referencing The zero positions of the translation stages are set by their mechanical end stop. The α and β stages are equipped with a nano-sensor and a reference mark. While α has mechanical stops to prevent full revolution, β required a specific software implementation. To ensure collision free referencing, the range is restricted to $\beta = [0^\circ, 90^\circ]$ with a defined shutdown position at 0° . The open-loop rotary actuator γ does not have a mechanical end stop for operational reasons and is currently excluded from the referencing operation.

Software

The Smaract MCS controller unit handles the host communication and controls all stages. A μ Manager hub object is used as a single communication port to the controller to implement

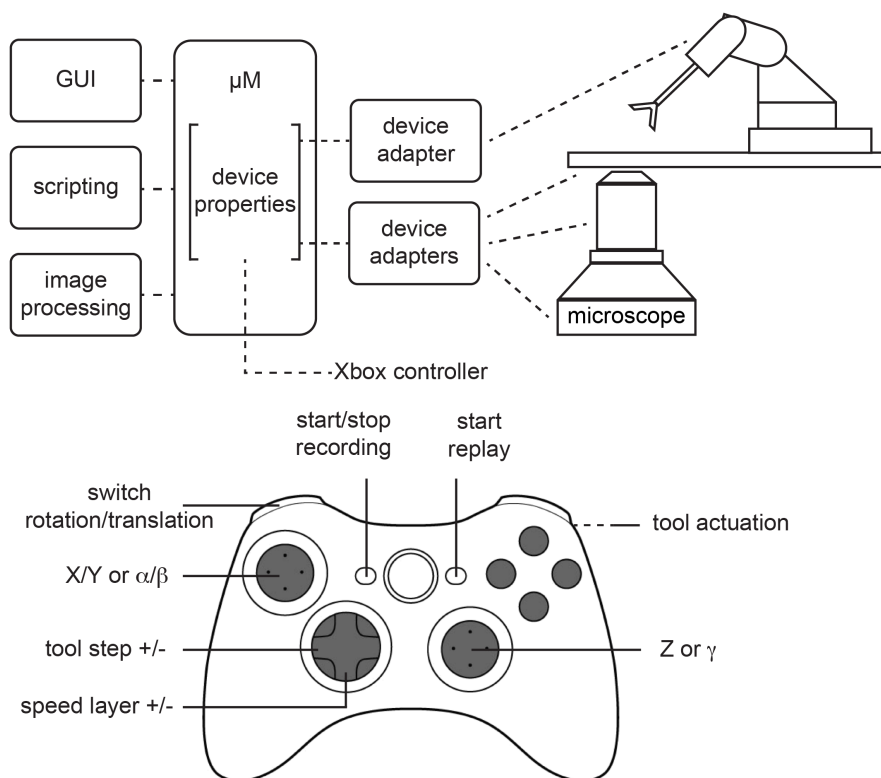


Figure 3.2: Schematic illustration of the software architecture and controller. The robot as well as other microscopy instruments communicate with the Core API from $\mu\text{Manager}$ via device adapters. Device adapters translate specific device driver API to common $\mu\text{Manager}$ plug-in interface. Each loaded device exposes a number of properties which can be read and changed via $\mu\text{Manager}$. Teleoperation is performed using an ASI Xbox controller connected to the $\mu\text{Manager}$ via a built-in plugin. $\mu\text{Manager}$ provides the graphical interface as well as scripting environment for control and real-time image processing.

all cross-channel logic. The linear stage class of $\mu\text{Manager}$ is used for all six stages due to the lack of a rotary stage class. Although the Arduino microcontroller has a simple serial connection protocol that is used by a generic device adapter class, it is accessed by the hub object to retrieve stepper motor positions. Device adapters communicate with $\mu\text{Manager}$ by exposing a number of properties which $\mu\text{Manager}$ can, respectively, read or write and potentially trigger an action of the connected device. A property is a field consisting of a name and a value. Properties can be accessed within the built-in GUI, via the beanshell scripting environment, or implemented plugins. We developed a user-friendly $\mu\text{Manager}$ -based GUI Plugin for manual command entry and retrieval of recorded data.

Motion and control Teleoperation is performed using an ASI Xbox controller that is connected to the program via a built-in plugin. Xbox controllers are optimised for multiple DOF motion control. Button assignment is customizable, depending on the specifics of the manipulation task. There are two joysticks and we assigned them to control either the translational stages or the spherical wrists. Upon displacement of the joystick, a discrete property value between -1 (left or down) and 1 (right or up) is sent to the corresponding stage. With increasing joystick displacement, the corresponding stage moves at around 25% of the maximum speed and linearly increases to 100%. To eliminate the errors accidentally caused by hand shaking, a displacement threshold is set. This way, parasitic movements occurring with less than a given relative movement amplitude are filtered out. For tool actuation, the stepper motor is controlled using either a dynamic or a discrete mode. Dynamic control follows the same principle as stage movement, whereas an intensity vector that linearly goes from the zero to the maximum position is assigned to a trigger on the Xbox controller. Upon trigger release the stepper motor goes back to the zero position. The discrete method divides the range into steps and a trigger of a button changes a property value that indicates the discrete position of the stepper motor. The zero position, step range, and maximum position of the stepper motor are set and can be changed within the software.

Speed layer Depending on the type of experiment and location of the manipulator, a variety of velocities or sensitivities are required, respectively. Speed layer functionality was implemented as a property value (1, 10, 100, or 1000), which acts as a simple multiplication factor of the speed variable that is computed on each movement based on the joystick displacement.

Motion recording and replay The manipulator is equipped with a teach-in and replay functionality. Recording mode is activated by changing a Boolean property value. On activation, each change of position triggers the printing of all seven positions into a text file. The replay function runs the motion pattern from a selected text file. The motion pattern can be replayed from 0.1 up to 10 times of the original speed and offsets can be added to the translation stages.

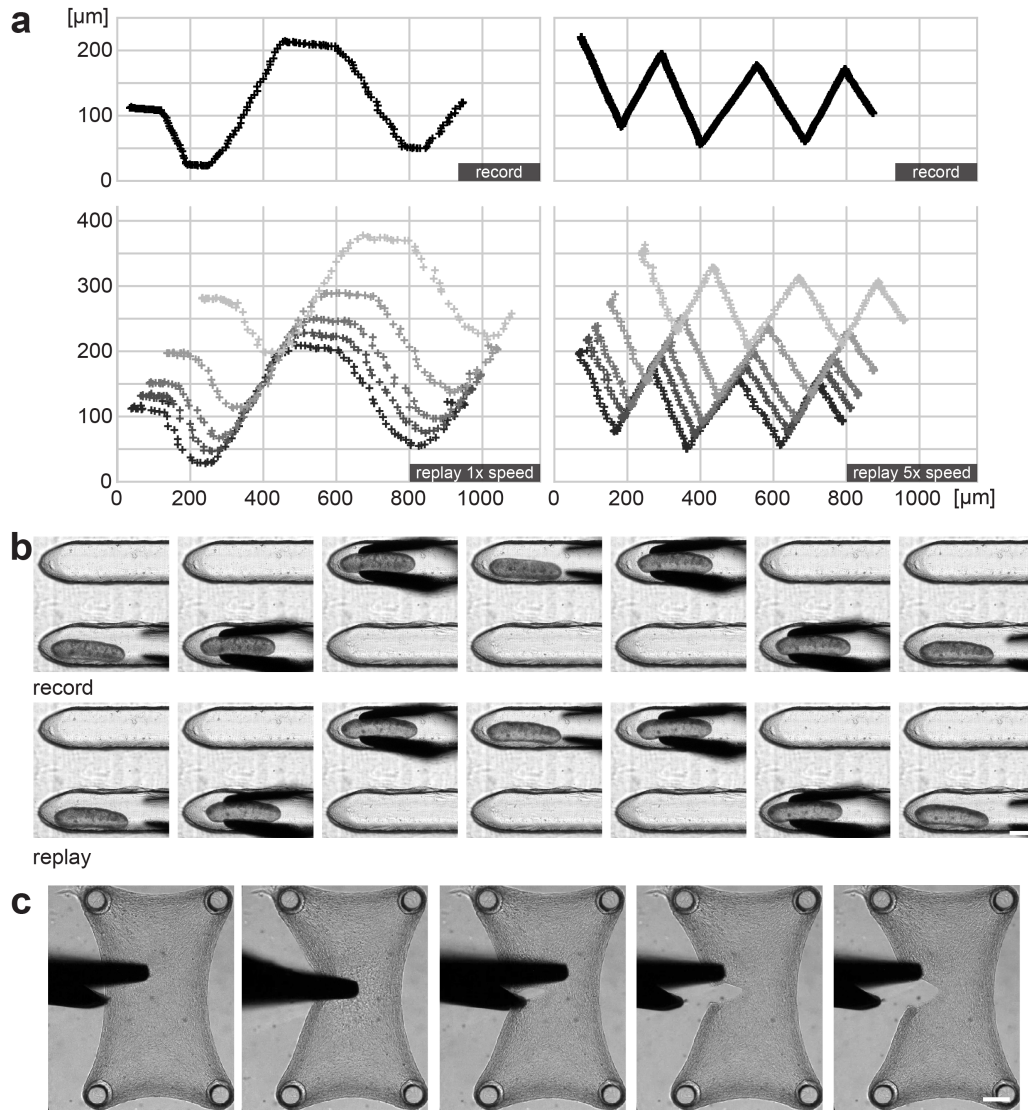


Figure 3.3: Teleoperated manipulation and automated repetition of motion. (a) Recorded motion along X and Y with a capillary end-effector (Upper panel) is replayed by the robotic system (Lower panel). The robot replays the recorded motion at real-time speed (Left) and at five times higher speed (Right). The motion is repeated in total five times with an X and Y offset increment of 20, 40, 80, and 160 μm . (b) Engineered microtissues are picked up with actuated microtweezers from one microwell and placed into another one. The manipulation task was accurately repeated. (c) Actuated microscissors are used to cut engineered microtissues under tension. Scale bars, 200 μm

3.2.2 System Validation

The robot was mounted on an inverted microscope to validate implemented features. Using a glass capillary as an end-effector, we recorded teleoperated motion on a plane. The robot re-

peated the recorded motion sequence five times with an X and Y offset increment of 20, 40, 80, and 160 μm . The robot successfully repeated curved and zig-zag motions with the programmed deviation from the original trajectory at both real-time and five times higher speed (Figure 3.3a). As a second test, using microtweezers, we successfully performed pick-and-place tasks by transferring engineered biological tissues (introduced in chapter 5) from one microwell into another, and back. The robot accurately repeated the recorded manipulation task (Figure 3.3b). Finally, using microscissors, we performed surgical cuts on tethered three-dimensional fibrous microtissues (Figure 3.3c). The engineering and morphological evolution of the microtissues will be presented in chapter 4. Using the same microtissues, we performed surgical flaps and collagen-based grafts in the pursuit of repairing the damage and reconstructing the original tissue shape (Figure 3.4).

3.3 Optochemical Control over Cell Viability

Previous work has shown that exposing blebbistatin-treated cells to blue light causes a strong phototoxic effect that leads to a dose-dependent cell death because blebbistatin undergoes a conformational change [130, 131]. To spatially pattern blue light on defined regions, we used a programmable Digital Micromirror Device (DMD) connected to a fully motorized inverted microscope. DMD is a projector constructed from individually addressable microscopic mirrors arranged in an array that corresponds the pixels of the displayed image. Compared to solutions based on galvano mirrors or spatial light modulators, this projection method provides rapid exposure of large areas at full sample depth and simultaneously on many samples.

The culture medium was exchanged with a medium containing 20 μM blebbistatin 30 minutes prior to light exposure. Light exposure was pulsed 5 times for 3 seconds with 30 second periods. Light intensity was adjusted between 1 and 100 $\mu\text{W cm}^{-2}$ depending on the size of selected region (0.06 to 0.9 mm^2). After light exposure, the medium containing the inhibitor was exchanged with fresh culture medium. The duration and power of blue light exposure was optimised to deliver 100% cell death within the treated area while preserving viability throughout the rest of the microtissue (Figure 3.5b). Brightfield illumination or exposure to green light (525 nm) had no effect on blebbistatin-treated cells, which confirmed that the response was generated by a wavelength-specific optochemical conversion (Figure 3.5c).

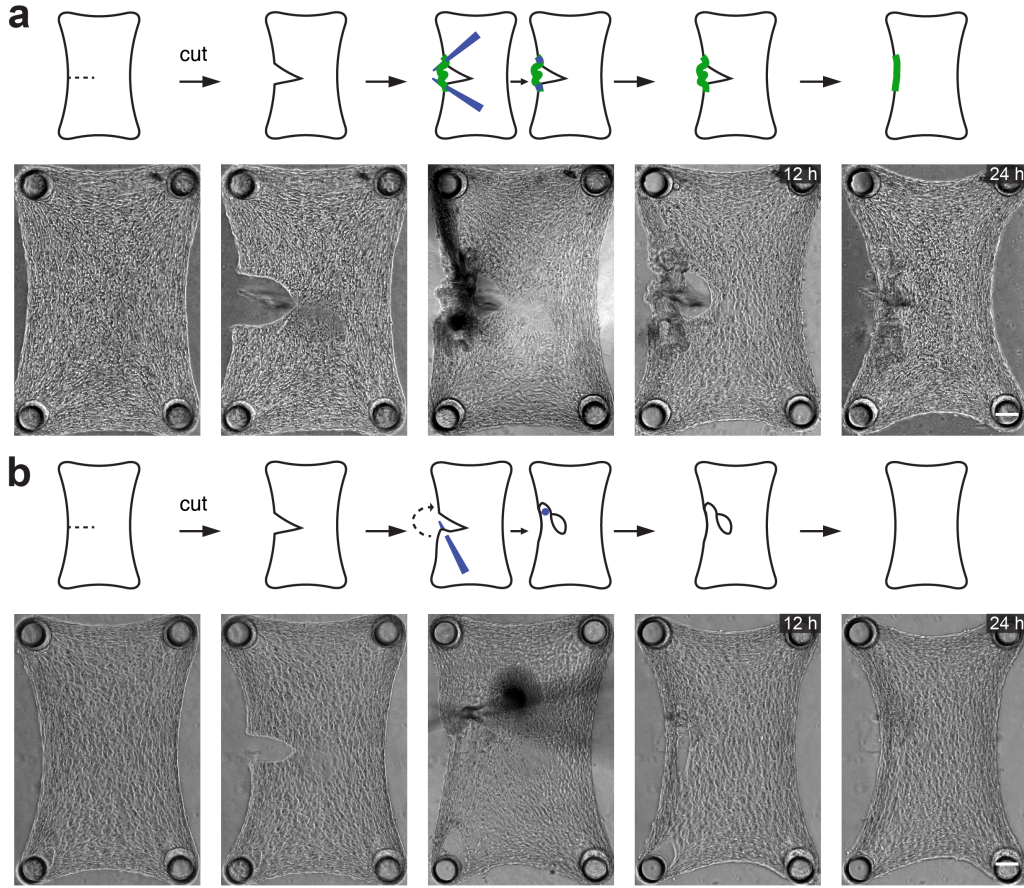


Figure 3.4: Plastic surgery to repair a sidecut in tethered collagenous microtissues. (a) Surgical flap. Unidirectional tissue advancement into the defect area by stretching the tissue and subsequent fixation with a microneedle. (b) Grafting. Decellularized collagen structures from microtissues are used as cell-free scaffold to guide repair. Collagen piece was fixed with two microneedles. Scale bars, 100 μm

3.4 3D Live Imaging during Robotic Manipulation

Fully automated 3D micromanipulation requires real-time visual feedback. Bright-field microscopy cannot capture 3D morphology and confocal systems suffer from low speed, relatively fast photobleaching, as well as phototoxicity. Light-sheet microscopes emerged as an alternative for 3D live imaging, delivering low phototoxicity at high scanning rates. Extensive ground work has been done on selective plane illumination microscopes (SPIM) [132]. We have a dual plane SPIM (diSPIM) system assembled by 3i. The system consists of two orthogonal objectives positioned at 45° above the specimen. This configuration is unique because it works with conventional sample holders such as coverslips and petri dishes (Figure 3.6a). 3D images are captured by using each

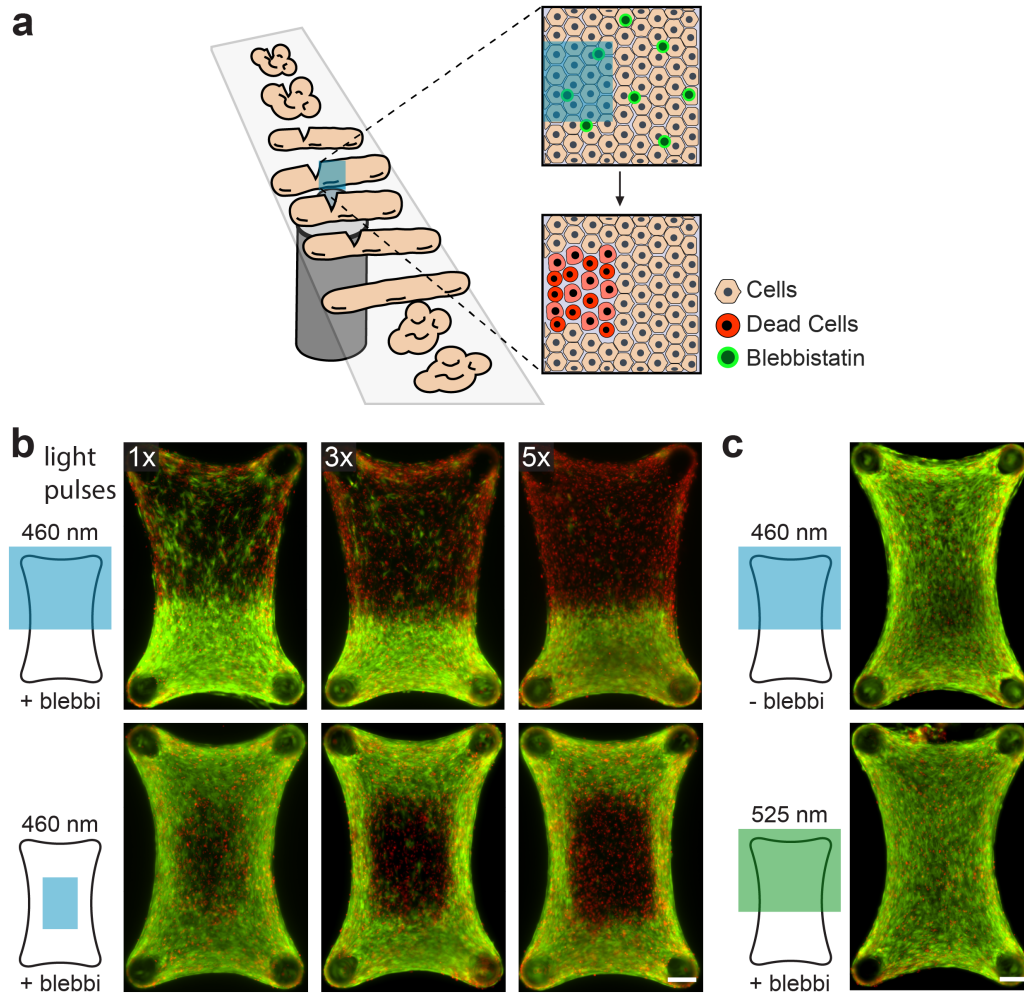


Figure 3.5: Spatiotemporally controlled photoconversion of blebbistatin and cell death in microtissues. (a) Schematic of local cell death induction with light. As an example engineered capsule-shaped microtissues (introduced in chapter 5) and organoids are shown. The efficacy of treatment is assessed in tethered three-dimensional fibrous microtissues (introduced in chapter 4) with live/dead staining (live, Calcein AM (green) and dead, Ethidium homodimer III (red)). (b) Optimization of the exposure protocol. Pulses of blue light (460 nm) exposure is generated for 3 seconds. A 30 second break is given in between consecutive pulses. Five pulses are enough to ensure complete killing within the targeted area. Half of the tissue (upper panel) or the center of the tissue (lower panel) is targeted to show that the treatment does not depend on the location. (c) Blue light exposure in the absence of blebbistatin or green light (525 nm) exposure of blebbistatin show no phototoxic effect on the exposed area. The treatment requires the presence of the chemical and is wavelength specific. Scale bars, 150 μm

objective for imaging and illumination in turns. We assembled this system on another motorized inverted microscope to be able to combine photoexcitation with 3D imaging. The control software is compatible with $\mu\text{Manager}$. Figure 3.6b (Left) shows a representative image captured

by this system. We further assessed cell viability in 3D after phototoxic treatment (Figure 3.6b, Right). The robotic micromanipulation system is mounted on the light-sheet system for real-time 3D operations (Figure 3.6c).

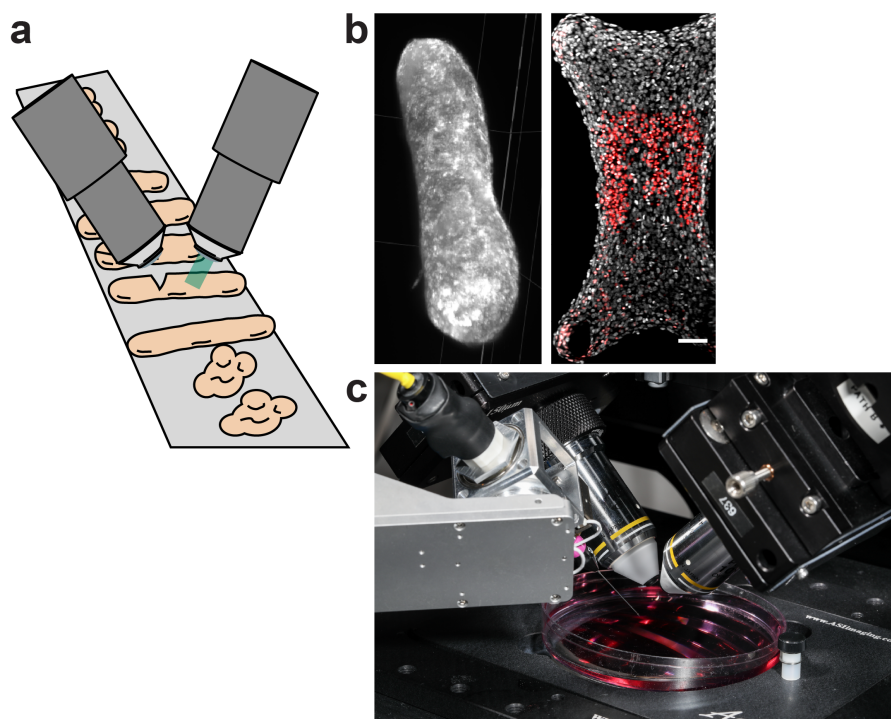


Figure 3.6: Light sheet microscopy for 3D live imaging. (a) Schematic illustration of the light-sheet imaging platform. Two orthogonal objectives are positioned at 45° above the specimen and scan multiple samples by using each objective for imaging and illumination in turns. As an example engineered capsule-shaped microtissues (introduced in chapter 5) and organoids are shown. (b) Left: 3D view of a diSPIM scan showing fluorescently labelled collagen (Collagen-647) of unconstrained microtissue. Right: 3D view of a diSPIM scan showing cell nuclei (Hoechst, grey) of tethered microtissue after light induced cell death. Dead cells are labelled with Ethidium homodimer III (red). (c) Photograph of the robotic manipulation system mounted on the diSPIM for live imaging during manipulation (Image: ©Alain Herzog 2020 EPFL). The upright light-sheet system sits on a fully automated inverted microscope for optical manipulation. Scale bar, 200 μm

3.5 Discussion

A dexterous robotic micromanipulation system is introduced for life science research. The commercially available end-effectors are relatively large for microengineered biological samples. Further research is required for the development of more proper tools. There are two interesting routes in this endeavour; (i) microfabrication using polymers and metals, particularly using laser

micromachining, electrodeposition, and two-photon polymerization and (ii) processing glass through pulling, forging, and printing techniques. Living matter changes shape and mechanical properties over time, which makes rigid grippers unfavorable. We developed a soft robotic universal microgripper that was made of a shape-memory hydrogel [119]. The gel adapts to the shape of engineered cell clusters upon physical contact (Figure 3.7). The tool can be readily integrated as an end-effector to the robotic micromanipulation system. Further work has been done to stretch, compress, and indent engineered tissues, but has not been further pursued in the scope of this thesis.

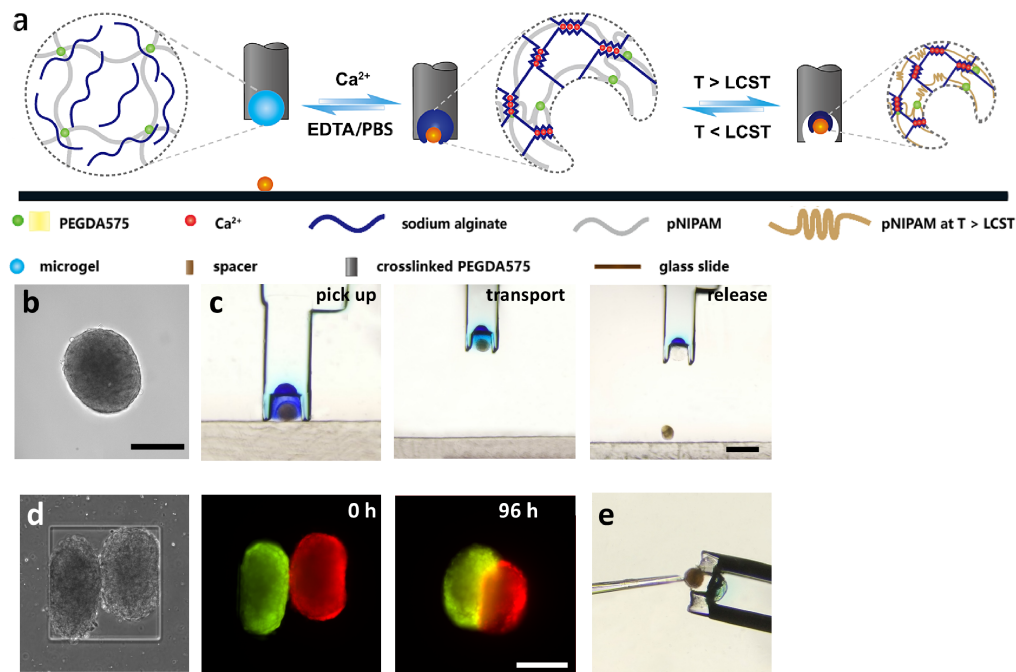


Figure 3.7: Smart actuated hydrogel allows gripping and placing of microtissues. (a) Schematic of the gripping mechanism, based on the reversible shape memory and thermoresponsive swelling properties of the hydrogel. (b) Micrograph of an engineered cell cluster composed of fibroblasts and collagen. (c) Images from a representative microtissue transport. Scale bar, 500 μm . (d) Two microtissues are placed into the same well. Staining of the cytoplasm with different colors shows the merge of the tissues in time. Scale bar, 200 μm . (e) Microtissue held by the soft microgripper can be accessed for dexterous surgical manipulation.

Several steps have to be taken into account to go towards high throughput automation of engineered microtissue manipulation. The γ -stage provides open-loop rotation without mechanical stop. A reference mark has to be integrated to enable automated axial rotation of the end-effector. More sophisticated software implementations are required, to read and process recorded motion,

which will enable more accurate offset control and relative speed adaption for jerk reduction and sample approach. Moreover, the implementation of inverse kinematics into the control software would enable more complex operations. To manipulate a large number of 3D samples in centimetre scale culture dishes, the robotic system must communicate with the microscope stage. Together with the motorized focusing of the microscope, the robot will receive 3D coordinates. The combination of real-time feedback and motion planning would pave the way towards highly complex tasks such as flexible microneedle steering in hydrogels.

For manipulations over a long duration, the robot must be positioned inside an incubation system. This can be achieved by modifying the environmental chamber with access points for cables. Preliminary trials demonstrated the feasibility. A spheroid residing inside an incubation chamber has been stretched with two microneedles using two manipulators mounted on a microscope (Figure 3.8).

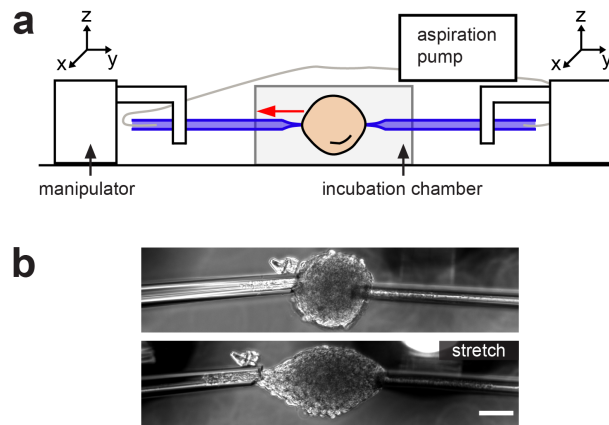


Figure 3.8: Microtissue manipulation over a long duration of time. (a) Schematic illustration of setup. Custom-made incubation chamber allows access for capillaries. Both capillaries are connected to an aspiration device and held by manipulators. (b) A cluster of fibroblasts is stretched over hours using the setup. Scale bar, 100 μm .

Optical manipulation methods are ideal for high-resolution perturbation of tissue mechanics. With the amazing molecular manipulation capabilities optogenetics offers, complex intracellular pathways that affect tissue mechanics can be manipulated using light [133, 134]. Substantial amount of time was dedicated to test several optogenetic constructs that are reported to enhance or inhibit contractility. Light-mediated control over contractility was tested by regulating gene expression [135], inhibiting RhoA by sequestration [136], or recruiting RhoA activator to the cell

membrane [133]. More details can be found in section 3.6. Recruitment of the light sensitive proteins upon illumination was achieved in single adherent cells (Figure 3.9). However, on deformable silicon substrates, no considerable increase in traction forces could be detected. The optogenetic system could not be replicated in microtissues, which may be due to the sensible nature of the genetic system, cell-to-cell DNA uptake variation, and challenges with light exposure in 3D. Moreover, substantial increase or decrease in contractility of several cells is required for initiating bulk changes in tissues, which seems to be quite challenging considering the high background activity of the constructs [133]. Significant work is required to make light-induced contractility to work at the tissue scale. The selective induction of cell death has a direct effect on tissue mechanics and blebbistatin is already optimized for biological systems. Moreover, this chemical shows very high stability, requires no special optical setup, works at low light intensities, and its sensitivity to background illumination is negligible. Taken together, the method that we introduced may become instrumental in mechanobiology research.

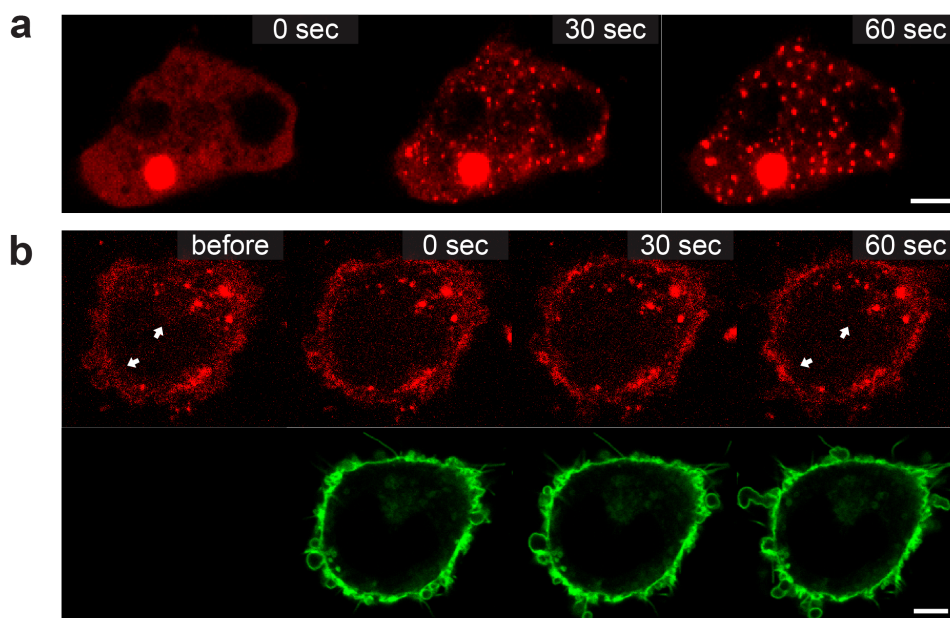


Figure 3.9: Spatiotemporal controlled protein localization in single cells. (a) CIBN functionalized multimeric proteins (red) sequester Cry2 proteins upon blue (488 nm) light illumination. The appearance of many bright red spots within the two HEK cells indicates the clustering of proteins. (LARIAT [136]). (b) Localization of the RhoA activator ARHGEF11 (red) to the membrane (green) upon blue (460 nm) light exposure in a single 3T3 fibroblast cell. Arrows indicate loss of dispersed signal in the cytoplasm due to recruitment of the light-sensitive proteins to the cellular membrane (optoGEF-RhoA [133]). Scale bars, 5 μm

3.6 Technical Details

Robotic manipulation

The piezo-electric stages were assembled from SmarAct GmbH according to our specifications. X (SmarAct SLC-2460-D-L-E), Y (SmarAct SLC-2460-O-W-D-L-E), Z (SmarAct SLC-2460-D-L-E), α (SmarAct SR-4513-D-S), β (SmarAct SR-2812-S), and γ (SmarAct SR-1908). Actuation of the tools was driven by a stepper motor (Can-Stack 15000 series LC1574W-12-999, Haydon Kerk Pittman¹) controlled by an Arduino microprocessor. Actuated tools are purchased from Alcon². Advanced DSP Tip 27+ Straight Scissors (727.53) and Advanced DSP Tip MAXGRIP Forceps 25+ (725.13P). The shaft of the microscissors is 27 Gauge and has a length of 27 mm.

¹www.haydonkerkpittman.com/products/linear-actuators/can-stack-stepper/15mm-15000

²www.alcon.widen.net/s/zrlg779yio

The shaft of the microtweezers is 25 Gauges also with a length of 27 mm. Glass capillaries were purchased from Science Products. Other manipulation instruments were purchased from Fine Science Tools. Robotic manipulation was performed with a Nikon Ts2r or a fully motorized Nikon Ti Eclipse (Nikon Instruments, Inc) microscope, and operation was visualized with either a 4x or 10x objective. μ Manager version 1.4.23 was used and the device adapter code is hosted on c4science-git. Preexisting device adapters can be found on the repository of μ Manager³.

Optochemical manipulation and Imaging

For method development, constrained fibrous microtissues (introduced in chapter 4) were used. Blebbistatin (in DMSO, Sigma-Aldrich) was added to the culture medium. Pre-defined regions of the tissues were exposed to blue light (460 nm, coolLED pE-4000) using a programmable DMD (Digital Micromirror Device, Andor) device through a Plan Apo Lambda 10x objective mounted on a fully motorized Nikon Ti Eclipse (Nikon Instruments, Inc) microscope. For light-sheet imaging a Marianas LightSheet (3i, Intelligent Imaging Innovations⁴) was used equipped with two 10x objectives.

Optogenetics

The possibility to spatiotemporally control gene expression was investigated using a modified Cas9 system to then, amongst others, regulate the expression of constitutive active or deactive RhoA proteins, respectively [135]. For pulsed illumination over long duration of time an Arduino controlled LED system was developed and placed under the culture dish in the incubator. In another experiment, proteins of interest were inactivated, using CRY2-labelling and sequestering with multimeric proteins fused to CIBN upon optical stimulation[136] (Figure 3.9a). In later attempts, RhoA recruitment specific optogenetic systems were tested, such as the TULIPs-mediated activation of RhoA [137], as well as the constructs CIBN-CAAX-GFP (CIBN-GFP – CAAX) and optoGEF-RhoA (ARHGEF11 - Cry2-mCherry) kindly provided by Mathieu Coppey [133] (Figure 3.9b).

³www.micro-manager.org/wiki/Device%20Support

⁴www.intelligent-imaging.com/marianas-lightsheet

Chapter 4

Surface and Bulk Stresses Drive Morphological Changes in Fibrous Microtissues

The work presented in this chapter has been published as

Mailand, E., Li, B., Eyckmans, J., Bouklas, N. & Sakar, M. S. Surface and bulk stresses drive morphological changes in fibrous microtissues. *Biophys. J.* (2019) [138]

Kim, J., **Mailand, E.**, Ang, I., Sakar, M. S., & Bouklas, N. A model for 3D deformation and reconstruction of contractile microtissues. *Soft Matter* (2020) [139]

4.1 Introduction

Tissue morphogenesis, the shaping of tissues, is a critical process during development and repair. During development, coordinated cell movement and rearrangement, deposition and assembly of extracellular matrix (ECM), and asymmetric cellular contractility morphs the embryo into a coherent body that consists of compartmentalized organs and tissues with characteristic shapes and well-defined boundaries [1]. When tissues are injured, these embryonic processes are partially recapitulated, which leads to a reconstruction process [140]. Whereas much research has focused on understanding the signaling pathways involved in wound closure [29, 141, 142], little is known about the mesoscale physical principles of multicellular organization required to restore the architecture of three-dimensional (3D) tissues during repair.

In fibrous tissues, fibroblasts physically interact with the surrounding nonlinear elastic and viscoelastic ECM [97, 143, 144]. These interactions are studied *in vitro* by encapsulating cells within 3D biopolymer hydrogels, such as collagen and fibrin [45–48]. Once the scaffold is polymerized, cells adhere to and pull on the fibers, resulting in the contraction of the hydrogel [49–51, 56]. Pioneering research suggested a central role for traction forces in closing skin wounds [26, 27, 39]. With the invention of microengineered wound healing models, it has been experimentally confirmed that epidermal tissue repair is regulated by cellular forces [19, 145].

Construction of 3D tissue architecture, however, is not solely driven by bulk tissue contraction. Wound-activated closure of topological defects resembles morphogenetic events associated with embryogenesis [140, 146, 147]. Embryonic tissues are best modeled as viscous liquid drops whose shape is governed by the minimization of free surface energy [74, 104, 148, 149]. Similarly, 3D cell aggregates show fluid behavior at longer time scales [8, 101, 150, 151]. Surface stresses of even synthetic soft materials that are in thermodynamic equilibrium are strong enough to deform solid bodies in their bulk [152, 153]. Surface stress of solids becomes equivalent to surface tension of liquids when stress is constant and the surface behavior is isotropic. While surface stresses are important drivers for shaping living and synthetic materials, theoretical and computational studies of fibrous tissues have so far been focused on mechanical anisotropy and nonlinear elasticity, and neglected the surface effects [154–158].

Given its role in shaping embryonic tissues, we hypothesize that, in addition to bulk contraction, cell-derived surface stresses also play a crucial role in the formation and restoration of shape in fibrous tissues, specifically at small length scales. Recent work has shown that fibroblasts accumulate at the periphery of reconstituted collagenous microtissues, which leads to formation of a heterogenous architecture containing a collagen-rich core that is sparsely populated by cells and a fibronectin-rich shell with high fibroblast density [159, 160]. We postulate that the spatially heterogenous force generation and matrix remodeling within fibrous tissues can be represented in the continuum scale through the introduction of surface stresses. We employed microfabricated tissue gauge technology with robot-assisted surgical and optochemical manipulation to test this hypothesis and investigate how tissue shape evolves during self-healing of wounded fibrous microtissues. Building on an energetically motivated equilibrium theory, we developed a computational framework that consists of a novel constitutive model coupling active and passive elasticity with bulk and surface energy components. Finite element simulations of the model recapitulated the shape response of microtissues to various surgical interventions, therefore confirming that cell-derived surface stresses play a major role in the closure of wounds and restoration of shape in fibrous microtissues. Our results also indicate that surface contractile stresses may act together with bulk contraction in sculpturing the form or they may drive tissue morphogenesis in opposing directions depending on the boundary conditions.

4.2 A New Equilibrium Theory for Contractile Microtissues

The main constituents of the experimental model are collagen fibers, fibroblasts and culture medium. The solid collagen network was modeled as a 2D foam-like material with high compressibility while the fluid component was not explicitly modeled. Contraction of the tissue on its surface and in the bulk were driven by isotropic packing of the constituent collagen fibers. We refer the reader to [161] for the general theory on the curvilinear kinematics of the surface and the volume of a 2D soft body and [162] for the specific considerations implemented in this work. We adopted the same notation in the following formulation.

We consider a continuum body that takes the material (or reference) configuration \mathcal{B}_o in the fully relaxed state and spatial (or current) configuration \mathcal{B}_t at time $t > 0$ under loading. The spatial and material coordinates \mathbf{x} and \mathbf{X} are connected through an invertible deformation map $\mathbf{x} = \phi(\mathbf{X})$. We can define the deformation gradient as $\mathbf{F} = \text{Grad } \phi(\mathbf{X})$ through this map. The Jacobian determinant $J = \det(\mathbf{F})$ defines the volumetric change of a material volume element dV to a spatial volume element dv . The boundary of the body is defined by a network of smooth curves $\mathcal{C}_o^\kappa(\mathbf{X})$ in the material configuration, with $\kappa = 1, n_{\text{curv}}$, where $\mathcal{C}_o = \cup \mathcal{C}_o^\kappa(\mathbf{X}) = \partial\mathcal{B}_o$. The intersections of n_{curv} curves define n_{point} points \mathcal{P}_o^π with $\pi = 1, n_{\text{point}}$. The curve deformation gradient is defined as $\tilde{\mathbf{F}} = \widetilde{\text{Grad } \phi(\mathbf{X})} = \lambda \mathbf{t} \otimes \mathbf{T}$, where $\lambda = dl/dL$ denotes curve stretch, and tangents \mathbf{T} to boundary $\partial\mathcal{B}_o$ are convected by the deformation to $\mathbf{t} = (\tilde{\mathbf{F}} \cdot \mathbf{T})/\tilde{\mathbf{F}} \cdot \mathbf{T}$. Boundary line elements dL of $\mathcal{C}_o = \partial\mathcal{B}_o$ are mapped to elements dl of $\mathcal{C}_t = \partial\mathcal{B}_t$ through the curve Jacobian $\tilde{J} = \det \tilde{\mathbf{F}} = |\tilde{\mathbf{F}} \cdot \mathbf{T}|/|\mathbf{T}|$. In the 2D setting, the curve Jacobian equals the curve stretch $\lambda = \tilde{J}$.

After the definition of the bulk and surface kinematics of the system, we move to the energetic considerations. We made the assumption that there were no internal dissipation mechanisms such as diffusion, viscoelasticity or any dissipation that may stem from the chemical cycle associated with the contraction of fibroblasts. As a result, all deformations are fully recoverable. We postulate that the system can be described through a bulk potential energy $U_o = W_o + V_o$ per material unit volume in \mathcal{B}_o and a surface potential energy $u_o = w_o + v_o$ per material surface length in $\partial\mathcal{B}_o$. The internal contributions can be defined as $W_o(\mathbf{F}; \mathbf{X})$ and $w_o(\tilde{\mathbf{F}}; \mathbf{X})$ while the external contributions can be defined as $V_o(\phi; \mathbf{X})$ and $v_o(\phi; \mathbf{X})$. Note that $W_o(\mathbf{F}; \mathbf{X})$ and $w_o(\tilde{\mathbf{F}}; \mathbf{X})$ are equivalent to the bulk and surface components of the Helmholtz free energy as our material is non-dissipative and perfectly elastic. We restricted the surface potential energy to be isotropic and, thus, w_o is independent of \mathbf{T} . The passive elasticity of the collagen network along with the active contraction of encapsulated fibroblasts provides the bulk potential energy while the surface potential energy stems from the active contraction of fibroblasts residing on the surface of the tissue at equilibrium. The formation of surface stresses is a manifestation of underlying biological processes including the migration of cells towards the surface and the local rearrangement of the fibronectin matrix through cell-induced forces.

The total potential energy functional $I(\phi)$ is defined as:

$$I(\phi) = \int_{\mathcal{B}_o} \mathcal{U}_o(\mathbf{F}, \phi; \mathbf{X}) dA + \int_{\mathcal{C}_o} \mathcal{u}_o(\tilde{\mathbf{F}}, \phi; \mathbf{X}) dL. \quad (4.1)$$

An equilibrated configuration is obtained by minimizing this functional considering all admissible deformations $\delta\phi$. By adding the constraint that the first variation must be equal to zero $\delta I(\phi) = 0$, we obtain a weak form statement as

$$\int_{\mathcal{B}_o} \mathbf{P} : \text{Grad} \delta\phi dA + \int_{\mathcal{C}_o} \tilde{\mathbf{P}} : \widetilde{\text{Grad}} \delta\phi dL = \int_{\mathcal{B}_o} \mathbf{b}_o \cdot \delta\phi dA + \int_{\mathcal{C}_o} \tilde{\mathbf{b}}_o \cdot \delta\phi dL. \quad (4.2)$$

The two point bulk and surface Piola stress tensors are given by

$$\mathbf{P} = \partial_{\mathbf{F}} \mathcal{U}_o \text{ and } \tilde{\mathbf{P}} = \partial_{\tilde{\mathbf{F}}} \mathcal{u}_o, \quad (4.3)$$

where we define the operator $\partial_{(\cdot)}(\cdot) = \frac{\partial(\cdot)}{\partial(\cdot)}$. The partial derivative of the bulk potential energy is taken with respect to the deformation gradient while the partial derivative of the surface potential energy is taken with respect to the surface deformation gradient. The body forces and tractions are given by

$$\mathbf{b}_o = -\partial_{\phi} \mathcal{U}_o \text{ and } \tilde{\mathbf{b}}_o = -\partial_{\phi} \mathcal{u}_o. \quad (4.4)$$

Following the derivation presented in [162], we can finally arrive at a set of localized force balance equations.

To relate the stress at any material point to deformation, we have to consider constitutive laws for the mechanical components. We consider an internal surface energy $w_o(\tilde{J})$ that captures the contribution of cellular contractility at the tissue surface and a bulk internal energy given by $W_o(I, J) = W_o^p(I, J) + W_o^a(J)$. The bulk internal energy consists of a passive term that captures the permanent elasticity of the collagen network including compressibility effects and an active term that represents the bulk contractility of fibroblasts. The internal surface energy component must recapitulate the empirical results including the minimization of surface area and associated reduction of boundary curvature that resembles fluids retaining constant surface tension. On the other hand, the deformations are restricted by the solid nature of the bulk material and the given boundary conditions. This leads to the choice of a specific internal surface energy

that is constant per unit deformed surface length, described as

$$w_o(\mathbf{F}) = \gamma \tilde{J}, \quad (4.5)$$

where γ is an equilibrium value that corresponds to the energy per unit area for the equilibrated tissue. We will refer to γ as the contractile surface modulus, because it represents the level of cellular contractility on the surface at the equilibrium state. The Piola surface stress tensor from (4.3) is obtained as

$$\tilde{\mathbf{P}} = \gamma \tilde{\mathbf{F}} / \tilde{J}, \quad (4.6)$$

and the Cauchy surface stress tensor

$$\tilde{\boldsymbol{\sigma}} = \tilde{\mathbf{P}} \tilde{\mathbf{F}}^T / \tilde{J} = \gamma \tilde{\mathbf{I}}, \quad (4.7)$$

where $\tilde{\mathbf{I}}$ is the surface unit tensor. The implication of (4.7) is that the surface Cauchy stress is constant and isotropic, thus resembling surface tension of liquids. The active part of the bulk energy is chosen to be

$$W_o^a(J) = \eta J. \quad (4.8)$$

Active bulk energy is a function of the volume change of the bulk J based on the assumption that the contractile action of the cells is locally relative to the volumetric deformation. The bulk contractile modulus, η , represents the equilibrium value of cellular contractility in the bulk of the tissue. The passive elasticity follows a compressible Neo-Hookean model:

$$W_o^p(I_1, J) = \frac{\mu}{2}(I_1 - 3 - 2\ln J) + \frac{\lambda}{2}(1 - J)^2, \quad (4.9)$$

where μ and λ are the shear and bulk modulus of the tissue and $I_1 = \text{tr}(\mathbf{C}) = \text{tr}(\mathbf{F}^T \mathbf{F})$ is the first principal invariant of the right Cauchy-Green deformation tensor. Finally, the Piola stress tensor

from Eq.4.3 is derived as

$$\mathbf{P} = \frac{\mu}{2}[\mathbf{I} : (\mathbf{2F} - \mathbf{2F}^{-T})] + [\lambda(\mathbf{I} - \mathbf{J}) + \eta]\mathbf{JF}^{-T}. \quad (4.10)$$

The proposed equilibrium theory allows the consideration of cell-derived surface and bulk contraction. The displacement field is calculated with respect to an initial state, which corresponds to an undeformed and stress-free tissue. Mechanical stresses and tractions can be extracted from the model. Loading can be imposed either by defining non-zero contraction moduli γ and η - that correspond to the surface and bulk terms respectively - or through the application of external forces.

4.3 Results

4.3.1 Shape Evolution of Fibroblast-Populated Collagen Microtissues

To systematically study the effect of mechanical perturbations on tissue morphology, we generated arrays of 3D constrained microtissues consisting of NIH-3T3 fibroblasts encapsulated in a type I collagen matrix that were suspended inside microwells over multiple poly(dimethylsiloxane) (PDMS) cantilevers (Figure 4.1a). Fibroblasts compacted the collagen matrix and formed 3D microtissues around the caps of the cantilevers in each well (Figure 4.1b and Figure 4.2). We utilized a compact dexterous robotic micromanipulation system for the execution of well-defined mechanical interventions (introduced in chapter 3). The system allowed us to perform microsurgical operations with high precision in a repeatable fashion. The release of the microtissues from the cantilevers resulted in bulk contraction and formation of spherical tissues with a diameter of $356 \pm 18 \mu\text{m}$ within 24 h (Figure 4.1c). A similar globular equilibrium shape was attained when the tissues were engineered inside wells that did not contain cantilevers. The deviation from the rectangular shape that was defined by the geometry of the surrounding well was a clear indication that surface stresses governed the shape. There is no other physical mechanism described by the theory of non-linear elasticity that can drive this morphological change other than the development of surface stresses.

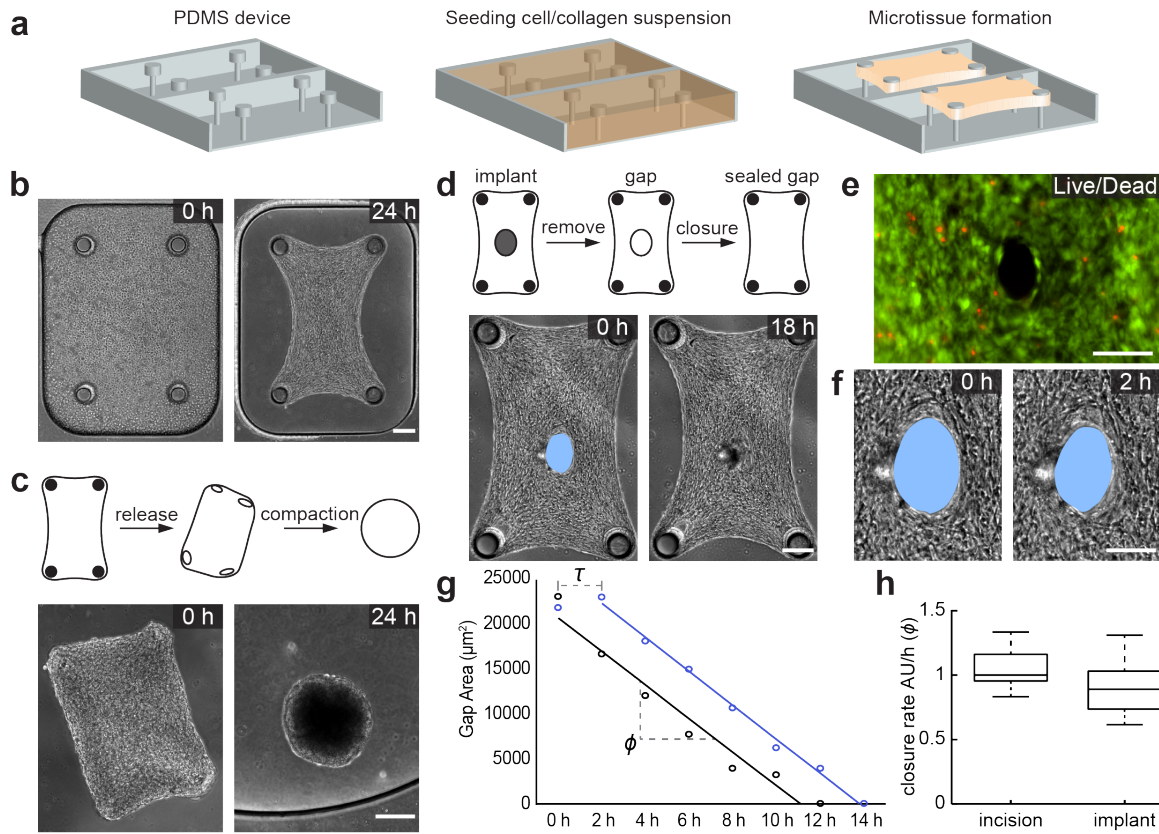


Figure 4.1: Engineered 3D fibrous microtissues display fluid-like behavior. (a) Schematic of the device and tissue engineering workflow. Fibroblasts suspended in a collagen type I solution form microtissues constrained between flexible cantilevers. (b) Representative images showing the initial and final shapes during the course of microtissue contraction. (c) Representative images showing the morphological evolution of microtissues released from the cantilevers. Free-floating microtissues contract further until they attain a spherical form. (d) Representative images showing the spontaneous closure of damage-free gaps generated using a microfabricated implant. (e) Live/dead staining of the gap area (live, green and dead, red) right after the removal of the implant. Scale bar, 100 μm . (f) Temporal sequence of micrographs of the gap area showing the immediate start of closure. Scale bar, 100 μm . (g) Graph showing the time course of the gap area for two different microtissues with gaps generated by surgical incision (blue) or removal of the implant (black). Unlike physically-damaged tissues, tissues with damage-free gaps do not show an initial lag phase (denoted by τ) due to opening and smoothening of the wound edge. Both type of gaps close overnight with comparable closure rates (ϕ), which is defined as the slope of the fitted line. (h) Box plots showing relative closure rates ($n = 10$). The median of the closure rate of incision wounds is taken as the reference and normalized to 1. Scale bars are 150 μm unless defined otherwise.

To further investigate the role of surface stresses in boundary restoration, we made full-thickness microsurgical wounds in the center of the microtissues and monitored the tissue's response. Within minutes after the incision was made, the gap widened further. Over the following few hours, the

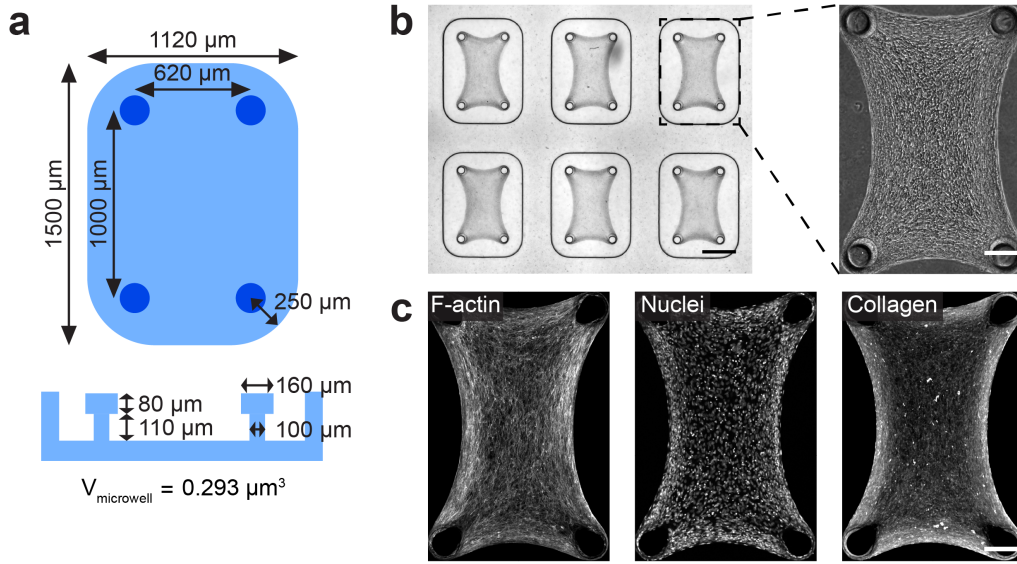


Figure 4.2: Experimental platform. (a) Schematic showing the dimensions of microwells and cantilevers. (b) Phase-contrast image of an array of engineered fibrous microtissues and the close-up view of a single construct. Scale bars, 500 μm and 150 μm . (c) Confocal micrographs of a representative microtissue stained with Phalloidin (F-actin), Hoechst (nuclei), and anti-collagen Alexa-647 (collagen fibres). Scale bar, 150 μm

rough wound edge was smoothened by the alignment and elongation of the cells along the circumferential boundary of the gap, and the wounds closed within 24h. Live/dead assays indicated that cells were physically injured by the cutting procedure (Figure 4.3). To investigate whether physical injury is required for closure, we inserted microscale implants using robotic micromanipulation into the center of the microtissues during gelation and carefully removed the implants to avoid damage to the cells residing at the interface (Figure 4.1d). Removal of the implants after overnight culture generated damage-free gaps, as indicated by the live/dead assay (Figure 4.1e). Over the course of the next 24 h, the gap progressively closed, while maintaining its shape and position (Figure 4.1f). Temporal analysis of the gap area showed a constant rate of closure ($1146 \pm 249 \mu\text{m}^2\text{h}^{-1}$) throughout the process, until the gap closed. The delay, τ , that was observed in the course of healing of incision wounds due to smoothing of boundaries was not present, which consequently resulted in a faster closure (Figure 4.1g). The closure rates of damage-free gaps and incision wounds were comparable to each other (Figure 4.1h). Together, these results indicate that physical injury is not required for closure of fibroblast-populated collagen microtissues, and therefore suggest that closure is mechanically-driven.

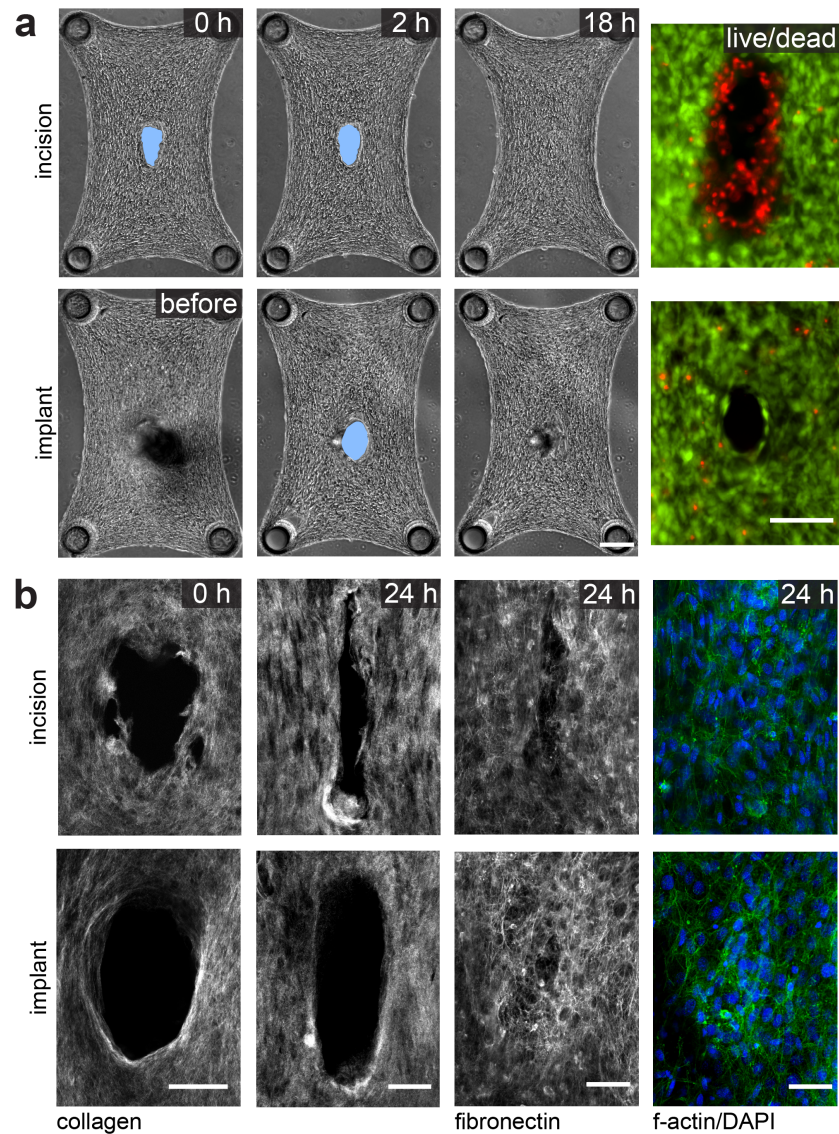


Figure 4.3: Closure of incision wounds and damage-free holes. (a) Upper panel: Micrographs showing the closure of wounds introduced by microsurgical incision. Live/dead staining of the wound area right after incision. Lower panel: Micrographs showing the closure of damage-free holes introduced by the removal of an implant. Live/dead staining of the gap right after the formation of the hole. Scale bars, 150 μm and 100 μm respectively. (b) Two-photon and confocal images of the wound area. Collagen fibres were visualized with second harmonic imaging microscopy. The tissues were stained for fibronectin, f-actin, and nuclei. Scale bar, 50 μm

4.3.2 Finite Element Simulations Capture (Re)Shaping of Microtissues

Motivated by the experimental observations, we postulate that active stresses generated by the cell contractility on the free surfaces drive the evolution of tissue shape at small scales and developed an equilibrium theory that captures the fundamental features of loading-dependent contractility of microtissues at finite strain. We implemented the weak form given in Eq.4.2 along with the constitutive equations given in Eqs.4.6 and 4.10 in the open source platform FEniCS [163, 164]. The bulk and surface contractile moduli η and γ are the only loading conditions applied during simulations (Figure 4.4a). In other words, no external mechanical force is applied other than the reaction forces. When the contractile moduli are set to zero, the material is considered to be at the reference (undeformed) state. Experimentally, this reference state corresponds to the initial state of the tissue right after the gelation of collagen matrix and prior to the application of forces by encapsulated fibroblasts. The reference configuration for the finite element simulations is chosen to represent the geometry shown in Figure 4.1b (Left). Since our proposed model is based on an equilibrium theory, the simulation results are not sensitive to the point in time when the damage is induced and the only meaningful option for the induction of damage is the mapping of the location and geometry of the damaged region in the reference state. The model then simulates the final equilibrated shape of the microtissues. For numerical stability, the values of η and γ were ramped from zero to their prescribed values during the simulations. Boundaries were clamped at the experimentally measured positions of the cantilevers and no load was applied on the outer surface. The cantilevers were considered rigid because for the chosen material composition and cantilever design, we did not observe deformation during the experiments. As the simulations are based on an equilibrium theory, only the final equilibrated state is captured for a given set of boundary conditions.

The elastic modulus and the Poisson's ratio were taken as $E = 18.33$ kPa and $\nu = 0.3$, respectively [53, 165–167]. The shear and bulk modulus μ and λ were uniquely defined using the elastic modulus and Poisson's ratio. Experimental measurements were then used to calibrate the bulk and surface contractile moduli, which were determined to be $\eta = 11$ kPa and $\gamma = 1.83$ mN mm⁻¹. The calibration was performed by fitting the parameters according to the equilibrated shape of the contracted tissue (Figure 4.1b, right) and the equilibrated shape of the tissue after the dis-

ruption of the periphery (Figure 4.7b, rightmost). First, bulk and surface activation were tuned to match the tissue shape at the equilibrated state prior to cutting. A representative example is shown in Figure 4.1b. The parameters were tuned a second time to match the tissue shape after a single cut had been made at the periphery as shown in Figure 4.7b. Shear and bulk modulus were kept constant, while bulk and surface activation were independently varied until the predicted shapes matched the experimental results.

The model recapitulated the empirical shapes of engineered microtissues at the steady-state (Figure 4.4b). While the bulk free energy resulted in the compaction of the bulk tissue with passive elasticity, the surface energy drove minimization of the surface area. The latter eliminated abrupt changes in curvature throughout the boundaries. To quantify tissue morphology, we measured the curvature κ of the outline at the long sides of the tissue (Figure 4.4c). The radius r was measured by fitting a curve along the tissue contour within the highlighted central region (Figure 4.4d). The simulated form of the microtissue is slightly less compacted but shows a higher curvature. The match between the computational and experimental results is not limited to the chosen 4-post geometry. The model captured the morphological evolution of other symmetric and asymmetric cantilever configurations.

The model provided the distribution of mechanical stresses within individual microtissues (Figure 4.4b). The results were qualitatively comparable with the predictions of bio-chemo-mechanical models including the alignment of predicted principal stress and the generation of large gradients of intratissue stress that propagate away from the cantilevers [53]. A quantitative comparison would be misleading as the previously established models remain in the small-deformation regime. Another prediction of the model was that, in accordance with experimental results, unconstrained microtissues compact close to a spherical form (Figure 4.4e). The 2D simulation resulted in the planar projection of an ellipsoid shape, an ellipse that is very close to a circle. Here, surface stresses of the solid smooth the edges and tend to minimize the surface area, as shown in the right panel in Figure 4.4e. The deviation from the rectangular shape that was defined by the geometry of the surrounding well was a clear indication that surface stresses governed the shape. Once again, there is no other physical mechanism described by the theory of non-linear elasticity that can drive this morphological change other than the development of surface stresses.

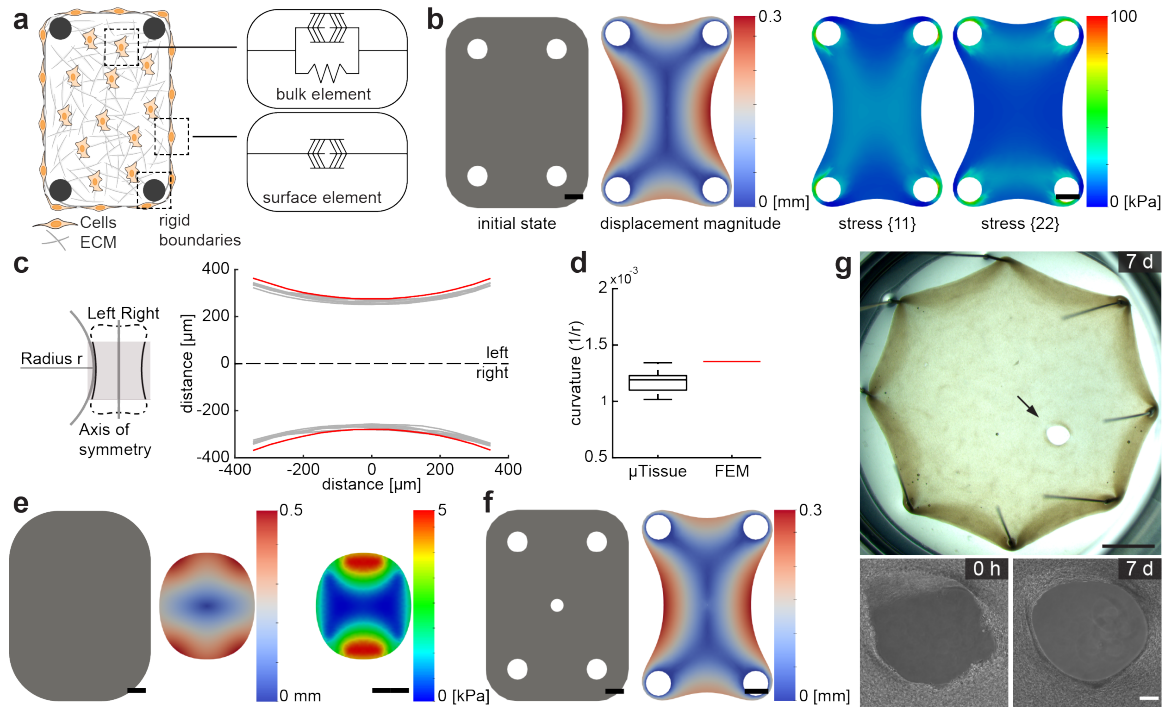


Figure 4.4: Predicted microtissue shapes resemble empirical observations. (a) Schematic description of the energy-based microtissue model. The active contractile component in the bulk represents the contractile activity of the fibroblasts embedded in the matrix. This component acts in parallel with the passive elastic element that represents the tissue stiffness. The active contractile component at the surface is a representation of the contractile activity of the fibroblasts residing on the surface. Cantilevers are modeled as rigid boundaries. (b) Finite element simulations. (Left) The initial shape where η and γ are set to zero and the equilibrium shape where η and γ are set to their calibrated values, and (Right) the distribution of principal stress. The color bars indicate displacement magnitude in mm and stress in kPa, respectively. Scale bar, 150 μm . (c) Schematic description for the measurement of curvature. (Right) The full set of reconstructed microtissue boundaries (Grey, $n = 10$) are shown along with the prediction of the simulation (Red). (d) Box plot showing curvature calculated from experimental data (Black, $n = 10$) and simulations (Red). (e) Finite element simulation of a free-floating microtissue. The shape of the untethered microtissue at the initial undeformed state and at the equilibrium state are shown along with the stress map at the equilibrium state. (f) Finite element simulation of a microtissue with a central hole that is 50 μm in diameter. The displacement magnitude shows closure of the hole at the equilibrium state. (g) Gap closure in centimeter scale tissues. Incisional wounds that are larger than 500 μm do not close after a week while wounds smaller than 100 μm spontaneously close overnight. Upper panel: Stereo microscope image of a fibroblast populated collagen tissue engineered around 8 pins in a well plate. Scale bar, 2 mm. Lower panel: Temporal sequence of phase contrast images of the wound area. Scale bars, 150 μm

To recapitulate the closed-contour wounds, a circular hole was formed in the center of the microtissue with a diameter comparable to that of the experimental assays (Figure 4.4f). This topology

defined the initial state prior to contraction. The rest of the boundary conditions and the values of the three calibrated parameters (elastic modulus, bulk and surface contractile moduli) were all kept the same. The gaps shrunk in size by several orders of magnitude at the equilibrium state, which effectively indicated closure. Taken together, modeling free energy as the superposition of a surface and a bulk component introduced predictive power to capture morphogenic evolution of tissues after mechanical perturbations that were previously inaccessible for soft tissue models.

4.3.3 Elastocapillary Length and Boundary Restoration

After discovering the dominant role of surface stresses in shaping microscale fibrous tissues, we sought to investigate whether our observations are universal or specific to a certain length scale. Elastocapillary length l_s dictates the regime where surface effects are relevant for a specific solid material [152, 153]. This number is defined as the ratio of surface stress that is given by the surface stress over shear modulus, $l_s = Y/G$, where Y is analogous to γ in the case of isotropic constant surface stress. For metals, l_s can be very small, on the order of picometers. For extremely soft materials such as microgels with loosely cross-linked polymer chains or biological tissues, l_s ranges from ~ 10 nm up to ~ 1 mm. The material properties of the microtissues studied in this work define an elastocapillary length of $l_s = 80 \mu\text{m}$. The size of the surgically-induced wounds were within this length scale, thus the surface stresses were expected to be dominant. We asked whether wounds with an order of magnitude larger sizes would spontaneously close. To test this idea, we formed centimeter scale tissues and inflicted wounds that were scaled up with the same ratio (Figure 4.4g). After an initial smoothing process around the wound edge, the gaps stayed open even after a week. These results show that although the initial geometry and the type of the wounds were similar in the microscale and mesoscale tissues, there exists a scaling factor driving the wound closure event. We conclude that the elastocapillary length scale associated with the development of surface stresses must be the dominant factor. Although this deduction does not explain the underlying biological mechanisms behind the development of surface stresses, it suggests that there are such mechanisms that drive the development of surface stresses that does not explicitly appear in our continuum theory.

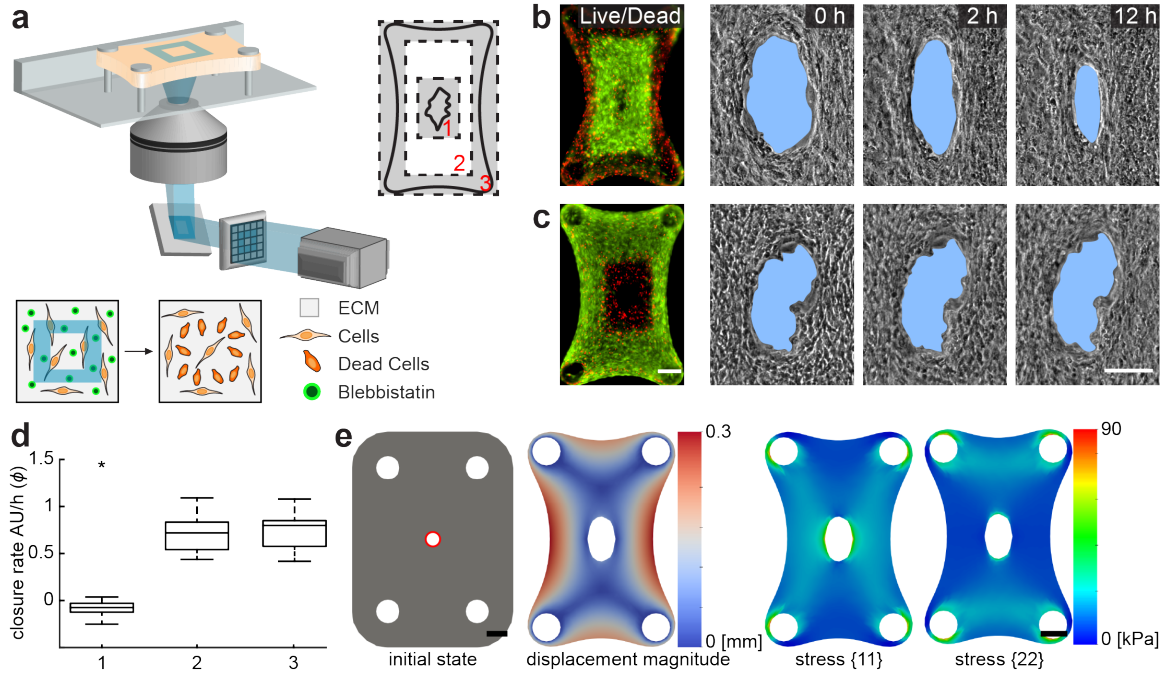


Figure 4.5: Deactivation of surface effects in the experiments and simulations. (a) Schematic illustration of the method for the spatiotemporally controlled photoconversion of blebbistatin and local killing of cells. A programmable digital micromirror display system is used for projecting blue light on predefined regions of the sample. The culture medium is supplemented with blebbistatin prior to exposure. Three areas are selected for the treatment; (1) the wound edge, (2) the region between the wound edge and the outline, and (3) the peripheral region. Live/dead staining (live, green and dead, red) and temporal sequence of wound area for microtissues that went through a treatment in (b) area 3 and (c) area 1. Scale bars, 100 μm (d) Box plot showing relative closure rates of microtissues that went through treatment in three different regions ($n = 12$). Closure rates were measured 10 hours after light exposure. The median of incision gap closure without any treatment is the reference control and corresponds to 1. (e) Finite element simulation of a microtissue with a central hole. The surface contractile modulus is set to zero around the hole throughout the simulation (highlighted in red). Displacement (left) and stress distribution (right) at the equilibrium state. Scale bars, 150 μm

4.3.4 Activity of the Fibroblasts at the Wound Edge is Indispensable for Closure

The model allows us to selectively disable surface effects while keeping the bulk contraction active. We asked whether we could stop the cellular activity at the wound edge without manipulating the cells residing away from the area and compare the experimental results with simulations. Previous work has shown that exposure of blebbistatin-treated cells to blue light (390-490 nm) causes a strong phototoxic effect that leads to a dose-dependent cell death [130]. We utilized the photo-

sensitivity of this small molecule inhibitor of myosin II for selectively de-activating cells within pre-defined regions of the microtissues. Projection of blue light (460 nm) on sub-regions of the microtissue was performed using a programmable digital mirror display (Figure 4.5a). The duration and power of blue light exposure was optimized to deliver 100% cell death within the treated area while preserving viability throughout the rest of the microtissue. Illumination with green light (525 nm) had no effect on blebbistatin-treated cells, which confirmed that the response was due to wavelength-specific photochemical conversion. For the details of the technique, we refer the reader to chapter 3.

Three distinct regions were targeted for phototoxic treatment: the outer boundary of the tissue, wound edge, and the area in between (Figure 4.5a). Following killing of the cells at the periphery, we observed a macroscale compaction due to the relaxation of surface stresses at the outer boundary of the tissue (Figure 4.5b). The coupling of mechanical activity among distant cell groups stems from the surrounding 3D fibre network. The initial compaction, on the other hand, did not influence the overall closure rate (Figure 4.5d). Likewise, targeting the cells residing between the tissue boundary and the wound edge showed no significant change in closure kinetics compared to the control. On the other hand, deactivating the cells at the wound edge within a $0.2 \times 0.3 \text{ mm}^2$ area in the centre halted the closure process (Figure 4.5c). The wound edge stayed rough and there was no tissue movement towards the gap area within the first 18 h. After the migration of surrounding cells into the area, the gap started to close, thus suggesting that cells residing at the wound edge are indispensable for closure.

To verify that build-up of stress gradients and plastic deformation of the collagen matrix during tissue formation did not play an important role in the observed behavior, we introduced the microsurgical wounds and illuminated confined areas immediately after cell seeding before the microtissue started to contract. We confirmed that gaps introduced at this stage closed over the course of tissue formation. As expected, deactivating the cells at the wound edge completely halted the closure process (Figure 4.6a). For the other two cases that involves killing cells outside the wound area, we did not observe a change in the closure rate (Figure 4.6b). Imaging of collagen, fibronectin, and cytoskeleton at the tissue boundary showed that the killing of cells at the periphery resulted in the elimination of surface stresses, which was manifested as the lack of

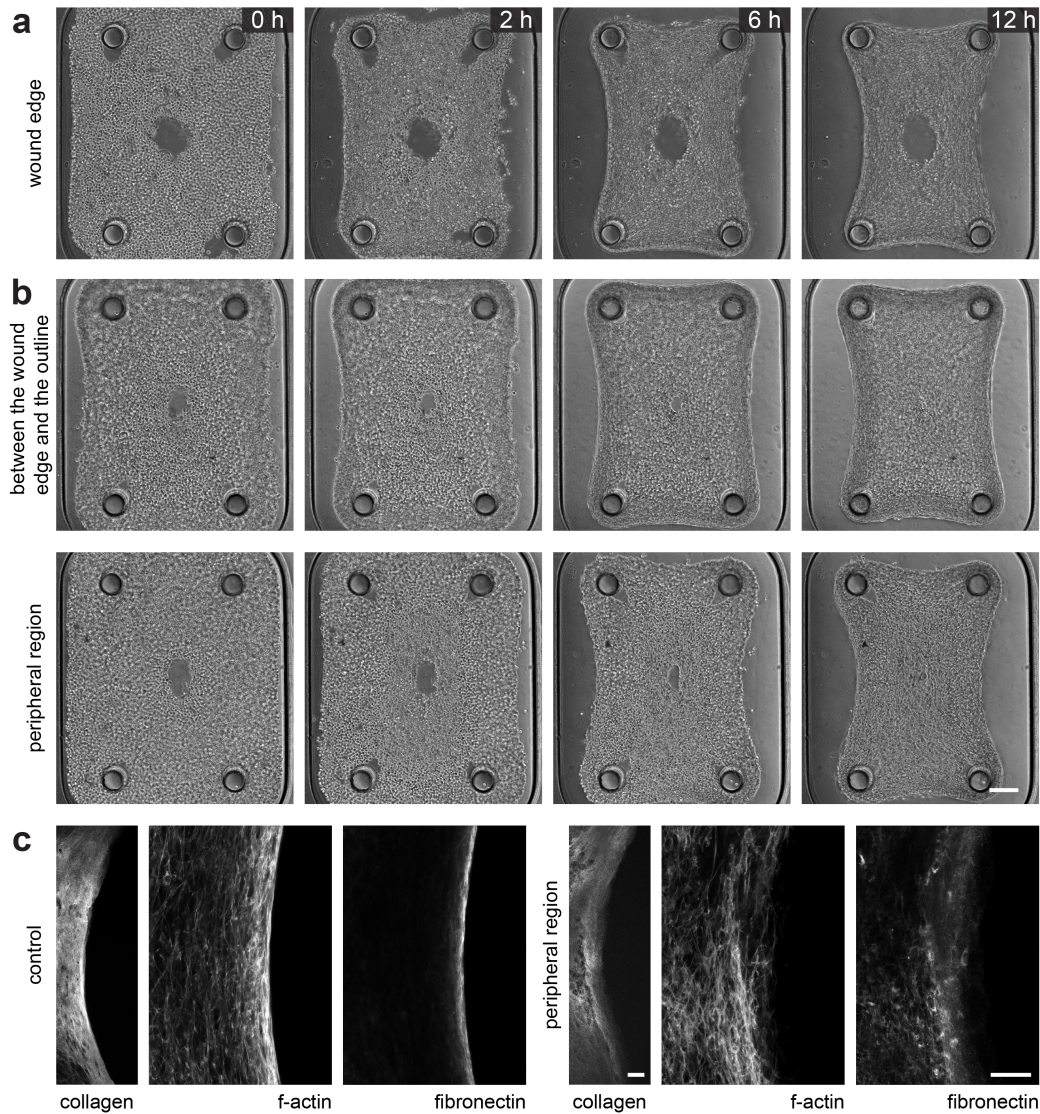


Figure 4.6: Deactivation of surface effects during tissue formation. Temporal sequence of micrographs showing the morphological changes after illumination at the (a) wound edge and (b) the region between the wound edge and the outline or the tissue periphery. Medium containing 20 μM blebbistatin was added to the culture medium 30 minutes after seeding the cell/collagen suspension. Scale bar, 150 μm . (c) Confocal sections showing collagen, F-actin, and fibronectin at the periphery of the microtissues with and without exposure at the periphery. Images are taken 14 hours after tissue formation. Scale bar, 50 μm

F-actin and matrix alignment, as well as a much sparser cell-fibronectin layer (Figure 4.6c). Taken together, these results indicate that cells at the boundary are responsible for the closure of holes via generation of surface stresses in fibrous tissues.

To recapitulate the effect of phototoxic treatment at the wound edge in the computational model,

we eliminated the surface stresses around the circular gap. The simulation results showed that circular holes formed in the middle of the tissues stayed open, and even enlarged further according to the tissue geometry (Figure 4.5e). The enlargement was expected as the geometry of the hole was solely controlled by the bulk contraction. The relatively high levels and the distribution pattern of stress around the hole at the equilibrium state showed that the tissue behaved as a sheet with a central hole under biaxial loading in the absence of surface stresses. The build up of stress around the hole resulted in observable decrease in the stress at the periphery and around the cantilevers. Taken together, these results indicate that cells at the boundary are responsible for the closure of holes via generation of surface stresses in fibrous tissues.

4.3.5 Shape Restoration at the Tissue Periphery

The restoration process may depend on the stress at the wounded side and the geometry created by the damage, which are essentially determined by the location of the surgical intervention. So far, we only studied the restoration of closed-contour defects contained within the boundaries of the microtissues. Open-contour wounds that are generated at the tissue border would present a different stress distribution and thus may lead to a different restoration process. To study this condition, a single cut was performed using robotically operated microscissors at the periphery of the microtissues (Figure 4.7a). Within minutes following the disruption of the tissue boundary, the opening was extended due to the elimination of surface stresses. In the following six hours, the concave edges on both sides of the cut were pulled towards the main body, which resulted in a smooth curve (Figure 4.7b). Again, this is a unique mechanical response that can not be explained or captured in a way other than the development of surface stresses. We observed patterns of filamentous actin around the periphery that correlated with the degree of mechanical stress (Figure 4.7c). Immediately after making the incision, F-actin staining showed disorganized filaments at the boundary, which became organized as a single tension line after 16 h and remained the same over days. We mimicked the microsurgical operation in the model by forming a slit on the side of the tissue as an initial condition. The simulated form at the equilibrium state resembled the steady-state shape of the cut microtissues (Figure 4.7d).

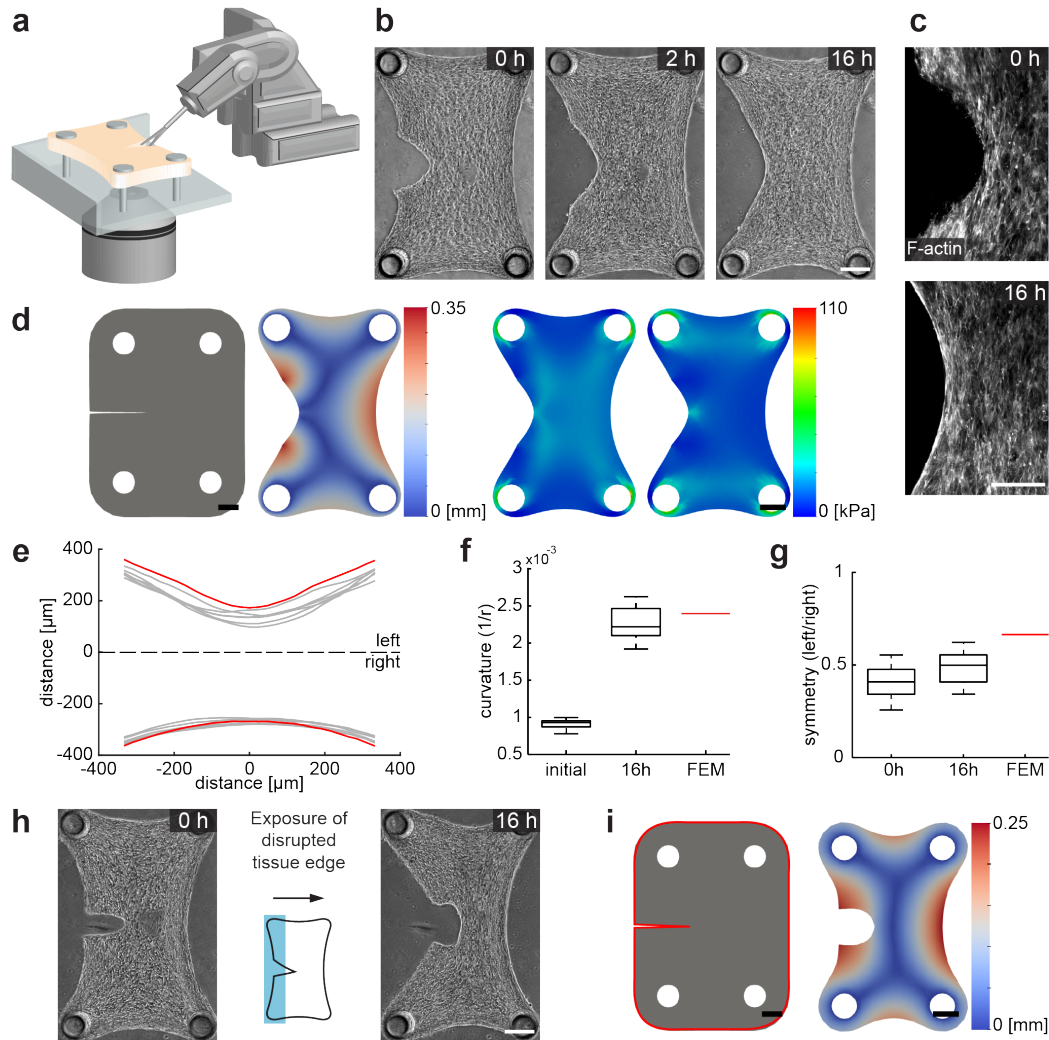


Figure 4.7: Surface stresses drive restoration at the tissue periphery. (a) Schematic illustration of the cutting of tissues using the actuated microscissors mounted on the robotic platform. (b) Temporal sequence of micrographs showing the morphological changes following the cut. (c) Immunofluorescence optical section of a microtissue showing the filamentous actin. The cellular contractility at the periphery smoothens the rough edges. (d) Finite element simulations of a microtissue with a thin notch on its side. Displacement map (Left) and simulated distribution of principal stress (Right) are shown at the equilibrium state. (e) The full set of reconstructed microtissue boundaries 16 h after surgical intervention (Grey, $n = 10$) are shown along with the prediction of the simulation (Red). (f) Box plot showing curvature at the operated side of the microtissue ($n = 12$). Red line shows the predicted curvature. (g) Box plot showing the symmetry of microtissues with respect to the longitudinal axis ($n = 12$). Red line shows the predicted symmetry. (h) Phototoxic inactivation of cells at the disrupted boundary. Representative images before and 16 hours after treatment. The schematic shows the exposed area (shaded in blue). (i) Finite element simulation of a cut microtissue. The surface contractile modulus on the periphery of the microtissue is set to zero throughout the simulation (highlighted in red). Scale bars, $150\ \mu\text{m}$

The restoration process led to the formation of a smooth convex periphery between the cantilevers in time (Figure 4.7e). The tissue contraction at the wound edge decreased the overall tissue width along the cut line and increased the curvature of the manipulated periphery compared to the initial state. The increase in curvature was quantitatively captured by the computational model (Figure 4.7f). We defined the longitudinal axis passing through center of the tissue as the axis of symmetry. The tissue shape with respect to this axis was asymmetric even after two days post-damage, which showed that, unlike closed-contour wounds, there was no internal mechanism that would drive expansion of the boundaries at the wounded side (Figure 4.7g).

The geometric evolution at the boundary suggested that surface contraction drives not only the closure of closed-contour wounds but also defects at the tissue periphery. We next investigated whether it was the contractile activity of the cells residing at the wound edge that was responsible for the remodelling of the dissected tissue parts. Killing the cells around the outer surface using phototoxic treatment significantly affected the restoration process and resulted in the formation of a cavity with an ellipsoidal shape (Figure 4.7h). The generation of this geometry was a clear indication of the absence of surface stresses on the cut region. To recapitulate the effect of phototoxic treatment, we eliminated the surface stresses around the tissue in the model. The simulation results mirrored the empirical observations in which the bulk contraction led to formation of a cavity at the cut location (Figure 4.7i). Taken together, these results show that the disruption of the external boundary of the microtissue leads to further remodeling, during which surface stresses drive recovery of a smooth outline.

4.3.6 3D Finite Element Simulations Capture 3D Shaping of Microtissues

To consider the stresses at the top and bottom surfaces of the 3D microtissues, we translated the equilibrium continuum theory to 3D. The kinematics of surfaces was updated to 3D representation to capture the full complexity, but the assumption of isotropic contributions from passive and active elements was left unchanged. The simulation error was minimized with respect to experimentally measured microtissue length, width, and thickness by setting the elastic modulus as $E = 17.38 \text{ kPa}$, the Poisson's ratio as $\nu = 0.09$, bulk contraction modulus as $\eta = 104.28 \text{ kPa}$,

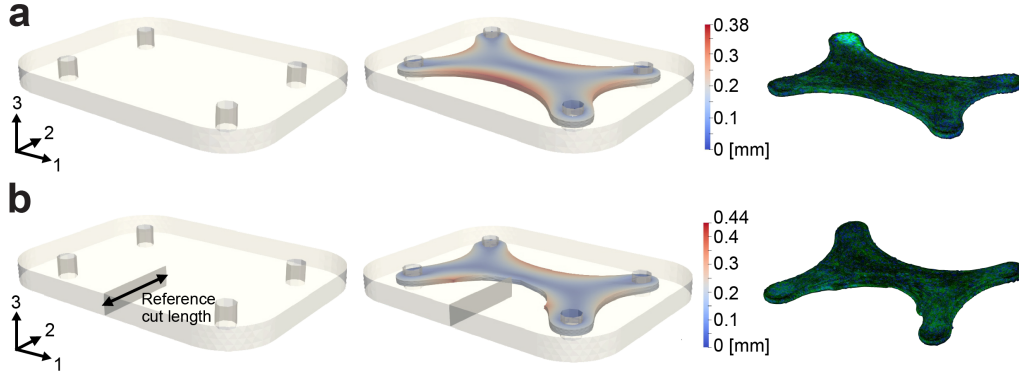


Figure 4.8: 3D simulations and reconstructed images of 3D fibrous microtissues. Undeformed (Left) and equilibrium configuration (Center) from finite element simulation. 3D reconstruction of confocal images from the tissues (Right). (a) Simulation of an unperturbed microtissue. (b) Simulation of a microtissue after a single cut had been made at the periphery. For finite element simulation the sidecut is introduced in the undeformed configuration (Left).

and surface contractile modulus as $\gamma = 1.04 \text{ mN mm}^{-1}$ (Figure 4.8a). Notably, η is an order of magnitude larger compared to the 2D simulation, which was associated to the large out-of-plane tissue deformation. The lower value for the Poisson's ratio indicated higher compressibility of the collagen matrix than assumed in 2D. Applying the same set of parameters we recapitulated the shape of cut microtissues with deviations less than 10% for all tissue dimensions (Figure 4.8b).

4.4 Discussion

During embryonic development or in 3D *in vitro* cell aggregate cultures, surface tension can drive morphological transitions, such as viscous spreading, cell sorting, and fusion of microtissues [74, 75, 99, 100]. In these biological systems, the surface tension is determined by intercellular adhesion and cortical tension [8]. Here, our results suggest that surface stresses also drive the shaping and restoration of fibrous microtissues, a mechanism that was recently proposed to shape engineered bone-mimicking microtissues [108]. Thus, the role of surface stresses in tissue morphogenesis is not restricted to embryonic and epithelial tissues, but can be extended to fibrous tissues as well.

Traditional modeling approaches follow local rearrangements inside fibrous microtissues and focus on how contractile forces drive tissue reorganization [155, 156]. Whereas these models captured

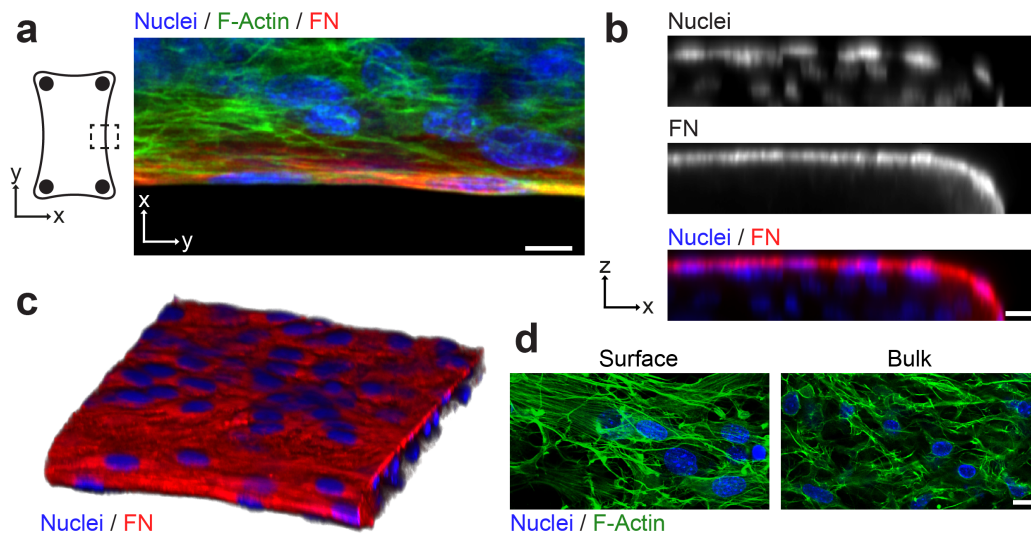


Figure 4.9: Tissue architecture suggests the presence of surface stresses. (a) Immunofluorescence optical section of the boundary shows aligned elongated cells embedded in a fibronectin rich matrix at the tissue periphery. (b) Cross-sectional view of a representative microtissue shows a gradient of fibronectin. (c) 3D reconstruction of confocal slices shows higher levels of fibronectin at the tissue periphery and smooth edges at the side. (d) Optical sections show different cytoskeletal architecture at the surface compared to cells in the bulk of a microtissue. Presence of stress fibers is an indication of higher stresses. Scale bars, 10 μm

the anisotropy and heterogeneity of a cell-compacted collagen gel, they cannot explain the macroscopic shape changes that we observed in our experiments. Introducing surface stresses through a novel and simple constitutive model did capture the observed experimental shape changes and confirmed the assumption that underlying micro-mechanical processes in the vicinity of the surface are effectively captured in the continuum scale. The following question arises, what generates surface stresses in engineered collagen microtissues? Recent work has shed light on how fibroblasts encapsulated inside collagen gels migrate towards and self-organize at the surface of the microtissues. The compaction of the collagen network coincides with the assembly of an extended and fibrillar fibronectin mesh surrounding the bulk tissue [159]. Gradients of fibronectin conformations generated from the core to the periphery guides migration of fibroblasts to the tissue surface [160]. As a result, the spatial organization of cells and ECM generates a biphasic core-shell architecture, a compressible collagen tissue with low cell density surrounded by a dense fibronectin-cell composite. The fibronectin matrix provides the overall cohesion for the microtissue and the effective transmission of forces between different layers.

In our computational model, the contraction of the collagen gel is driven by the bulk contraction modulus η while the surface contractile modulus γ represents the loading generated by the fibroblast activity (i.e. migration, contractility, and fibronectin remodeling) at the surface. The magnitude of γ is significantly higher than the surface tension values reported in the literature for epithelial monolayers and embryonic tissues [99, 105, 168–170]. These articles refer either to 3D cell clusters interacting primarily with cell-cell contacts [99] or epithelial monolayers patterned on isotropic, linear elastic surfaces [105, 168–170], whereas surface stresses in our experimental model are generated through fibroblast-ECM interactions on the surface of a compressible and plastically deformable solid. It is important to note that the active tensile modulus of an epithelial monolayer spans two orders of magnitude across cell types (ranging from 0.58 ± 0.26 to 180 ± 65 nN mm⁻¹) and it depends on the activity state of the cells as well as the composition of the underlying collagen matrix [105, 170]. Fibroblasts in our microtissue model may build up significantly higher stresses on the tissue surface because fibrous networks impart complex mechanical characteristics due to nonlinear stiffening in response to loading and differential rigidity in axial versus transverse directions with respect to fibre orientation [171]. Furthermore, experiments with free-floating, fibroblast-populated collagen lattices have shown that after the compaction of the gel, fibroblasts within the outermost region begin to differentiate into myofibroblasts, which is associated with the generation of stress fibers and the ability to sustain a larger contractility [172]. As a result, significant tensile stresses may develop in the outer region of the contracted gel while cells reorient and compact the collagen. Mechanical modelling of these constructs suggested that the outermost region experiences a tensile circumferential stress and the inner-most region experiences a compressive stress [55]. These observations are in accordance with our findings (Figure 4.9) and we postulate that the increased density of fibroblasts at the surface, changes in their phenotype that leads to elevated contractility, and the remodeling of the fibronectin matrix together lead to a high tensile circumferential stress, which appears as a high γ value in our model.

The presented modeling paradigm complies with the results of recent experiments with very soft gels, which showed that the relative importance of surface stress and bulk elasticity is a matter of length scale. Furthermore, interfacial stresses can deform solid bodies in their bulk at microscale [152, 153]. The model required fitting of only two parameters for the prediction of the equilib-

rium shape of free-standing and constrained microtissues with arbitrary initial geometry. During the simulation of surgical cuts, we observed a deviation from the empirical data as the perturbed boundary did not become a smooth line (Figure 4.7d). This issue may be addressed with the incorporation of additional physical properties of collagen networks such as anisotropy and plasticity [52, 173, 174]. Furthermore, a more accurate constitutive law can be derived for cell-driven surface contractility in viscoelastic solids. The constitutive relation prescribed on the tissue surface follows Eq.4.7, which leads to a constant surface stresses much like a fluid. To move further, a strain-dependent surface stress can be introduced, which will mitigate the issue of surface stresses increasing uniformly over the whole surface and allow for local changes of surface stress. The modeling of these nonlinear properties would also allow the simulation of intermediate morphological states during self-repair and prediction of the effect of multiple consecutive surgical operations.

To conclude, through experimental and theoretical developments, this study confirms that contractile collagen microtissues develop surface stresses and correlates them to underlying biological mechanisms. The developed surface stresses have a significant effect on the morphological response after damage and follow an elastocapillary lengthscale. It also provides new experimental tools and a novel computational framework to examine how cells coordinate shaping after mechanical perturbations. The robotic manipulation methods introduced here provide high-throughput, precision and repeatability, which together facilitate data acquisition and testing of the predictive power of computational models. Extension of the work to study the shaping of fibrous tissue constructs with multiple cell types of different contractile activity and spatial distribution would be of fundamental relevance to developmental biology and regenerative medicine. In natural tissues, the activation of cells is not constant but regulated by the mechanical properties of the surrounding tissue. These nonlinear effects can be incorporated into the computational model to provide insights into their contribution to tissue mechanics. The model can be further validated with the experimental measurement of surface and bulk stresses in fibrous tissues.

4.5 Materials and Methods

Device fabrication

Tissue gauges were fabricated as described previously [53, 145]. Briefly, polydimethylsiloxane (PDMS, Sylgard 184, Dow-Corning) substrates were molded from SU-8 masters. The devices were then sterilized in 70% ethanol followed by UV exposure for 15 minutes. Before cell seeding, the devices were treated with 0.02% Pluronic-F127 (Sigma) solution for 10 minutes at room temperature.

Cell culture

NIH 3T3 fibroblast (Sigma) were cultured in DMEM GlutaMAX (Life Technologies) supplemented with 10% FBS (Life Technologies) and 1% Penicillin-Streptomycin (Life Technologies). Cells were passaged every 2-3 days using trypsin 0.25% EDTA (Life Technologies) and not kept longer than 20 passages. All experiments were done with cells that were tested negative for mycoplasma.

Microtissue model

One million cells were suspended in $2 \text{ mg} \cdot \text{ml}^{-1}$ liquid neutralized collagen type I from rat tail (Corning BV Life Sciences) and seeded in the device. The entire assembly was centrifuged to drive cells into the chambers containing the cantilevers. Excess solution was then removed, leaving only the chambers filled with liquid. The device was centrifuged once again in an inverted configuration to move the cells closer to the the cap of the cantilevers prior to polymerization. A few hours after polymerization, we observed the spontaneous contraction of the collagen matrix by the cells. Cantilevers incorporated within each chamber spatially constricted the contraction of the collagen matrix.

Large-scale tissue formation

Boundary conditions were set by pinning dissection pins (FineScienceTools) inside the wells of a 24 well plate (1.9 cm^2) coated with PDMS. Wells were sterilized with ethanol and UV treatment. To prevent cell adhesion, devices were incubated in 0.02% Pluronic-F127 (Sigma) for 10 minutes

at room temperature. One million 3T3 cells suspended in $2 \text{ mg}\cdot\text{ml}^{-1}$ liquid neutralized collagen type I from rat tail were seeded into the wells. The tissues spontaneously formed within 24 h.

Robotic micromanipulation

The robotic system used for this work is introduced in chapter 3. Full-thickness incisional wounds were generated using a dissection pin (FineScienceTools) while microscissors (Alcon) were used for cutting the boundaries of the microtissues. Microimplants were fabricated from glass substrates and PDMS elastomer. Glass capillaries were filled with uncured PDMS using capillary action and subsequently heated for curing. Microimplants were inserted into the microtissues using microtweezers (Alcon).

Microscopy and quantitative image analysis

For wide field imaging, microtissues were labeled with Hoechst 33342 (ThermoFisher) to visualize the nuclei of the cells. Phase contrast and fluorescent images were captured every hour for 20 h with an ORCA-Flash4.0 digital CMOS camera (Hamamatsu) and a Plan Fluor 10x objective mounted on the microscope equipped with a live cell incubator (Life Imaging Services). Time-lapse images were segmented using a semi-automated processing software in ImageJ for the quantification of gap and tissue size. Closure rate and curvature were measured by a custom script written in Matlab (Mathworks, MA). The script calculated the slope of the line that fitted gap size data recorded over time. For curvature measurements, the script accepted the location of the micropillars as the reference to define the global center point and the axis of symmetry. The outline of the microtissues were digitally reconstructed by selecting points along the boundaries every $25 \text{ }\mu\text{m}$. The curvature was calculated from the radius of the circle that fitted those points. Symmetry was defined as the ratio of the average distance between the points that define the left and right boundaries and the symmetry axis.

Confocal and multiphoton microscopy

Microtissues were fixed with 4% formaldehyde, permeabilized with 0.2% Triton X-100, and blocked in 10% Goat serum for 1 h at RT. Samples were subsequently incubated with antibodies against

fibronectin (Abcam, ab2413) and collagen (Merck Millipore, AB755P) overnight at 4°C and detected with goat anti-rabbit Alexa-647 (1:100, ThermoFisher) conjugated antibodies. Fluorescently labelled microtissues were imaged using an inverted confocal microscope (Zeiss LSM 700) equipped with a 20x objective. Non-labelled collagen type I was visualized by second-harmonic imaging microscopy. Images were taken with an upright Leica DM 6000 CFS microscope equipped with a 20x WI objective and HeNe laser source (excitation 800 nm, second-harmonic light detection with a 400/15 cut off filter). Representative images are z-projections of 3 to 5 images.

Viability assay

For staining live and dead cells, the Viability/Cytotoxicity Assay Kit (Biotium) was applied according to manufacturer's protocol. Briefly, a staining solution of 2 µM Calcein AM as living cell stain (green) and 4 µM Ethidium homodimer III (EthDIII) as dead cell stain (red) was prepared in PBS. Microtissues were incubated for 40 minutes in the staining solution, washed three times, and resuspended in PBS solution.

Statistical analysis

All values were given as mean \pm s.e.m. or shown as box plots. The central mark within the box indicates the median and the borders are the first and third quartiles. Whiskers were shown as dashed lines. Statistical significance was calculated with unpaired Student's t-test. P-values greater than 0.05 were considered to be statistically not significant.

Chapter 5

Tissue Sculpting by Mechanically Induced Solid-Fluid Transitions

The work presented in this chapter is going to be submitted as

Erik Mailand, Ece Özelçi, Jaemin Kim, Odysseas Chaliotis, Nikolaos Bouklas, and Mahmut Selman Sakar. Tissue sculpting by mechanically induced solid-fluid transitions.

5.1 Introduction

Engineering designer tissues is instrumental for understanding embryonic development, opening new avenues in regenerative medicine, modelling disease biology *in vitro*, and building biological machines [175]. The acquired knowledge may even inspire the discovery of reconfigurable synthetic material systems. However, major challenges to bringing tissue morphogenesis under engineering control arise from the multiscale dynamics of biological processes, which involve distributed contractile forces and motion at microscale that add up to macroscale changes in morphology [3]. Furthermore, structural and mechanical changes occur both in the self-organizing cell collectives and the surrounding extracellular matrix (ECM) at a wide range of time scales. Seminal work has shown that formation of organs during embryonic development is coordinated by tissue mechanics, and engineered tissues could be programmed to recapitulate some of these morphogenic episodes[1, 38].

Pottery is one of the oldest human inventions. Objects with complex shapes are sculpted from clay using various additive and subtractive techniques including moulding, carving, and assembling. Furthermore, the plasticity of the disordered soft material enables modelling of structures from rigid templates. Drying and firing the finished pieces inside a kiln remove the water molecules and bond the suspended particles together, essentially driving a jamming transition. Epithelial sheets have been shown to display analogous properties where the living material locally and reversibly switches from solid-like to fluid-like state while maintaining overall mechanical integrity [25, 69]. The source of epithelial plasticity and fluid behaviour resides in the ability to actively remodel junctions during spatiotemporally controlled proliferation, extrusion, and intercalation of constituent cells [176]. This fluidization process is a consequence of epithelial to mesenchymal and jamming transitions, which has been shown to be triggered by external mechanical loading or administration of growth factors [114].

The true potential of epithelium in driving embryonic morphogenesis is revealed with the emergence of a mesenchyme that is comprised of loosely packed migratory cells that are suspended in an ECM scaffold. A mismatch in strains between the epithelium and the underlying mesenchyme results in mechanical instabilities and tissue folding, which could be generated by the differential growth or local contraction of the tissue layers [41, 177]. We postulated that coating the surface of

a bulk ECM gel with epithelial cells would transform the solid into shape-programmable living matter. The soft gel would provide a substrate on which epithelium could spread and organize, and later solidify into a thin shell that stabilizes the tissue shape. Elastic core would allow bulk mechanical manipulation as a means to drive spatially defined solid to fluid transitions in the casting, which would enable re-shaping of the tissue through episodes of plastic deformation. Local fluidization may also allow joining tissue pieces together for building more complex constructs. Finally, fluidized epithelium generates surface stresses that can deform the soft gel, therefore autonomous tissue folding could be guided along prescribed trajectories by locally perturbing the cohesion of the shell.

Here, we introduce a tissue engineering framework that harnesses mechanics of epithelia. Our method bridges the precision and versatility of traditional manufacturing techniques with the programmable and decentralized nature of the biological self-organization. The raw composite biomaterial, consisting of a collagen and epithelial cells, is cast inside microfabricated moulds in a way that the cells sandwich the soft and compressible gel. Cells spread, migrate, and proliferate to cover the whole gel surface and, in the meantime, exert traction forces on the underlying matrix that are high enough to deform the bulk tissue. As the tissue compacts, increasing cell density leads to reinforcement of tight junctions and jamming where cells cannot overcome the yield stress to pass by each other and thus become immobilized. The equilibrated tissue preserves its shape for weeks. Yet, it is amenable to further shaping upon dynamic fluidization of the epithelium through mechanical loading, cutting, and punching. The enlisted mechanical operations locally increase cell kinetics by creating new tissue boundaries while transient solid to fluid transitions enable plastic forming, carving, assembly of multibody structures, and introduction of folds. The experiments reveal a spectrum of 3D morphologies, demonstrating the versatility of our engineering framework.

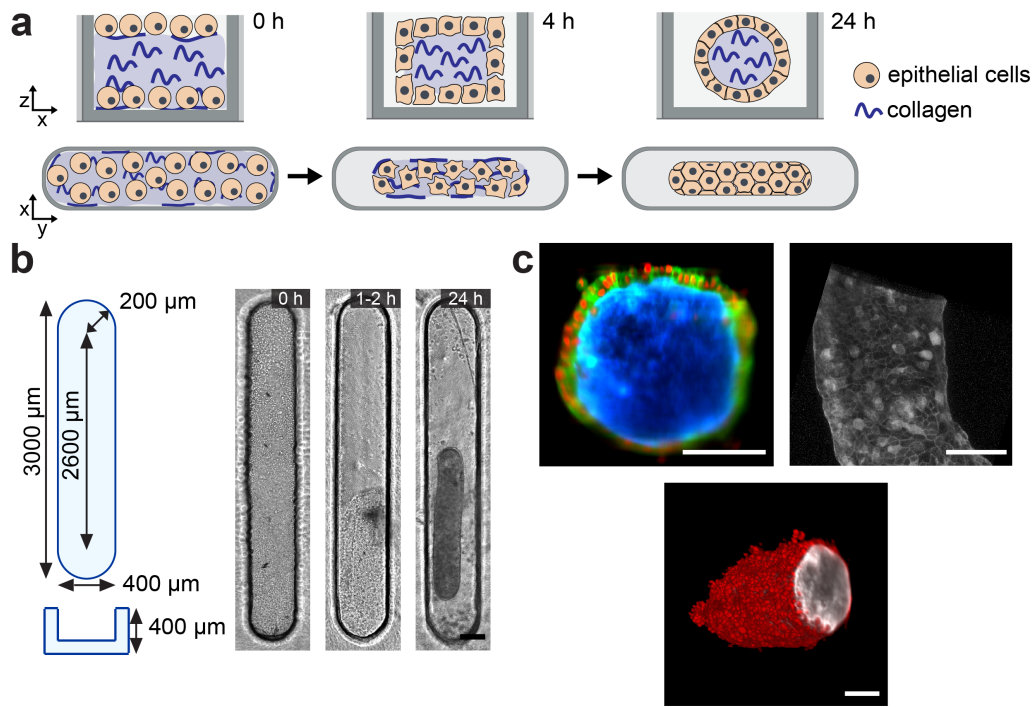


Figure 5.1: Self-assembly of capsule-shaped microtissue. (a) Schematic of self-assembly process. After collagen polymerization, epithelial cells compact the collagen gel (blue) and self-organize into a coherent shell within 24 hours. The shape of the microtissue is stable over weeks. (b) Left: Schematic showing the dimensions of microwells. Right: Representative pictures of self-assembly process in microwells. Scale bar, 100 μm. (c) Microtissue architecture 48 hours after assembly. Microtissues are formed with MDCKII cells that stably express eGFP-H2B and mCherry-Actin. Upper panel: Cross-sectional view and surface of microtissue. Nuclei is shown in red, actin in green or grey respectively, and fluorescent labelled collagen (collagen-647) in blue. Lower panel: 3D reconstruction of light-sheet images showing the tip of a microtissue. Nuclei is shown in red and collagen-647 in grey. Scale bars, 100 μm

5.2 Results

5.2.1 Fluid to Solid Transition Stabilizes Engineered Tissue Morphology

The sculpturing process starts with the moulding of a self-stabilizing and reconfigurable microtissue. To facilitate detailed quantitative analysis, we fabricated a high-throughput device that is compatible with live imaging using additive manufacturing and replica moulding. Wells with a stadium geometry were filled with Madin-Darby Canine Kidney cells (MDCK sub-type II or MDCKII) in a suspension of 1 mg ml^{-1} collagen type I using centrifugation and de-wetting steps (Figure 5.1a and b). This process ensured that cell-laden gels were entrapped inside the wells, and

the cells were dispersed close to the bottom surface of the wells. Immediately after the gelation of collagen, we seeded cells in a suspension of culture medium at a density optimized to cover the top surface. The initial cell distribution instructed the cells to position at the tissue surface. Cell-derived surface stresses compacted the cross-sectional area of the microtissue by 80% within the first 24 hours (Figure 5.1b and Figure 5.2a). The whole surface of the stadium-shaped tissue was covered with an epithelial monolayer after 48 hours where the cells were regularly organized following the characteristic honeycomb pattern (Figure 5.1c). Notably, the cross-sectional area of the microtissue enlarged by 60% during the next five days while maintaining its shape (Figure 5.2a, b, and c).

We hypothesized that the transient expansion of the microtissue was caused by either cellular rearrangements or tissue growth due to cell proliferation. Blocking proliferation using mitogenic inhibitors Aphidicolin or Mitomycin C did not influence the overall expansion process (Figure 5.2d). Inhibition of non-muscle myosin II activity with Blebbistatin or disrupting actin cytoskeleton with Cytochalasin D did not increase the rate of expansion. Surprisingly, microtissues treated with Cytochalasin D stopped expanding, even though we expected the monolayer to lose its cohesion. Further experiments are required for discovering the mechanism of this morphogenic episode. With the existing observations, we postulate that structural remodelling of the monolayer is responsible for the enlargement of the surface area.

To reveal the key role of the glassy phase transition associated with increasing cell density, we performed experiments with two other cell lines: parental MDCK that was shown to present mesenchymal characteristics ([178]) and NIH-3T3 fibroblasts. First, we recorded time-lapse movies of monolayers cultured on flat collagen substrate. As expected, MDCKII cells drastically reduced activity upon reaching confluency, while MDCK and 3T3 cells continued to migrate and exchange neighbours (Figure 5.3a and b). Next, we engineered 3D tissues from MDCK and 3T3 cells using the protocol described in Figure 5.1a. MDCK cells formed microtissues with an initially high aspect ratio but the tissues rapidly compacted over the following days and eventually started to gain an isotropic shape. Fibroblasts were much more aggressive in their response and turned the tissues into almost perfect spheres within a day of culture (Figure 5.2a, b, and c). Taken together, these experiments showed that prescribing a long-lasting tissue morphology relies on the formation

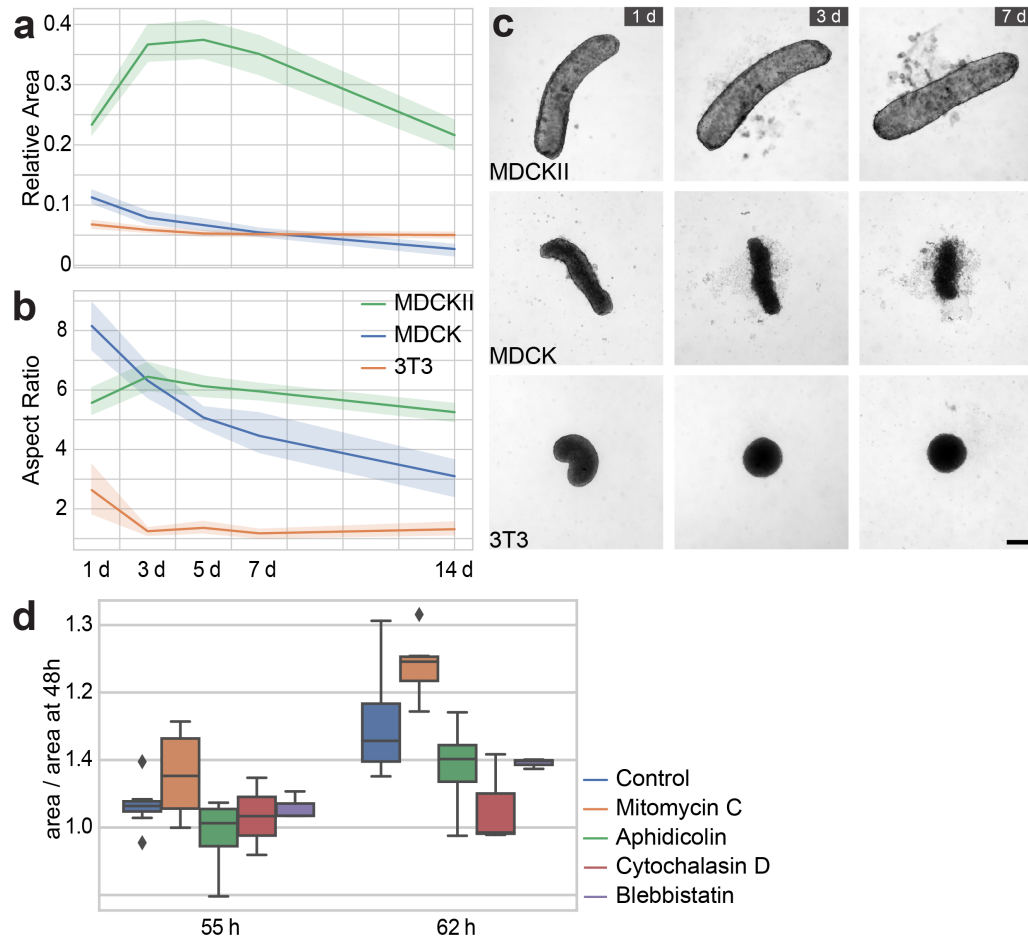


Figure 5.2: Stability of engineered microtissues. (a) Graph showing vertical cross-sectional area of microtissues relative to the area of the microwell over days. (b) Graph showing the aspect ratio of microtissues (length divided by width) over days. Mean and 95% confidence interval are shown measured on day 1, 3, 5, 7, and 14. MDCKII (green), MDCK (blue), and 3T3-fibroblasts (red) (N=2, n=12). (c) Representative images showing morphological evolution over time of MDCKII, MDCK, and 3T3 fibroblasts. (d) Boxplot showing expansion of microtissues under pharmacological drugs added 2 days after tissue formation. Vertical cross-sectional area of microtissues relative to their area 2 days after tissue formation is shown. Control (blue), 5 μ g/ml Mitomycin C (orange), 1 μ g/ml Aphidicolin (green), 4 μ M Cytochalasin D (red), 10 μ M Blebbistatin (purple). Line in the box represents the median and the borders the first and third quartiles. Whiskers extend to points that lie within 1.5 times the interquartile range (N=1, n=3). Scale bar, 200 μ m

of a jammed monolayer, which coincides with a transition from traction forces to intercellular stresses.

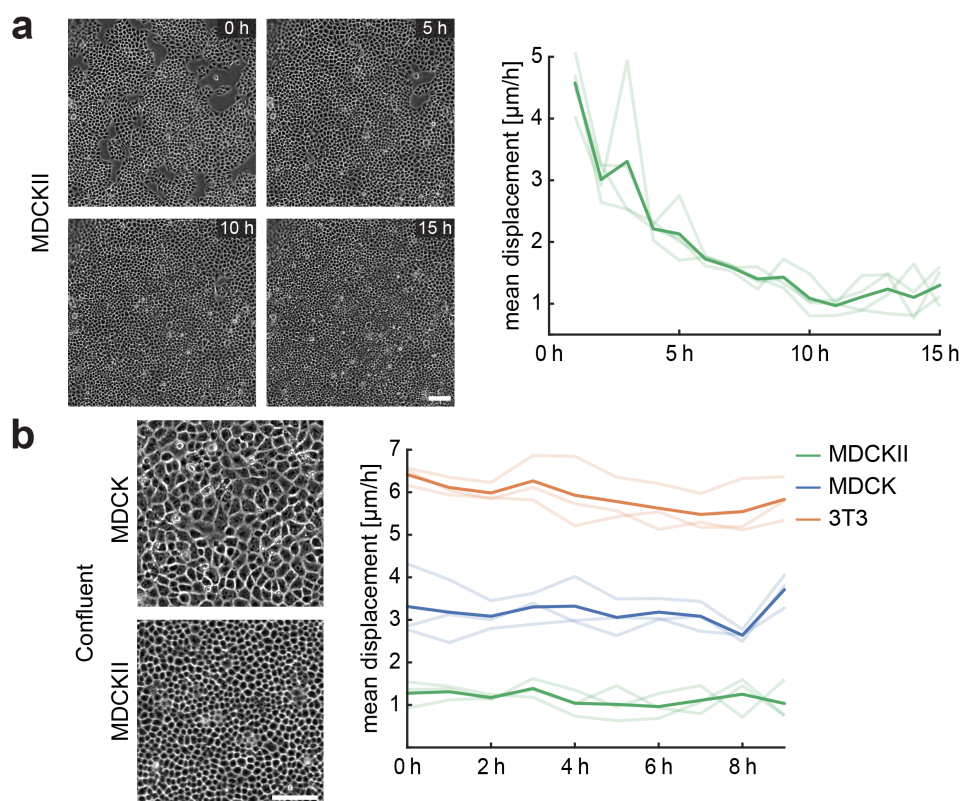


Figure 5.3: Slowdown of motion in MDCKII monolayer. Particle image velocimetry was applied to quantify cell motion over time in an area of $850\mu\text{m} \times 850\mu\text{m}$. The graphs show the mean of all velocity values within a frame for every hour. Transparent lines show single samples and the bold line the mean. (a) Left: Representative micrographs of MDCKII cells covering free areas and decreasing in size over time. Right: Graph showing the arrest of cell motion over the given time ($N=1$, $n=4$). (b) Left: At confluency, parental MDCK show larger and more dispersed morphology compared to MDCKII. Right: 3T3 fibroblasts as well as parental MDCK cells show higher motility than MDCKII cells at confluency ($N=1$, $n=3$). Scale bars, $100\mu\text{m}$

5.2.2 Slip Casting and Plastic Forming

Formation of stadium-shaped microtissues from MDCKII cells promoted the conception that the raw biomaterial may take the shape of any mould upon casting. As demonstrated by the first set of experiments, the initial tissue compaction reduces the original size defined by the dimensions of the well, which must be considered in the design process. Importantly, the overall well shape is expected to be preserved unless surface stresses are non-uniformly distributed. To systematically explore the design space, we fabricated wells with a variety of geometries that included convex and concave edges. Tissue area from microtissues formed with 2 mg ml^{-1} collagen reduced about 60% during the formation phase and the prescribed shape was preserved for at least

three weeks (Figure 5.4a). Elastocapillary effects were more dominant in smaller tissues, leading to boundaries with lower curvature (Figure 5.4b).

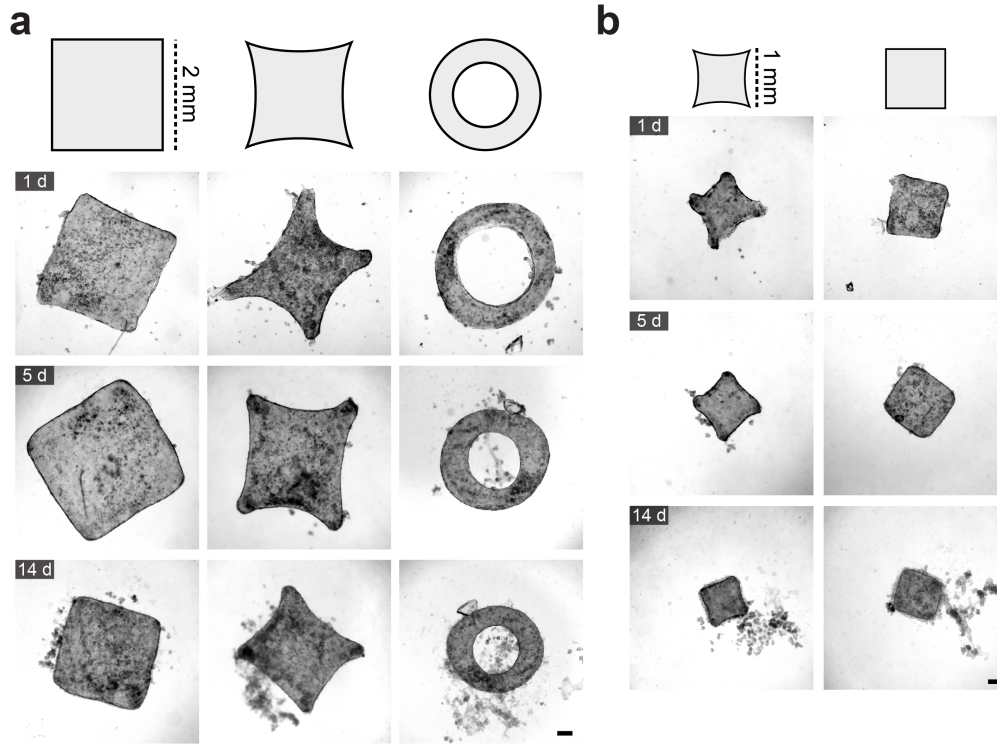


Figure 5.4: Slip casting and plastic forming of microtissues. (a) Microtissues are formed in microwells with the shape of square, square with sides curving inwards, and ring. Representatives are shown at day 1, 5, and 14. (b) Microtissues molded from molds half the size of (a). Tissue formation is not restricted to a given size but elastocapillary effects are more emphasized with reduction in size. Scale bars, 200 μm .

5.2.3 Subtractive Sculpturing using Plastic Microsurgery

Experiments with *in vitro* cell culture assays and fruit fly embryos have shown that regionalized tissue fluidization is required for wound repair and closure of physical gaps. The disruption of the tissue integrity initiates epithelial sheet movement at the leading edge in various forms, including the formation of a contractile supracellular actomyosin cable surrounding the gap [28], cell intercalation [34], and cell crawling with lamellipodia protrusion on the underlying substratum [19]. These morphogenic processes promptly seal the defects and restore the physiological function of the tissue. Inspired by these studies, we hypothesized that moulded microtissues could be shaped further following the principles of subtractive manufacturing by removing solid material.

We cut out pieces from microtissues with surgical instruments mounted on a teleoperated microrobotic system. For the details of the robot, we refer the reader to chapter 3. The boundaries of the microtissue were modified by making small cuts using surgical scissors (Figure 5.5a). The cuts were engraved into the microtissues with the flow of the epithelium to the exposed areas of the collagen gel. Likewise, the microtissue was pierced using a biopsy punch, which formed a stabilized perforating hole. In both cases, a phase transition was induced by the disruption of the monolayer, essentially forcing the cells at the operated region to migrate and close the gap. The cutting was extended to splitting the tissue into pieces, where each piece reconstructed its epithelial skin and stabilized its shape (Figure 5.5b).

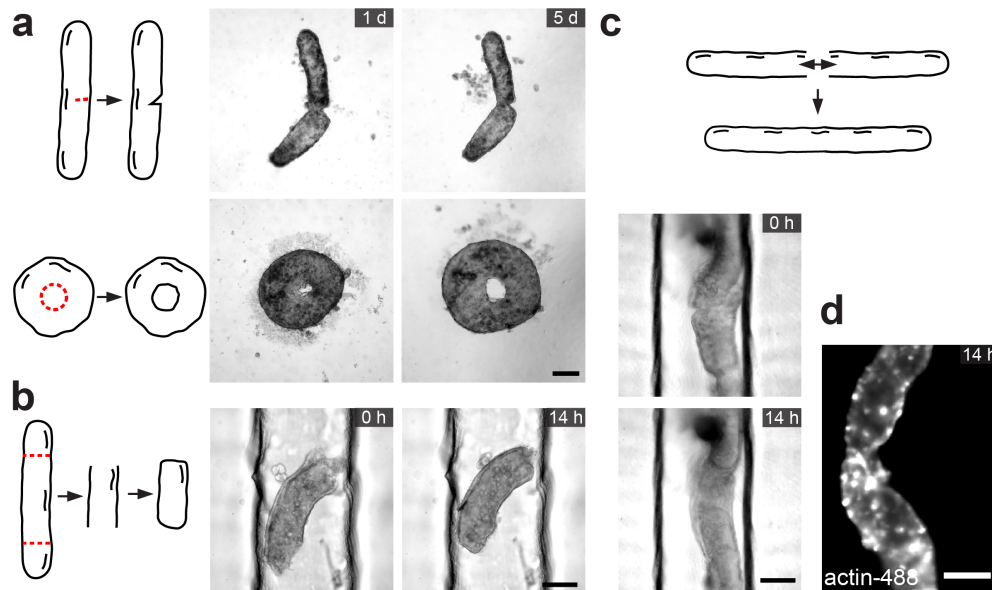


Figure 5.5: Plastic microsurgery and microtissue assembly. (a) Microtissues are cut from the side (upper panel) or pierced with a biopsy punch (lower panel). The altered shape stabilized. (b) Microtissue ends are removed with microscissors and free ends seal over the course of 14 hours. (c) Microtissues with one end removed are placed next to each other with the open end facing each other. Micrographs show the fusion of microtissues. (d) Actin is shown of fused microtissues 14 hours later. Scale bars, 200 μm

5.2.4 Assembling Complex Tissues from Building Blocks

Self-healing of the epithelium motivated the idea that two tissue pieces could be attached to each other. The surfaces that are supposed to bond together must be activated (i.e. interacting sides must be cut prior to the assembly) for the migration and fusion of the epithelium. Indeed, phys-

ically pushing two activated pieces end-to-end for 14 hours was sufficient to initiate tissue fusion (Figure 5.5c and d). Pushing together non-activated pieces with an intact shell also initiated bonding but preliminary results have shown that the fusion of activated ends is significantly stronger against tensile loading. However, collagen cores of individual pieces do not fuse, thus a tissue formed through assembly would be weaker compared to a single-piece moulded counterpart. Assembly, on the other hand, opens a design space where 3D complex morphologies are feasible.

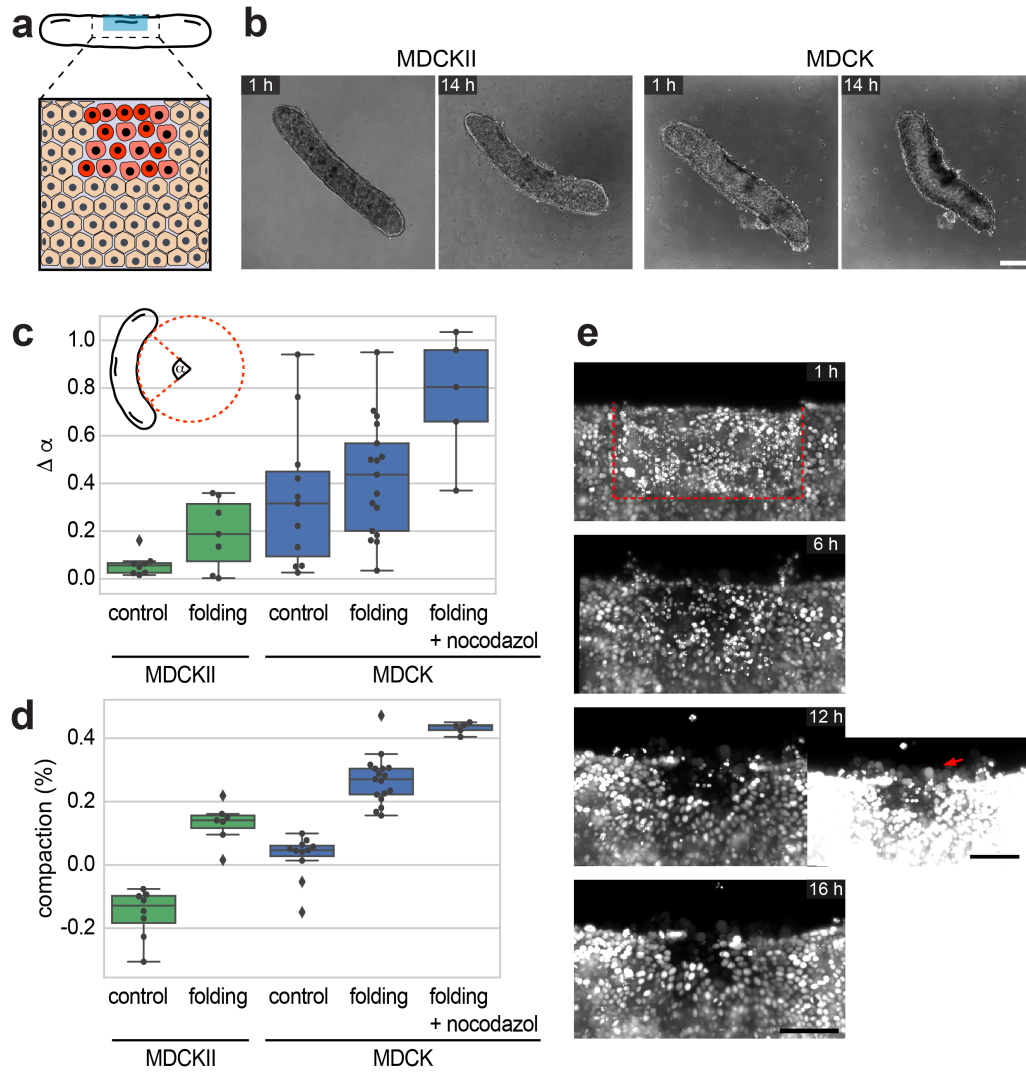


Figure 5.6: Tissue folding through cell death. (a) Schematic of light induced cell death at the tissue periphery (dead cells in red) (b) Microtissue folds within 14 hours after local illumination (MDCKII (Left) and MDCK (Right)). Scale bar, 200 μm . (c) Boxplot showing folding of MDCKII and MDCK microtissues not exposed to light (control) and exposed to an area of 200 μm (folding), as well as MDCK microtissues exposed to light but treated with nocodazol (folding + nocodazol). Inset: Schematic describing quantification of tissue folding. After fitting a circle to the median line of the microtissue, the central angle α is used to compare the initial state (before illumination) with the end state (14 h after illumination) ($\Delta\alpha = \alpha_{\text{after}} - \alpha_{\text{before}}$). (d) Boxplot showing compaction rates of microtissues quantified in (c). Compaction is quantified as $1 - (\text{Area}_{\text{after}}/\text{Area}_{\text{before}})$. Line in the box represents the median and the borders the first and third quartiles. Whiskers extend to points that lie within 1.5 times the interquartile range. Points represent single microtissues (N=2 for MDCKII, N=3 for MDCK, and N=1 for MDCK folding + nocodazol). (e) Micrographs from light-sheet microscopy showing cell nuclei. Inset at 12 hours: Dying cells show reduced expression of fluorescent nuclei label and get extruded (red arrow). Scale bar, 50 μm

5.2.5 Tissue Folding Through Spatially Patterned Cell Death

Local fluidization of epithelium leads to a shift in force balance with increasing surface stresses. We observed that in every re-epithelization process, the collagen core was deformed locally in a way to minimize surface energy. We asked whether these forces could be harnessed to initiate a more drastic change in the tissue shape. Ideally, the manipulation should activate the epithelium without damaging the underlying collagen gel. In our previous work, we introduced a technique to kill cells in a spatiotemporally resolved fashion using a photochemical conversion process. The technique is based on the phototoxicity of the small molecule blebbistatin (Figure 5.6a). For the details of the protocol, we refer the reader to chapter 3. We hypothesized that locally killing cells would create a free boundary around which the cells would increase surface stresses that would cause bending of the bulk tissue.

To demonstrate controlled bending and subsequent plastic deformation, we illuminated one side of stadium-shaped microtissues that were treated with blebbistatin. In the course of six hours after illumination, we observed irreversible bending of the microtissue towards the direction of the illuminated side (Figure 5.6b, Left). If the tissues were under tension prior to the manipulation, they would bend in the opposite direction due to local relaxation of stress. Notably, microtissues formed with MDCK cells showed a larger amount of bending compared to MDCKII cells, revealing the importance of the strength of surface stresses (Figure 5.6b (Right) and Figure 5.6c). Moreover, we found tissue bending to be correlated with the overall tissue compaction (Figure 5.6d).

Surface stresses may increase due to two distinct mechanisms, either the epithelium acts as an elastic band that is contracted upon illumination or the locally unjammed cells apply higher traction forces at the edge of the illuminated area. Experimental observations so far reinforced the second theory. Time-lapse microscopy has shown that the epithelium actively moved and extruded the dead cells over the course of 24 hours (Figure 5.6e). Similar to gap closure, extrusion of dead cells by neighboring cells relies on the interactions between actomyosin contraction and lamellipodia-driven cell crawling. To interrogate the role of cell migration, we performed experiments on cell monolayers cultured on a planar collagen substrate. We observed that, similar to the 3D scenario, the epithelium flowed into the exposed area and the dead cells were extruded from the substrate over the course of 24 hours. The 2D cell motion is essentially constrained to the

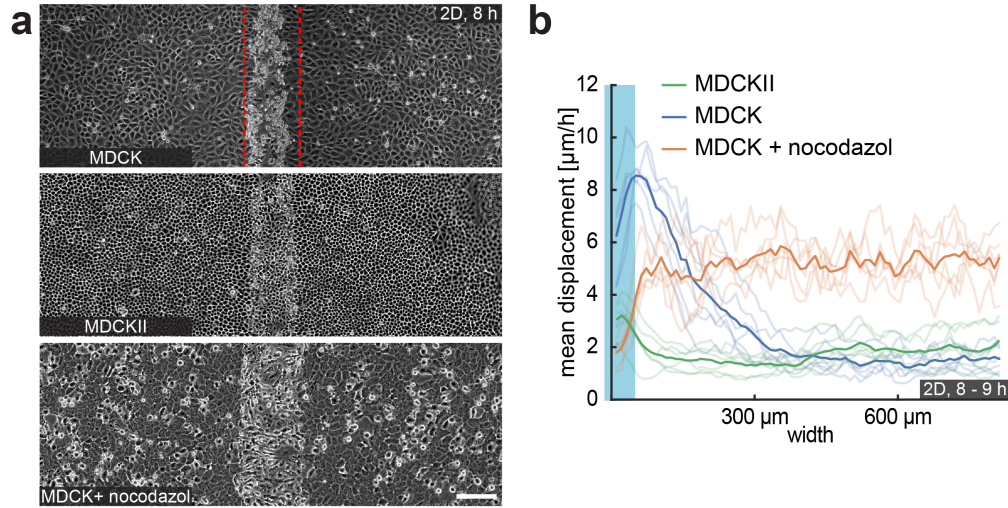


Figure 5.7: Cell extrusion in monolayers on flat collagen substrates. (a) A region of 200 μm in width is exposed to light. Representative images of cell extrusion 8 hours after illumination are shown for MDCK, MDCKII, and MDCK treated with nocodazol. MDCK treated with nocodazol fail to extrude dead cells. (b) Graph showing mean displacement of cells from 8 to 9 hours after illumination, measured with particle image velocimetry. Edge of illuminated region is indicated in blue. Transparent lines show single samples and the bold line their mean. MDCK (blue), MDCKII (green), and MDCK treated with nocodazol (red). (N=2, n=6). Scale bar, 200 μm

wound edge (Figure 5.7a and b). Nocodazol, a drug that depolymerizes microtubules, disrupts the integrity of the monolayer as displayed by the balling up of the cells (Figure 5.7a). Cells treated with nocodazol cannot move into the illuminated area and extrude the dead cells in the planar assay (Figure 5.7b). Notably, we recorded higher curvature on microtissues treated with nocodazol right after illumination (Figure 5.5c). Moreover, for untreated microtissues creases formed on both sides of the illuminated area 4 hours after illumination, indicating local compression of the collagen gel (Figure 5.8a). Finally, bending was amplified when the illumination was performed during tissue formation (Figure 5.8b). These observations have indicated that it is not the contraction of the epithelium shell but the traction forces applied at the wound edge elevating the surface stress.

To put the theory that surface stresses are generated by unjammed epithelia, where cells show mesenchymal characteristic and apply higher traction forces, we induced an epithelial-to-mesenchymal transition (EMT) by treating the microtissues with the transforming growth factor β_1 (Tgf- β_1)

[179]. Preliminary results have shown that the transition enhances tissue bending (Figure 5.8c).

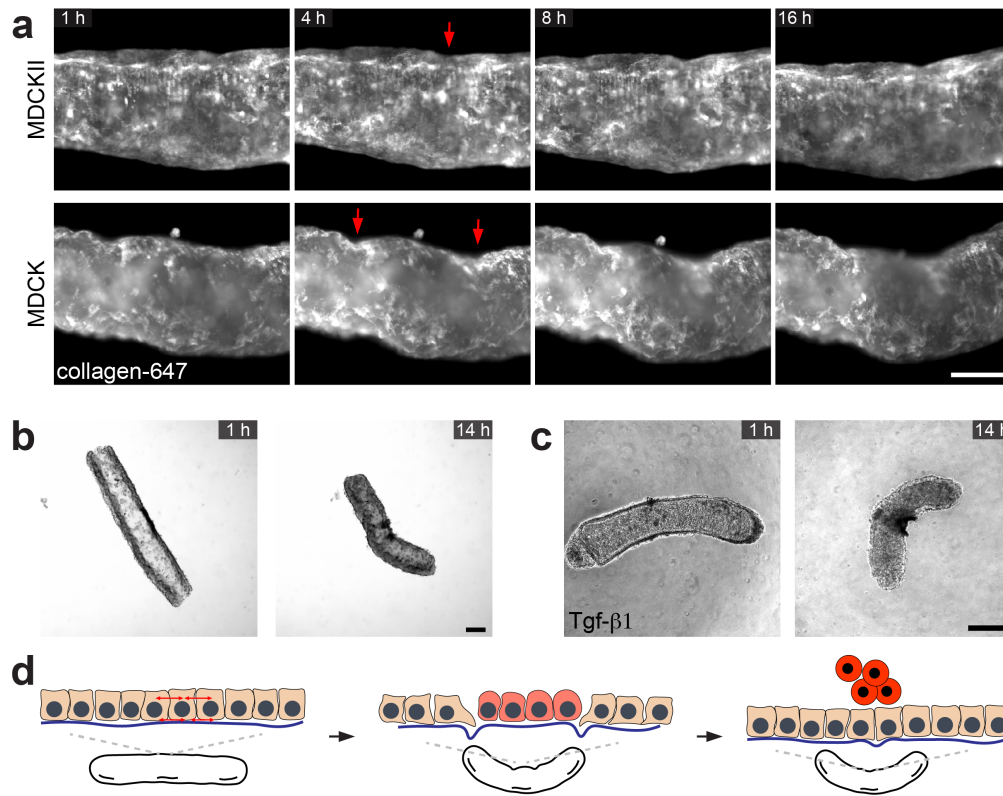


Figure 5.8: Traction forces at the wound edge lead to tissue folding. (a) Micrographs of fluorescently labelled collagen (collagen-647) recorded with light-sheet microscopy. Tissues are formed with MDCKII (Upper panel) or MDCK (Lower panel). Creases are visible at the edges of the illuminated region (red arrows). Scale bar, 100 μm . (b) Microtissue formed with MDCKII cells is exposed to light 30 minutes after collagen polymerisation. Scale bar, 200 μm . (c) Tissues formed with MDCKII and subsequently treated with Tgf- β 1 fold after local light exposure. Scale bar, 200 μm . (d) Postulated mechanism of microtissue folding. (i) Cell forces are balanced in unperturbed state. (ii) Dying cells do not apply forces on the underlying collagen and it locally expands. Surrounding cells apply traction forces to migrate and balance mismatch of forces. Traction forces lead to local anisotropic collagen compaction, visible by creases at the interface, leading to tissue folding. (iii) Together with the induction of folding cells migrate inwards and extrude dying cells.

5.3 Discussion

Epithelial sheets could act both as a solid to maintain physical boundaries and fluid to create new boundaries or regenerate lost parts [20, 34]. In our model, we harnessed these phase transitions to create a shape-programmable living matter. We observed that morphogenesis is different for

microtissues formed from MDCKII cells or 3T3 cells. Although both types of cells generate surface stresses during tissue formation, only the shell made of MDCKII cells eventually underwent a jamming transition. It has been shown that wetting transition in epithelium is controlled by the competition between traction forces and intercellular stresses [105]. Therefore, it is conceivable that MDCKII cells reduce traction forces while strengthening tight junctions and increasing tension within the monolayer during the first day of culture. *In situ* stress measurements are required to prove this theory. Notably, the microtissues expand during the next five days, which may be associated with changes in osmotic pressure or cell intercalations.

The scale at which surface stresses contribute to bulk morphogenesis in soft solids is defined by the elastocapillary length. This length is defined by the competition between surface forces and the bulk elastic stresses. Surface stresses (γ) dominate when the characteristic size of the sample is smaller than the shear elastocapillary length given by $l_s = \gamma/G$ where G is the shear modulus [152]. Therefore, the equilibrium morphology of the microtissue depends on the collagen concentration and the original mould size, where smaller and softer tissues are expected to deviate more from the prescribed shape. On the other extreme, it would be more challenging to shape large and stiff tissues using plastic forming or local cell killing due to the dominance of bulk stresses. Plastic forming involves the deformation of the tissues with mechanical loading in a way that the structure preserves its new shape after the removal of the external stress. Upon stretching or bending, the epithelial monolayer would locally fluidize, remodel, and eventually re-solidify. Preliminary results have demonstrated the feasibility of shaping tissues using this technique.

Microtissues autonomously bent upon local disruption of epithelial cohesion. We postulate that by locally killing cells we perturb the balance of forces and cells at the boundary apply traction forces as a result. These forces locally contract collagen, as visualized by the formation of creases, and subsequently fold the tissue (Figure 5.8e). Increase in traction forces at the boundary may not solely be due to unjamming but may require a transition from an epithelial to mesenchymal state. Using Tgf- β 1 we show preliminary evidence that EMT increases surface stresses and curvature in the course of shaping.

Here we presented a tissue engineering framework, to mold and further shape fibrous microtissues. Like pottery, the living material can be cast into molds, solidified over time and fur-

ther sculptured using additive and subtractive manufacturing techniques. The controllable microscale tissues composed of an elastic collagen core and an epithelial shell can potentially be used as building blocks for the assembly of complex organ-like *in vitro* constructs. We can also envision encapsulation of cells inside the collagen core, to introduce new functionality.

5.4 Materials and Methods

Device fabrication

Polydimethylsiloxane (PDMS, Sylgard 184; Dow-Corning, Midland, MI) substrates were molded from 3D printed stamps (Formlabs Form 2). The devices were then sterilized in 70% ethanol, followed by ultraviolet exposure for 15 min. Before cell seeding, the devices were treated with 0.02% Pluronic-F127 solution (Sigma-Aldrich, St. Louis, MO) for 20 min at room temperature.

Cell culture and reagents

MDCKII epithelial cells (ECACC, CAT#00062107), MDCK epithelial cells (ECACC, CAT#84121903), NIH-3T3 fibroblasts (ECACC, CAT#93061524), and MDCKII H2B-eGFP mCherry-Actin cells (kindly provided by Prof. Daniel Müller (D-BSSE, ETHZ, Basel, CH)) were cultured in Dulbecco's modified Eagle's medium GlutaMAX (Life Technologies, Carlsbad, CA) supplemented with 10% fetal bovine serum (Life Technologies) and 1% penicillin-streptomycin (Life Technologies). The cells were passaged every 2–3 days using PBS and trypsin 0.25% EDTA (Life Technologies). All experiments were done with cells not kept longer than 20 passages and that tested negative for mycoplasma. Blebbistatin (Sigma-Aldrich), cytochalasin-D (Sigma-Aldrich), and nocodazol (Sigma-Aldrich) were dissolved in dimethyl sulfoxide at 10 mM. Aphidicolin (Sigma-Aldrich) at 1 mg/ml. Drugs were supplemented to the medium at the start of experiment. Mitomycin-C (Sigma-Aldrich) was reconstituted in deionized water at 0.5 mg/ml. Microtissues were incubated for 2 hours in medium supplemented with Mitomycin-C but it was washed out before start of experiment. Tgf- β 1 (Peprotech, CAT#00062107100-21-2UG) was reconstructed following manufacturers protocol. Prior experiment microtissues were incubated in serum-free medium supplemented with 2 ng/ml Tgf- β 1 for 24 hours. For the experiment serum-free medium was

exchanged with medium supplemented with 2 ng/ml Tgf- β 1.

Microtissue model

For microtissue formation in 400 μ m deep wells, in total 2 million MDCKII cells, 1 million MDCK cells, or 1 million 3T3 cells were used. Half of the cells were suspended in 1 or 2 mg ml⁻¹ liquid neutralized collagen type I from rat tail (Corning BV Life Sciences) and seeded in the device. The entire assembly was centrifuged to drive cells onto the bottom of the chambers. Excess solution was then removed, leaving only the chambers filled with liquid. After 9 minutes polymerization at 37°C, the other half of cells was resuspended in 1 ml medium and added on top. For stabilisation of tissues formed with MDCK, 2% Matrigel (Corning BV Life Sciences) was supplemented to the medium. Within 2 hours after polymerization, we observed the spontaneous contraction of the collagen matrix by the cells. Over the course of 24 hours cells on top and on the bottom of the three-layer sandwich structure eventually fully surrounded the collagen core.

Microscopy

Phase-contrast, DIC and fluorescent images were captured every hour for 20h with an ORCA-Flash4.0 digital CMOS camera (Hamamatsu, Hamamatsu City, Japan) mounted on a Nikon Ti Eclipse (Nikon Instruments, Inc) microscope. The microscope is equipped with a Plan Fluor 10x objective and a live-cell incubator for long term imaging (Life Imaging Services, Switzerland). For F-actin imaging, microtissues were labeled with Alexa Fluor 488 Phalloidin (ThermoFisher, CAT#A12379). For fluorescent imaging and light-sheet microscopy microtissues were formed using MDCKII H2B-eGFP mCherry-Actin cells. Before tissue engineering, collagen type I from rat tail was labelled with Alexa Fluor 647 NHS ester (ThermoFisher, CAT#A20006). 5 μ l of 1 mg/ml Alexa Fluor 647 NHS ester was added to 450 μ l of 3.8 mg/ml Rat tail collagen and incubated for 2 hours at 4°C prior collagen neutralisation. For imaging, samples were mounted on a LSi Live light-sheet (Viventis) microscope equipped with two 25x objectives.

Quantitative image analysis

To quantify tissue morphology of the capsule-shaped microtissues, time-lapse images were first segmented using a semiautomated processing software in ImageJ. Shape parameters were extracted with a custom script written in MATLAB (Mathworks, MA). The script skeletonized the tissues, calculated tip points, and measured area, width, and length. To quantify shape the script fitted a circle to the median line and calculated the central angle. To quantify cell motion on two-dimensional substrates, particle image velocimetry was performed using PIVlab written for Matlab [180]. To not track discrete objects within the cells, images were treated with a fast Fourier transform bandpass filter 3-6 pixel wide. We used 64x64 pixel interrogation windows with 50% overlap. Cross-correlation was performed by using the fast Fourier transform method. For post-processing a velocity limit of around 25 pixel per frame was chosen and error-prone vectors were filtered out using the standard deviation filter. The data was processed with a custom script in Matlab. The script accepted the window locations (x,y) and corresponding vectors (u,v) of each frame and calculated mean velocities at a given location or from the entire frame, respectively. All data was plotted using custom scripts in Matlab and Python.

Chapter 6

Conclusion and Future Work

6.1 Conclusion

Embryonic development starts at the microscale with a small number of cells where morphogenic episodes are rich and abundant. The scale and material properties provide a structure where the distribution and activity of cells can critically influence the global tissue morphology. Recent work has highlighted the contribution of the provisional extracellular matrix (ECM) to the shaping process. 3D bioengineered *in vitro* models are ideal to systematically study the mechanics of tissue morphogenesis. They enable quantitative 3D time-lapse imaging, precise control over material composition, and spatiotemporally resolved mechanical manipulations. Together, this provides the basis for physics-based computational models [181]. The work presented in this thesis establishes a new set of technological, and computational tools that contribute to a better understanding of living systems.

Tissue morphogenesis is studied with either suspended culture models that are accessible from outside or cell clusters embedded inside hydrogels, depending on the type of tissue. Here, we focused our attention on problems that fall into the first category. We asked the following fundamental question: "What kind of shape transformation do we expect to see if we encapsulate cells inside a microscale collagen gel?". The cells (fibroblasts or epithelial cells) reside on the surface of the gel or inside the gel, and the tissue may be completely untethered or constrained with anchors.

We worked solely with reconstituted collagen I matrix as this material recapitulates morphogenesis associated with fiber remodeling. The primary objective was to determine the dominant forces acting on the tissue as well as the structural changes taking place inside and around the gel. This required the use of precise manipulation techniques. To this end, we introduced a robotic manipulation system as well as a photochemical stimulation protocol. Finally, we sought to control the forces that act on the tissue in order to guide the morphogenesis process.

A number of reported morphogenic events indicated that surface stress is a dominant force. We designed a series of experiments to prove that the cells residing on the surface are indeed generating stresses. Moreover, we developed a computational model based on an equilibrium theory that combines bulk and surface potential energy. The simulation results captured empirical morphological changes by only fitting two parameters, bulk and surface contractile moduli η and γ . These results further strengthened the theory that surface stresses play a major role in our model system.

Based on these results, we postulated that engineering fibrous microtissues with prescribed shapes could be achieved using surface stresses. Compared to controlling bulk stresses, surface stresses may be turned off due to a jamming transition. There is an increasing amount of literature on solid to fluid transitions in epithelia, with observations both *in vivo* and *in vitro*. Encouraged by these reports, we decided to pattern an epithelial shell around a collagen core and thereby engineer the respective tissue. With precise mechanical manipulations through cutting, piercing, loading or photochemically induced cell death, we initiated local fluidization of the shell and established engineering control over the shape of microtissues.

The overall experimental platform built upon microengineering, robotics, and biochemistry along with the computational modeling framework based on continuum mechanics enabled the discovery of fundamental principles in tissue mechanics and mechanobiology. The incorporation of the fibrous elements is particularly important and complements previous work on cell clusters. Analogous to the major influence of surface tension on the shape of cell clusters, we discovered that surface stresses arise in fibrous tissues due to traction forces. The theory of elastocapillarity predicts the length scale at which these stresses are significant. There is still much work to be done to reveal the full spectrum of options in terms of engineering tissues with desired archi-

ture. The next section summarizes the directions along which such investigations could be carried forward.

6.2 Future Work on Biomanipulation

3D bioengineered *in vitro* models such as organoids and organ-on-a-chip devices have the potential to partially replace animal trials. Pharmaceutical companies have already started to transform their testing platforms. Once the culture conditions are established, automated handling as well as continuous interrogation and conditioning of 3D culture systems will require robotic micromanipulation in near future. Our work is a step forward in this direction. Considering the complexity of the manipulation tasks and the variability in the characteristics of the samples, we proposed a technique where the robot learns from the expert. This framework can be extended to scenarios where the sample is not suspended but embedded in a gel. Minimally-invasive navigation is a must to not perturb the culture conditions, therefore the tools must be tiny. At such small scale, even metal structures bend, as studied extensively in needle steering problems [182]. A novel modeling and control strategy must be developed based on the elastic properties of the tool and the rheology of the gels. Furthermore, novel tools must be developed that are relatively long, ultraflexible, and functional. This could be achieved using 3D nanoprinting, which has advanced significantly during the last decade, enabling printing of polymers (Nanoscribe) or glass (Femtoprint). Initial trials have shown that imaging during 3D manipulation is going to be another challenge. Novel imaging modalities are required based on light-sheet microscopy that may provide the required speed and resolution for closed-loop visual servoing.

An interesting direction for biomanipulation is the concept of robot scientists. Robots have been used recently to synthesize novel compounds by harnessing techniques from machine learning. Seminal work has demonstrated that a robot can formulate hypotheses on functional genomics and perform experiments to test them [183]. Overall, there is a growing number of intelligent systems at the intersection of robotics and fluidics that perform drug screening and related biochemistry experiments [184]. A robotic manipulation system that can repeatedly and precisely manipulate 3D culture systems may adjust the parameters of manipulation based on the information acquired from the biological sample. This information may be a microscope image indicating

changes in morphology, expression levels of certain proteins, or quantification of biochemicals that are collected by robotic tools. Either way, the algorithms may determine the optimal perturbation that would drive the morphogenesis in the right way or discover novel ways of treatment.

Spatially patterned phototoxic treatment enabled local removal of stress from tissues in order to evaluate the contribution of different mechanical forces. Living tissues have the ability to extrude dead cells and regenerate. Based on this biological self-healing mechanism, we proposed controlled apoptosis as a novel technique for tissue morphogenesis. The biochemical changes that take place upon phototoxic conversion of blebbistatin is not fully understood. Generation of reactive oxygen species is the prevailing theory [130, 131]. Before this technique can be widely used, a detailed investigation of the cell state is required. In this work a digital projector was used for light exposure. For higher spatial resolution, specifically in the z axis, a two-photon laser can be used.

Optochemical and optogenetic systems enable the use of light to manipulate intracellular signaling within tissues [185]. Whereas optogenetics has tremendous potential in precisely manipulating protein activity, de novo design relies (i) on predictive DNA translation into proteins with defined enzymatic sides, or discovery and adaption from nature, and (ii) genetic integration on tissue scale. As of today, we have limited predictions to modify the enzymatic side on the gene level. On the other hand, more work has been done on the modification of functional molecular groups. A common strategy is to covalently modify a functional side with a photocleavable moiety. Not only molecular cleavage, but also light-driven cis/ trans isomerization of an attached azobenzene moiety has been optimized for the control of nucleic acid and protein activity [186]. Both, optochemical and optogenetic manipulation techniques have been very recently introduced to the field of mechanobiology. We tried to use some of these constructs but the signal to noise ratio was too low. With combined efforts from photochemistry and biology it is to be expected that more versatile and robust constructs will be introduced, of which some will be useful for tissue morphogenesis.

6.3 Future Work on Mechanobiology

We postulated that surface stresses arise in constrained fibrous tissues due the dynamic interaction between fibroblasts and the fibronectin matrix. Through computational modeling we discovered that the traction forces were higher than values reported for cells cultured on planar substrates. We speculated that this discrepancy could be due to the fiber recruitment, nonlinear stiffening, and plasticity of collagen. A recent work supported the idea that the ECM contributes to surface stresses [103]. Notably, bacteria biofilms that are composed of cells embedded in a dynamically cross-linked polymer matrix apply high surface stresses. Similar to the case of biofilms, high surface stresses may emerge when cells are connected via a fibrillar matrix and progressively remodel the fibers. While we predicted a value for surface stresses through computational modeling, experimental quantification of strain-dependent surface stresses is challenging even in non-living solids [187]. Novel techniques are required for making direct measurements.

Formation of an ECM rich outer tissue layer may have another important implication. When we trypsinized constrained microtissues composed of fibroblasts and collagen, the tissue shape did not change much because the collagen gel is remodeled by the resident cells [167]. Surprisingly, the shape of the tissue remained the same when we trypsinized unconstrained microtissues composed of epithelial cells and collagen. One theory that is to be tested is that epithelial cells remodel the underlying matrix using fibronectin and other proteins floating in the medium. Indeed, there is evidence in the literature which supports this argument. For example, it has been shown that a self-assembled polarized fibrillar extracellular matrix at the tissue periphery defined shape during egg elongation in fruit flies [85]. Moreover, mouse embryo becomes enveloped by a basement membrane during development [188]. Treatment of microtissues composed of fibroblasts and collagen with a peptide that inhibits cell-fibronectin binding led to a significant relaxation with increase in tissue width and decrease in boundary curvature. The same compound has to be tested on microtissues composed of epithelial cells and collagen, to dissociate the shell along with a potentially interwoven provisional matrix.

6.4 Future Work on Engineered Morphogenesis

We focused our work on collagen and immortalized cell lines to be able to build upon previous work and keep the biological responses relatively simple. As a downside of this approach, the engineered tissues are not functional. The functionality may be instantiated by increasing the complexity of the architecture. To this end, we have been exploring different ways of dynamically modulating the properties of the ECM. One extreme manipulation is enzymatically dissociating the collagen core using collagenase. This modification may lead to the formation of ducts [189]. Our preliminary results showed that collagen can be successfully removed from the tissue. However, we observed serious stability problems as the thin epithelial shell collapses. There are many future directions in this domain, including the use of synthetic hydrogels and controlling the activity of the enzyme. Embedding cells inside the collagen core is another way of introducing physiological functionality. The mechanical effects of having cells in the bulk will depend on the type of the chosen cell and the design framework must be updated accordingly.

Biological machines emerged as a novel application for tissue engineering [190, 191]. They serve two distinct purposes at the moment; (i) to explore the design and operation principles of biological systems by building biomimetic machinery from living matter and (ii) to introduce novel functionality such as intelligence and self-healing to the engineering domain. Existing biological machines are biohybrid constructs and they rely on synthetic structures such as elastomers for stabilizing their shape. Our shaping techniques have the potential to build machines using morphogenic principles and only from biomaterials. Without synthetic structures, the whole machine can be edible, biodegradable, and self-healing. Moreover, they may be programmed to reconfigure their shape upon external mechanical or chemical stimulation.

Bibliography

- [1] T. Mammoto and D. E. Ingber. Mechanical control of tissue and organ development. *Development*, 137(9):1407–1420, 2010. 7, 43, 71
- [2] D. E. Ingber. Mechanical control of tissue morphogenesis during embryological development. *International Journal of Developmental Biology*, 50(2-3):255–266, 2006. 7, 15
- [3] D. Gilmour, M. Rembold, and M. Leptin. From morphogen to morphogenesis and back. *Nature*, 541(7637):311–320, 2017. 7, 11, 71
- [4] T. D. Pollard and G. G. Borisy. Cellular Motility Driven by Assembly and Disassembly of Actin Filaments. *Cell*, 112(4):453–465, 2003. 8
- [5] M. Vicente-Manzanares, X. Ma, R. S. Adelstein, and A. R. Horwitz. Non-muscle myosin II takes centre stage in cell adhesion and migration. *Nature Reviews Molecular Cell Biology*, 10(11):778–790, 2009. 8
- [6] D. A. Fletcher and R. D. Mullins. Cell mechanics and the cytoskeleton. *Nature*, 463(7280):485–92, 2010. 8
- [7] W. Xi, T. B. Saw, D. Delacour, C. T. Lim, and B. Ladoux. Material approaches to active tissue mechanics. *Nature Reviews Materials*, 4(1):23–44, 2019. 8
- [8] M. L. Manning, R. A. Foty, M. S. Steinberg, and E.-M. Schoetz. Coaction of intercellular adhesion and cortical tension specifies tissue surface tension. *Proceedings of the National Academy of Sciences*, 107(28):12517–12522, 2010. 8, 17, 43, 62
- [9] J. T. Parsons, A. R. Horwitz, and M. A. Schwartz. Cell adhesion: Integrating cytoskeletal

- dynamics and cellular tension. *Nature Reviews Molecular Cell Biology*, 11(9):633–643, 2010. 8
- [10] D. E. Discher, P. Janmey, and Y. Wang. Tissue cells feel and respond to the stiffness of their substrate. *Science*, 310(5751):1139–43, 2005. 9
- [11] V. Vogel and M. Sheetz. Local force and geometry sensing regulate cell functions. *Nature Reviews Molecular Cell Biology*, 7(4):265–75, 2006. 9
- [12] T. Iskratsch, H. Wolfenson, and M. P. Sheetz. Appreciating force and shape — The rise of mechanotransduction in cell biology. *Nature Reviews Molecular Cell Biology*, 15(12):825–833, 2014. 9
- [13] J. Yang, P. Antin, G. Berx, C. Blanpain, T. Brabletz, M. Bronner, K. Campbell, A. Cano, J. Casanova, G. Christofori, S. Dedhar, R. Derynck, H. L. Ford, J. Fuxe, A. García de Herreros, G. J. Goodall, A. K. Hadjantonakis, R. J. Huang, C. Kalcheim, R. Kalluri, Y. Kang, Y. Khew-Goodall, H. Levine, J. Liu, G. D. Longmore, S. A. Mani, J. Massagué, R. Mayor, D. McClay, K. E. Mostov, D. F. Newgreen, M. A. Nieto, A. Puisieux, R. Runyan, P. Savagner, B. Stanger, M. P. Stemmler, Y. Takahashi, M. Takeichi, E. Thevenneau, J. P. Thiery, E. W. Thompson, R. A. Weinberg, E. D. Williams, J. Xing, B. P. Zhou, and G. Sheng. Guidelines and definitions for research on epithelial–mesenchymal transition. *Nature Reviews Molecular Cell Biology*, 21(6):341–352, 2020. 9
- [14] B. K. Hall and T. Miyake. Divide, accumulate, differentiate: Cell condensation in skeletal development revisited. *International Journal of Developmental Biology*, 39(6):881–893, 1995. 9
- [15] P. Friedl and D. Gilmour. Collective cell migration in morphogenesis, regeneration and cancer. *Nature Reviews Molecular Cell Biology*, 10(7):445–457, 2009. 11
- [16] S. R. K. Vedula, H. Hirata, H. M. Nai, A. Brugués, Y. Toyama, X. Trepats, C. Lim, and B. Ladoux. Epithelial bridges maintain tissue integrity during collective cell migration. *Nature Materials*, 13(1):87–96, 2014. 11, 12
- [17] A. Ravasio, I. Cheddadi, T. Chen, T. Pereira, H. T. Ong, C. Bertocchi, A. Brugués, A.

- Jacinto, A. J. Kabla, Y. Toyama, X. Trepát, N. Gov, L. Neves de Almeida, and B. Ladoux. Gap geometry dictates epithelial closure efficiency. *Nature Communications*, 6:7683, 2015. II, 12
- [18] C. C. Liang, A. Y. Park, and J. L. Guan. In vitro scratch assay: A convenient and inexpensive method for analysis of cell migration in vitro. *Nature Protocols*, 2(2):329–333, 2007. II
- [19] A. Brugués, E. Anon, V. Conte, J. H. Veldhuis, M. Gupta, J. Colombelli, J. J. Muñoz, G. W. Brodland, B. Ladoux, and X. Trepát. Forces driving epithelial wound healing. *Nature Physics*, 10(9):683–690, 2014. II, 12, 43, 77
- [20] A. R. Harris, L. Peter, J. Bellis, B. Baum, A. J. Kabla, and G. T. Charras. Characterizing the mechanics of cultured cell monolayers. *Proceedings of the National Academy of Sciences*, 109(41):16449–16454, 2012. II, 83
- [21] R. W. Style, R. Boltyanskiy, G. K. German, C. Hyland, C. W. Macminn, A. F. Mertz, L. A. Wilen, Y. Xu, and E. R. Dufresne. Traction force microscopy in physics and biology. *Soft Matter*, 10(23):4047–4055, 2014. II
- [22] X. Trepát, M. R. Wasserman, T. E. Angelini, E. Millet, D. A. Weitz, J. P. Butler, and J. J. Fredberg. Physical forces during collective cell migration. *Nature Physics*, 5(6):426–430, 2009. II
- [23] V. Maruthamuthu, B. Sabass, U. S. Schwarz, and M. L. Gardel. Cell-ECM traction force modulates endogenous tension at cell-cell contacts. *Proceedings of the National Academy of Sciences*, 108(12):4708–4713, 2011. II
- [24] A. F. Mertz, Y. Che, S. Banerjee, J. M. Goldstein, K. A. Rosowski, S. F. Revilla, C. M. Niessen, M. C. Marchetti, E. R. Dufresne, and V. Horsley. Cadherin-based intercellular adhesions organize epithelial cell-matrix traction forces. *Proceedings of the National Academy of Sciences*, 110(3):842–847, 2013. II
- [25] T. E. Angelini, E. Hannezo, X. Trepát, M. Marquez, J. J. Fredberg, and D. A. Weitz. Glass-

- like dynamics of collective cell migration. *Proceedings of the National Academy of Sciences*, 108(12):4714–4719, 2011. II, 12, 18, 71
- [26] M. Abercrombie, M. Flint, and D. James. Wound contraction in relation to collagen formation in scorbutic guinea-pigs. *Development*, 4(2):167–175, 1956. II, 43
- [27] G. T. Watts. Wound shape and tissue tension in healing. *British Journal of Surgery*, 47(205):555–561, 1960. II, 43
- [28] P. Martin and J. Lewis. Actin cables and epidermal movement in embryonic wound healing. *Nature*, 360(6400):179–183, 1992. II, 77
- [29] P. Martin. Wound healing—aiming for perfect skin regeneration. *Science*, 276(5309):75–81, 1997. II, 43
- [30] W. M. Bement, P. Forscher, and M. S. Mooseker. A novel cytoskeletal structure involved in purse string wound closure and cell polarity maintenance. *Journal of Cell Biology*, 121(3):565–578, 1993. 12
- [31] V. Ajeti, A. P. Tabatabai, A. J. Fleszar, M. F. Staddon, D. S. Seara, C. Suarez, M. S. Yousafzai, D. Bi, D. R. Kovar, S. Banerjee, and M. P. Murrell. Wound healing coordinates actin architectures to regulate mechanical work. *Nature Physics*, 15(7):696–705, 2019. 12
- [32] S. Karsch, D. Kong, J. Großhans, and A. Janshoff. Single-cell defects cause a long-range mechanical response in a confluent epithelial cell layer. *Biophysical Journal*, 113(12):2601–2608, 2017. 12
- [33] L. Kocgozlu, T. B. Saw, A. P. Le, I. Yow, M. Shagirov, E. Wong, R. M. Mège, C. T. Lim, Y. Toyama, and B. Ladoux. Epithelial cell packing induces distinct modes of cell extrusions. *Current Biology*, 26(21):2942–2950, 2016. 12
- [34] R. J. Tetley, M. F. Staddon, D. Heller, A. Hoppe, S. Banerjee, and Y. Mao. Tissue fluidity promotes epithelial wound healing. *Nature Physics*, 15(11):1195–1203, 2019. 12, 77, 83
- [35] A. Shellard and R. Mayor. Supracellular migration - Beyond collective cell migration. *Journal of Cell Science*, 132:jcs226142, 2019. 12

- [36] N. Gjorevski, N. Sachs, A. Manfrin, S. Giger, M. E. Bragina, P. Ordóñez-Morán, H. Clevers, and M. P. Lutolf. Designer matrices for intestinal stem cell and organoid culture. *Nature*, 539(7630):560–564, 2016. 12, 23
- [37] M. Nikolaev, O. Mitrofanova, N. Broguiere, S. Geraldo, D. Dutta, Y. Tabata, B. Elci, N. Brandenberg, I. Kolotuev, N. Gjorevski, H. Clevers, and M. P. Lutolf. Homeostatic mini-intestines through scaffold-guided organoid morphogenesis. *Nature*, 585(7826):574–578, 2020. 12, 23
- [38] A. J. Hughes, H. Miyazaki, M. C. Coyle, J. Zhang, M. T. Laurie, D. Chu, Z. Vavrušová, R. A. Schneider, O. D. Klein, and Z. J. Gartner. Engineered Tissue Folding by Mechanical Compaction of the Mesenchyme. *Developmental Cell*, 44(2):165–178.e6, 2018. 12, 14, 71
- [39] F. Grinnell. Fibroblasts, myofibroblasts, and wound contraction. *The Journal of Cell Biology*, 124(4):401–404, 1994. 12, 43
- [40] S. Ihara and Y. Motobayashi. Wound closure in foetal rat skin. *Development*, 114(3):573–82, 1992. 12
- [41] A. E. Shyer, A. R. Rodrigues, G. G. Schroeder, E. Kassianidou, S. Kumar, and R. M. Harland. Emergent cellular self-organization and mechanosensation initiate follicle pattern in the avian skin. *Science*, 357(6353):811–815, 2017. 12, 71
- [42] T. Mammoto, A. Mammoto, Y. Torisawa, T. Tat, A. Gibbs, R. Derda, R. Mannix, M. de Bruijn, C. W. Yung, D. Huh, and D. E. Ingber. Mechanochemical control of mesenchymal condensation and embryonic tooth organ formation. *Developmental Cell*, 21(4):758–769, 2011. 13
- [43] K. D. Walton, M. Whidden, A. Kolterud, S. K. Shoffner, M. J. Czerwinski, J. Kushwaha, N. Parmar, D. Chandrasekhar, A. M. Freddo, S. Schnell, and D. L. Gumucio. Villification in the mouse: Bmp signals control intestinal villus patterning. *Development*, 143(3):427–436, 2016. 13
- [44] A. E. Shyer, T. Tallinen, N. L. Nerurkar, Z. Wei, E. S. Gil, D. L. Kaplan, C. J. Tabin, and L. Mahadevan. Villification: How the gut gets its villi. *Science*, 342(6155):212–218, 2013. 13

-
- [45] M. A. Carlson and M. T. Longaker. The fibroblast-populated collagen matrix as a model of wound healing: a review of the evidence. *Wound Repair and Regeneration*, 12(2):134–147, 2004. 13, 43
 - [46] F. Grinnell and W. M. Petroll. Cell motility and mechanics in three-dimensional collagen matrices. *Annual Review of Cell and Developmental Biology*, 26:335–361, 2010. 13, 43
 - [47] J. Foolen, T. Yamashita, and P. Kollmannsberger. Shaping tissues by balancing active forces and geometric constraints. *Journal of Physics D: Applied Physics*, 49:053001, 2015. 13, 43
 - [48] J. Eyckmans and C. S. Chen. 3d culture models of tissues under tension. *Journal of Cell Science*, 130(1):63–70, 2017. 13, 43
 - [49] T. Elsdale and J. Bard. Collagen substrata for studies on cell behavior. *The Journal of Cell Biology*, 54(3):626–637, 1972. 13, 43
 - [50] E. Bell, B. Ivarsson, and C. Merrill. Production of a tissue-like structure by contraction of collagen lattices by human fibroblasts of different proliferative potential in vitro. *Proceedings of the National Academy of Sciences*, 76(3):1274–1278, 1979. 13, 43
 - [51] A. K. Harris, D. Stopak, and P. Wild. Fibroblast traction as a mechanism for collagen morphogenesis. *Nature*, 290(5803):249–251, 1981. 13, 43
 - [52] E. Ban, J. M. Franklin, S. Nam, L. R. Smith, H. Wang, R. G. Wells, O. Chaudhuri, J. T. Liphardt, and V. B. Shenoy. Mechanisms of plastic deformation in collagen networks induced by cellular forces. *Biophysical Journal*, 114(2):450–461, 2018. 13, 65
 - [53] W. R. Legant, A. Pathak, M. T. Yang, V. S. Deshpande, R. M. McMeeking, and C. S. Chen. Microfabricated tissue gauges to measure and manipulate forces from 3d microtissues. *Proceedings of the National Academy of Sciences*, 106(25):10097–10102, 2009. 13, 52, 53, 66
 - [54] H. Wang, A. S. Abhilash, C. S. Chen, R. G. Wells, and V. B. Shenoy. Long-range force transmission in fibrous matrices enabled by tension-driven alignment of fibers. *Biophysical Journal*, 107(11):2592–2603, 2015. 13
 - [55] D. Simon, C. Horgan, and J. Humphrey. Mechanical restrictions on biological responses

- by adherent cells within collagen gels. *Journal of the Mechanical Behavior of Biomedical Materials*, 14:216–226, 2012. 13, 64
- [56] D. Stopak and A. K. Harris. Connective tissue morphogenesis by fibroblast traction: I. tissue culture observations. *Developmental Biology*, 90(2):383–398, 1982. 13, 43
- [57] J. Foolen, V. S. Deshpande, F. M. W. Kanters, and F. P. T. Baaijens. The influence of matrix integrity on stress-fiber remodeling in 3D. *Biomaterials*, 33(30):7508–7518, 2012. 13
- [58] C. D. Morley, S. T. Ellison, T. Bhattacharjee, C. S. O’Bryan, Y. Zhang, K. F. Smith, C. P. Kabb, M. Sebastian, G. L. Moore, K. D. Schulze, S. Niemi, W. G. Sawyer, D. D. Tran, D. A. Mitchell, B. S. Sumerlin, C. T. Flores, and T. E. Angelini. Quantitative characterization of 3D bioprinted structural elements under cell generated forces. *Nature Communications*, 10:3029, 2019. 13
- [59] Z. Gartner and A. Hughes. Bioprinting in space and time. *Nature*, 572(7767):38–39, 2019. 13
- [60] J. M. Viola, C. M. Porter, A. Gupta, M. Alibekova, L. S. Prah, and A. J. Hughes. Guiding cell network assembly using shape-morphing hydrogels. *Advanced Materials*, 32(31):2002195, 2020. 14
- [61] A. T. Plygawko, S. Kan, and K. Campbell. Epithelial-mesenchymal plasticity: Emerging parallels between tissue morphogenesis and cancer metastasis. *Philosophical transactions of the Royal Society of London. Series B, Biological sciences*, 375(1809):20200087, 2020. 14
- [62] M. A. Futterman, A. J. García, and E. A. Zamir. Evidence for partial epithelial-to-mesenchymal transition (pEMT) and recruitment of motile blastoderm edge cells during avian epiboly. *Developmental Dynamics*, 240(6):1502–1511, 2011. 14
- [63] P. L. Leopold, J. Vincent, and H. Wang. A comparison of epithelial-to-mesenchymal transition and re-epithelialization. *Seminars in Cancer Biology*, 22(5-6):471–483, 2012. 14
- [64] M. T. Grande, B. Sánchez-Laorden, C. López-Blau, C. A. De Frutos, A. Boutet, M. Arévalo, R. G. Rowe, S. J. Weiss, J. M. López-Novoa, and M. A. Nieto. Snail-induced

- partial epithelial-to-mesenchymal transition drives renal fibrosis in mice and can be targeted to reverse established disease. *Nature Medicine*, 21(9):989–997, 2015. 14
- [65] E. Beerling, D. Seinstra, E. de Wit, L. Kester, D. van der Velden, C. Maynard, R. Schäfer, P. van Diest, E. Voest, A. van Oudenaarden, N. Vrisekoop, and J. van Rheenen. Plasticity between epithelial and mesenchymal states unlinks EMT from metastasis-enhancing stem cell capacity. *Cell Reports*, 14(10):2281–2288, 2016. 14
- [66] E. Theveneau and R. Mayor. Collective cell migration of epithelial and mesenchymal cells. *Cellular and Molecular Life Sciences*, 70(19):3481–3492, 2013. 14
- [67] A. K. Lawton, A. Nandi, M. J. Stulberg, N. Dray, M. W. Sneddon, W. Pontius, T. Emonet, and S. A. Holley. Regulated tissue fluidity steers zebrafish body elongation. *Development*, 140(3):573–582, 2013. 15
- [68] F. Serwane, A. Mongera, P. Rowghanian, D. A. Kealhofer, A. A. Lucio, Z. M. Hockenberg, and O. Campàs. In vivo quantification of spatially varying mechanical properties in developing tissues. *Nature Methods*, 14(2):181–186, 2016. 15
- [69] A. Mongera, P. Rowghanian, H. J. Gustafson, E. Shelton, D. A. Kealhofer, E. K. Carn, F. Serwane, A. A. Lucio, J. Giammona, and O. Campàs. A fluid-to-solid jamming transition underlies vertebrate body axis elongation. *Nature*, 561(7723):401–405, 2018. 15, 71
- [70] X. Wang, M. Merkel, L. B. Sutter, G. Erdemci-Tandogan, M. L. Manning, and K. E. Kasza. Anisotropy links cell shapes to tissue flow during convergent extension. *Proceedings of the National Academy of Sciences*, 117(24):13541–13551, 2020. 15
- [71] S. W. Moore, R. E. Keller, and M. A. Koehl. The dorsal involuting marginal zone stiffens anisotropically during its convergent extension in the gastrula of *Xenopus laevis*. *Development*, 121(10):3131–3140, 1995. 15
- [72] H. Ninomiya and R. Winklbauer. Epithelial coating controls mesenchymal shape change through tissue-positioning effects and reduction of surface-minimizing tension. *Nature Cell Biology*, 10(1):61–69, 2008. 15
- [73] N. I. Petridou, S. Grigolon, G. Salbreux, E. Hannezo, and C. P. Heisenberg. Fluidization-

- mediated tissue spreading by mitotic cell rounding and non-canonical Wnt signalling. *Nature Cell Biology*, 21(2):169–178, 2019. 15
- [74] H. Morita, S. Grigolon, M. Bock, S. G. Krens, G. Salbreux, and C.-P. Heisenberg. The physical basis of coordinated tissue spreading in zebrafish gastrulation. *Developmental Cell*, 40(4):354–366, 2017. 15, 43, 62
- [75] B. Wallmeyer, S. Trinschek, S. Yigit, U. Thiele, and T. Betz. Collective cell migration in embryogenesis follows the laws of wetting. *Biophysical Journal*, 114(1):213–222, 2018. 15, 62
- [76] E. A. Zamir, B. J. Rongish, and C. D. Little. The ECM moves during primitive streak formation - Computation of ECM versus cellular motion. *PLoS Biology*, 6(10):e247, 2008. 15
- [77] R. Loganathan, B. J. Rongish, C. M. Smith, M. B. Filla, A. Czirok, B. Bénazéraf, and C. D. Little. Extracellular matrix motion and early morphogenesis. *Development*, 143(12):2056–2065, 2016. 15
- [78] D. A. Walma and K. M. Yamada. The extracellular matrix in development. *Development*, 147(10):dev175596, 2020. 15
- [79] L. A. Davidson, R. Keller, and D. W. DeSimone. Assembly and remodeling of the fibrillar fibronectin extracellular matrix during gastrulation and neurulation in *Xenopus laevis*. *Developmental Dynamics*, 231(4):888–895, 2004. 15
- [80] P. Skoglund and R. Keller. *Xenopus* fibrillin regulates directed convergence and extension. *Developmental Biology*, 301(2):404–416, 2007. 15
- [81] D. R. Shook, E. M. Kasprowicz, L. A. Davidson, and R. Keller. Large, long range tensile forces drive convergence during *Xenopus* blastopore closure and body axis elongation. *eLife*, 7:e26944, 2018. 15
- [82] N. Dray, A. Lawton, A. Nandi, D. Jülich, T. Emonet, and S. A. Holley. Cell-fibronectin interactions propel vertebrate trunk elongation via tissue mechanics. *Current Biology*, 23(14):1335–1341, 2013. 15

- [83] A. S. Dias, I. De Almeida, J. M. Belmonte, J. A. Glazier, and C. D. Stern. Somites without a clock. *Science*, 343(6172):791–795, 2014. 15
- [84] L. Truskinovsky, G. Vitale, and T. H. Smit. A mechanical perspective on vertebral segmentation. *International Journal of Engineering Science*, 83:124–137, 2014. 15
- [85] S. L. Haigo and D. Bilder. Global tissue revolutions in a morphogenetic movement controlling elongation. *Science*, 331(6020):1071–1074, 2011. 15, 93
- [86] S. Münster, A. Jain, A. Mietke, A. Pavlopoulos, S. W. Grill, and P. Tomancak. Attachment of the blastoderm to the vitelline envelope affects gastrulation of insects. *Nature*, 568(7752):395–399, 2019. 15
- [87] A. Bailles, C. Collinet, J. M. Philippe, P. F. Lenne, E. Munro, and T. Lecuit. Genetic induction and mechanochemical propagation of a morphogenetic wave. *Nature*, 572(7770):467–473, 2019. 15
- [88] E. Heller, K. V. Kumar, S. W. Grill, and E. Fuchs. Forces generated by cell intercalation tow epidermal sheets in mammalian tissue morphogenesis. *Developmental Cell*, 28(6):617–632, 2014. 15
- [89] M. Linde-Medina and R. Marcucio. Living tissues are more than cell clusters: The extracellular matrix as a driving force in morphogenesis. *Progress in Biophysics and Molecular Biology*, 137:46–51, 2018. 15
- [90] H. M. Phillips and M. S. Steinberg. Embryonic tissues as elasticoviscous liquids. I. Rapid and slow shape changes in centrifuged cell aggregates. *Journal of Cell Science*, 30:1–20, 1978. 16, 17
- [91] O. Chaudhuri, J. Cooper-White, P. A. Janmey, D. J. Mooney, and V. B. Shenoy. Effects of extracellular matrix viscoelasticity on cellular behaviour. *Nature*, 584(7822):535–546, 2020. 16
- [92] D. Gonzalez-Rodriguez, K. Guevorkian, S. Douezan, and F. Brochard-Wyart. Soft matter models of developing tissues and tumors. *Science*, 338(6109):910–917, 2012. 16
- [93] R. David, O. Luu, E. W. Damm, J. W. H. Wen, M. Nagel, and R. Winklbauer. Tissue

- cohesion and the mechanics of cell rearrangement. *Development*, 141(19):3672–3682, 2014. 16
- [94] T. V. Stirbat, A. Mgharbel, S. Bodennec, K. Ferri, H. C. Mertani, J. P. Rieu, and H. Delanoë-Ayari. Fine Tuning of Tissues’ Viscosity and Surface Tension through Contractility Suggests a New Role for α -Catenin. *PLoS One*, 8(2):e52554, 2013. 16
- [95] B. G. Godard and C. P. Heisenberg. Cell division and tissue mechanics. *Current Opinion in Cell Biology*, 60:114–120, 2019. 16
- [96] P. Kollmannsberger, C. T. Mierke, and B. Fabry. Nonlinear viscoelasticity of adherent cells is controlled by cytoskeletal tension. *Soft Matter*, 7(7):3127–3132, 2011. 16
- [97] C. Storm, J. J. Pastore, F. C. MacKintosh, T. C. Lubensky, and P. A. Janmey. Nonlinear elasticity in biological gels. *Nature*, 435(7039):191–194, 2005. 16, 43
- [98] I. B. Bischofs, F. Klein, D. Lehnert, M. Bastmeyer, and U. S. Schwarz. Filamentous network mechanics and active contractility determine cell and tissue shape. *Biophysical Journal*, 95(7):3488–3496, 2008. 17, 18
- [99] R. A. Foty, C. M. Pfleger, G. Forgacs, and M. S. Steinberg. Surface tensions of embryonic tissues predict their mutual envelopment behavior. *Development*, 122(5):1611–1620, 1996. 17, 62, 64
- [100] K. Jakab, A. Neagu, V. Mironov, R. R. Markwald, and G. Forgacs. Engineering biological structures of prescribed shape using self-assembling multicellular systems. *Proceedings of the National Academy of Sciences*, 101(9):2864–2869, 2004. 17, 62
- [101] S. Douezan, K. Guevorkian, R. Naouar, S. Dufour, D. Cuvelier, and F. Brochard-Wyart. Spreading dynamics and wetting transition of cellular aggregates. *Proceedings of the National Academy of Sciences*, 108(18):7315–7320, 2011. 17, 18, 43
- [102] K. Guevorkian, M. J. Colbert, M. Durth, S. Dufour, and F. Brochard-Wyart. Aspiration of biological viscoelastic drops. *Physical Review Letters*, 104(21):218101, 2010. 17
- [103] R. Winklbauer. Dynamic cell-cell adhesion mediated by pericellular matrix interaction - A hypothesis. *Journal of Cell Science*, 132(16):jcs231597, 2019. 17, 93

-
- [104] T. Lecuit and P. Lenne. Cell surface mechanics and the control of cell shape, tissue patterns and morphogenesis. *Nature Reviews Molecular Cell Biology*, 8(8):633, 2007. 17, 43
 - [105] C. Pérez-González, R. Alert, C. Blanch-Mercader, M. Gómez-González, T. Kolodziej, E. Bazellieres, J. Casademunt, and X. Trepát. Active wetting of epithelial tissues. *Nature Physics*, 15(1):79, 2019. 17, 64, 84
 - [106] C. E. Caicedo-Carvajal, T. Shinbrot, and R. A. Foty. $\alpha_5\beta_1$ integrin-fibronectin interactions specify liquid to solid phase transition of 3D cellular aggregates. *PloS One*, 5(7):e11830, 2010. 18
 - [107] M. Rumpler, A. Woesz, J. W. Dunlop, J. T. Van Dongen, and P. Fratzl. The effect of geometry on three-dimensional tissue growth. *Journal of the Royal Society Interface*, 5(27):1173–1180, 2008. 18
 - [108] S. Ehrig, B. Schamberger, C. M. Bidan, A. West, C. Jacobi, K. Lam, P. Kollmannsberger, A. Petersen, P. Tomancak, K. Kommareddy, F. D. Fischer, P. Fratzl, and J. W. Dunlop. Surface tension determines tissue shape and growth kinetics. *Science Advances*, 5(9):1–9, 2019. 18, 62
 - [109] T. B. Saw, W. Xi, B. Ladoux, and C. T. Lim. Biological tissues as active nematic liquid crystals. *Advanced Materials*, 30(47):1802579, 2018. 18
 - [110] J. P. Garrahan. Dynamic heterogeneity comes to life. *Proceedings of the National Academy of Sciences*, 108(12):4701–4702, 2011. 18
 - [111] S. Garcia, E. Hannezo, J. Elgeti, J. F. Joanny, P. Silberzan, and N. S. Gov. Physics of active jamming during collective cellular motion in a monolayer. *Proceedings of the National Academy of Sciences*, 112(50):15314–15319, 2015. 18
 - [112] D. Bi, J. H. Lopez, J. M. Schwarz, and M. L. Manning. A density-independent rigidity transition in biological tissues. *Nature Physics*, 11(12):1074–1079, 2015. 18
 - [113] D. Bi, X. Yang, M. C. Marchetti, and M. L. Manning. Motility-driven glass and jamming transitions in biological tissues. *Physical Review X*, 6(2):1–13, 2016. 18
 - [114] J. A. Mitchel, A. Das, M. J. O’Sullivan, I. T. Stancil, S. J. DeCamp, S. Koehler, O. H.

- Ocaña, J. P. Butler, J. J. Fredberg, M. A. Nieto, D. Bi, and J.-A. Park. In primary airway epithelial cells, the unjamming transition is distinct from the epithelial-to-mesenchymal transition. *Nature Communications*, 11:5053, 2020. 18, 71
- [115] P. Kollmannsberger, C. M. Bidan, J. W. C. Dunlop, and P. Fratzl. The physics of tissue patterning and extracellular matrix organisation: How cells join forces. *Soft Matter*, 7(20):9549–9560, 2011. 18
- [116] R. Alert and X. Trepat. Physical models of collective cell migration. *Annual Review of Condensed Matter Physics*, 11(1):77–101, 2020. 18
- [117] E. Ban, H. Wang, J. M. Franklin, J. T. Liphardt, P. A. Janmey, and V. B. Shenoy. Strong triaxial coupling and anomalous Poisson effect in collagen networks. *Proceedings of the National Academy of Sciences*, 116(14):6790–6799, 2019. 19
- [118] A. S. Abhilash, B. M. Baker, B. Trappmann, C. S. Chen, and V. B. Shenoy. Remodeling of fibrous extracellular matrices by contractile cells: Predictions from discrete fiber network simulations. *Biophysical Journal*, 107(8):1829–1840, 2014. 19
- [119] H. Jia, E. Mailand, J. Zhou, Z. Huang, G. Dietler, J. M. Kolinski, X. Wang, and M. S. Sakar. Universal Soft Robotic Microgripper. *Small*, 15(4):1–8, 2019. 22, 35
- [120] E. Garreta, R. D. Kamm, S. M. Chuva de Sousa Lopes, M. A. Lancaster, R. Weiss, X. Trepat, I. Hyun, and N. Montserrat. Rethinking organoid technology through bioengineering. *Nature Materials*, 20(2):145–155, 2020. 23
- [121] D. Huh, B. D. Matthews, A. Mammoto, M. Montoya-Zavala, H. Y. Hsin, and D. E. Ingber. Reconstituting organ-level lung functions on a chip. *Science*, 328(5986):1662–8, 2010. 23
- [122] N. Brandenburg, S. Hoehnel, F. Kuttler, K. Homicsko, C. Ceroni, T. Ringel, N. Gjorevski, G. Schwank, G. Coukos, G. Turcatti, and M. P. Lutolf. High-throughput automated organoid culture via stem-cell aggregation in microcavity arrays. *Nature Biomedical Engineering*, 4(9):863–874, 2020. 23
- [123] T. Leal Ghezzi and O. Campos Corleta. 30 Years of Robotic Surgery. *World Journal of Surgery*, 40(10):2550–2557, 2016. 23

- [124] A. Edelstein, N. Amodaj, K. Hoover, R. Vale, and N. Stuurman. Computer control of microscopes using manager. *Current Protocols in Molecular Biology*, (92):1–17, 2010. 24
- [125] H. Pinkard, N. Stuurman, and L. Waller. Pycro-manager: Open-source software for integrated microscopy hardware control and image processing. *arXiv*, 2006.11330, 2020. 24, 26
- [126] M. Thomas, B. Ladoux, and Y. Toyama. Desmosomal junctions govern tissue integrity and actomyosin contractility in apoptotic cell extrusion. *Current Biology*, 30(4):682–690, 2020. 24
- [127] K. Jewhurst, M. Levin, and K. A. McLaughlin. Optogenetic control of apoptosis in targeted tissues of *Xenopus laevis* embryos. *Journal of Cell Death*, 7:25–31, 2014. 24
- [128] K. Makhijani, T. L. To, R. Ruiz-González, C. Lafaye, A. Royant, and X. Shu. Precision Optogenetic Tool for Selective Single- and Multiple-Cell Ablation in a Live Animal Model System. *Cell Chemical Biology*, 24(1):110–119, 2017. 24
- [129] M. Nambi, P. S. Bernstein, and J. J. Abbott. A compact telemanipulated retinal-surgery system that uses commercially available instruments with a quick-change adapter. *Journal of Medical Robotics Research*, 1(2):1630001, 2016. 25
- [130] J. Kolega. Phototoxicity and photoinactivation of blebbistatin in uv and visible light. *Biochemical and Biophysical Research Communications*, 320(3):1020–1025, 2004. 31, 56, 92
- [131] A. Mikulich, S. Kavaliauskiene, and P. Juzenas. Blebbistatin, a myosin inhibitor, is phototoxic to human cancer cells under exposure to blue light. *Biochimica et Biophysica Acta - General Subjects*, 1820(7):870–877, 2012. 31, 92
- [132] A. Kumar, Y. Wu, R. Christensen, P. Chandris, W. Gandler, E. McCreedy, A. Bokinsky, D. A. Colón-Ramos, Z. Bao, M. McAuliffe, G. Rondeau, and H. Shroff. Dual-view plane illumination microscopy for rapid and spatially isotropic imaging. *Nature Protocols*, 9(11):2555–2573, 2014. 32
- [133] L. Valon, A. Marin-Llaurado, T. Wyatt, G. Charras, and X. Trepatt. Optogenetic control

- of cellular forces and mechanotransduction. *Nature communications*, 8:14396, 2017. 36, 37, 38, 39
- [134] G. Guglielmi, H. J. Falk, and S. De Renzis. Optogenetic Control of Protein Function: From Intracellular Processes to Tissue Morphogenesis. *Trends in Cell Biology*, 26(11):864–874, 2016. 36
- [135] L. R. Polstein and C. A. Gersbach. A light-inducible CRISPR-Cas9 system for control of endogenous gene activation. *Nature Chemical Biology*, 11(3):198–200, 2015. 36, 39
- [136] S. Lee, H. Park, T. Kyung, N. Y. Kim, S. Kim, J. Kim, and W. D. Heo. Reversible protein inactivation by optogenetic trapping in cells. *Nature methods*, 11(6):633–636, 2014. 36, 38, 39
- [137] E. Wagner and M. Glotzer. Local RhoA activation induces cytokinetic furrows independent of spindle position and cell cycle stage. *Journal of Cell Biology*, 213(6):641–649, 2016. 39
- [138] E. Mailand, B. Li, J. Eyckmans, N. Bouklas, and M. S. Sakar. Surface and bulk stresses drive morphological changes in fibrous microtissues. *Biophysical Journal*, 117(5):975–986, 2019. 42
- [139] J. Kim, E. Mailand, I. Ang, M. S. Sakar, and N. Bouklas. A model for 3D deformation and reconstruction of contractile microtissues. *Soft Matter*, 2020. 42
- [140] P. Martin and S. M. Parkhurst. Parallels between tissue repair and embryo morphogenesis. *Development*, 131(13):3021–3034, 2004. 43
- [141] A. J. Singer and R. A. Clark. Cutaneous wound healing. *New England Journal of Medicine*, 341(10):738–746, 1999. 43
- [142] S. a. Guo and L. A. DiPietro. Factors affecting wound healing. *Journal of Dental Research*, 89(3):219–229, 2010. 43
- [143] S. Münster, L. M. Jawerth, B. A. Leslie, J. I. Weitz, B. Fabry, and D. A. Weitz. Strain history dependence of the nonlinear stress response of fibrin and collagen networks. *Proceedings of the National Academy of Sciences*, 110(30):12197–12202, 2013. 43

- [144] S. Nam, K. H. Hu, M. J. Butte, and O. Chaudhuri. Strain-enhanced stress relaxation impacts nonlinear elasticity in collagen gels. *Proceedings of the National Academy of Sciences*, 113(20):5492–5497, 2016. 43
- [145] M. S. Sakar, J. Eyckmans, R. Pieters, D. Eberli, B. J. Nelson, and C. S. Chen. Cellular forces and matrix assembly coordinate fibrous tissue repair. *Nature Communications*, 7:11036, 2016. 43, 66
- [146] K. J. Sonnemann and W. M. Bement. Wound repair: Toward understanding and integration of single-cell and multicellular wound responses. *Annual Review of Cell and Developmental Biology*, 27:237–263, 2011. 43
- [147] T. J. Shaw and P. Martin. Wound repair: a showcase for cell plasticity and migration. *Current Opinion in Cell Biology*, 42:29–37, 2016. 43
- [148] R. A. Foty, G. Forgacs, C. M. Pfleger, and M. S. Steinberg. Liquid properties of embryonic tissues: measurement of interfacial tensions. *Physical Review Letters*, 72(14):2298–2301, 1994. 43
- [149] D. Gonzalez-Rodriguez, K. Guevorkian, S. Douezan, and F. Brochard-Wyart. Soft matter models of developing tissues and tumors. *Science*, 338(6109):910–917, 2012. 43
- [150] P. L. Ryan, R. A. Foty, J. Kohn, and M. S. Steinberg. Tissue spreading on implantable substrates is a competitive outcome of cell–cell vs. cell–substratum adhesivity. *Proceedings of the National Academy of Sciences*, 98(8):4323–4327, 2001. 43
- [151] G. Beaune, T. V. Stirbat, N. Khalifat, O. Cochet-Escartin, S. Garcia, V. V. Gurchenkov, M. P. Murrell, S. Dufour, D. Cuvelier, and F. Brochard-Wyart. How cells flow in the spreading of cellular aggregates. *Proceedings of the National Academy of Sciences*, 111(22):8055–8060, 2014. 43
- [152] R. W. Style, A. Jagota, C.-Y. Hui, and E. R. Dufresne. Elastocapillarity: Surface tension and the mechanics of soft solids. *Annual Review of Condensed Matter Physics*, 8:99–118, 2017. 43, 55, 64, 84

- [153] J. Bico, É. Reyssat, and B. Roman. Elastocapillarity: When surface tension deforms elastic solids. *Annual Review of Fluid Mechanics*, 50:629–659, 2018. 43, 55, 64
- [154] A. Zemel, I. Bischofs, and S. Safran. Active elasticity of gels with contractile cells. *Physical Review Letters*, 97(12):128103, 2006. 43
- [155] E. A. Sander, T. Stylianopoulos, R. T. Tranquillo, and V. H. Barocas. Image-based multi-scale modeling predicts tissue-level and network-level fiber reorganization in stretched cell-compacted collagen gels. *Proceedings of the National Academy of Sciences*, 106(42):17675–17680, 2009. 43, 62
- [156] A. Abhilash, B. M. Baker, B. Trappmann, C. S. Chen, and V. B. Shenoy. Remodeling of fibrous extracellular matrices by contractile cells: predictions from discrete fiber network simulations. *Biophysical Journal*, 107(8):1829–1840, 2014. 43, 62
- [157] P. Ronceray, C. P. Broedersz, and M. Lenz. Fiber networks amplify active stress. *Proceedings of the National Academy of Sciences*, 113(11):2827–2832, 2016. 43
- [158] J. Feng, H. Levine, X. Mao, and L. M. Sander. Nonlinear elasticity of disordered fiber networks. *Soft Matter*, 12(5):1419–1424, 2016. 43
- [159] W. R. Legant, C. S. Chen, and V. Vogel. Force-induced fibronectin assembly and matrix remodeling in a 3d microtissue model of tissue morphogenesis. *Integrative Biology*, 4(10):1164–1174, 2012. 44, 63
- [160] J. Foolen, J.-Y. Shiu, M. Mitsi, Y. Zhang, C. S. Chen, and V. Vogel. Full-length fibronectin drives fibroblast accumulation at the surface of collagen microtissues during cell-induced tissue morphogenesis. *PloS One*, 11(8):e0160369, 2016. 44, 63
- [161] P. Steinmann. On boundary potential energies in deformational and configurational mechanics. *Journal of the Mechanics and Physics of Solids*, 56(3):772–800, 2008. 44
- [162] A. Javili and P. Steinmann. A finite element framework for continua with boundary energies. part i: the two-dimensional case. *Computer Methods in Applied Mechanics and Engineering*, 198(27-29):2198–2208, 2009. 44, 46

- [163] A. Logg, K.-A. Mardal, G. N. Wells, et al. *Automated Solution of Differential Equations by the Finite Element Method*. Springer, 2012. 52
- [164] M. S. Alnæs, J. Blechta, J. Hake, A. Johansson, B. Kehlet, A. Logg, C. Richardson, J. Ring, M. E. Rognes, and G. N. Wells. The fenics project version 1.5. *Archive of Numerical Software*, 3(100):9–23, 2015. 52
- [165] T. Wakatsuki, M. S. Kolodney, G. I. Zahalak, and E. L. Elson. Cell mechanics studied by a reconstituted model tissue. *Biophysical Journal*, 79(5):2353–2368, 2000. 52
- [166] V. S. Deshpande, R. M. McMeeking, and A. G. Evans. A bio-chemo-mechanical model for cell contractility. *Proceedings of the National Academy of Sciences*, 103(38):14015–14020, 2006. 52
- [167] R. Zhao, T. Boudou, W.-G. Wang, C. S. Chen, and D. H. Reich. Decoupling cell and matrix mechanics in engineered microtissues using magnetically actuated microcantilevers. *Advanced Materials*, 25(12):1699–1705, 2013. 52, 93
- [168] A. F. Mertz, S. Banerjee, Y. Che, G. K. German, Y. Xu, C. Hyland, M. C. Marchetti, V. Horsley, E. R. Dufresne, et al. Scaling of traction forces with the size of cohesive cell colonies. *Physical Review Letters*, 108(19):198101, 2012. 64
- [169] P. W. Oakes, S. Banerjee, M. C. Marchetti, and M. L. Gardel. Geometry regulates traction stresses in adherent cells. *Biophysical Journal*, 107(4):825–833, 2014. 64
- [170] R. Vincent, E. Bazellères, C. Pérez-González, M. Uroz, X. Serra-Picamal, and X. Trepat. Active tensile modulus of an epithelial monolayer. *Physical Review Letters*, 115(24):248103, 2015. 64
- [171] B. M. Baker, B. Trappmann, W. Y. Wang, M. S. Sakar, I. L. Kim, V. B. Shenoy, J. A. Burdick, and C. S. Chen. Cell-mediated fibre recruitment drives extracellular matrix mechanosensing in engineered fibrillar microenvironments. *Nature Materials*, 14(12):1262–1268, 2015. 64
- [172] H. Ehrlich. Wound closure: Evidence of cooperation between fibroblasts and collagen matrix. *Eye*, 2(2):149–157, 1988. 64

- [173] S. Nam, J. Lee, D. G. Brownfield, and O. Chaudhuri. Viscoplasticity enables mechanical remodeling of matrix by cells. *Biophysical Journal*, 111(10):2296–2308, 2016. 65
- [174] J. Kim, J. Feng, C. A. Jones, X. Mao, L. M. Sander, H. Levine, and B. Sun. Stress-induced plasticity of dynamic collagen networks. *Nature Communications*, 8:842, 2017. 65
- [175] J. Laurent, G. Blin, F. Chatelain, V. Vanneaux, A. Fuchs, J. Larghero, and M. Théry. Convergence of microengineering and cellular self-organization towards functional tissue manufacturing. *Nature Biomedical Engineering*, 1(12):939–956, 2017. 71
- [176] J. Ranft, M. Basan, J. Elgeti, J.-F. Joanny, J. Prost, and F. Julicher. Fluidization of tissues by cell division and apoptosis. *Proceedings of the National Academy of Sciences*, 107(49):20863–20868, 2010. 71
- [177] T. Savin, N. A. Kurpios, A. E. Shyer, P. Florescu, H. Liang, L. Mahadevan, and C. J. Tabin. On the growth and form of the gut. *Nature*, 476(7358):57–63, 2011. 71
- [178] J. D. Dukes, P. Whitley, and A. D. Chalmers. The MDCK variety pack: Choosing the right strain. *BMC Cell Biology*, 12:2–5, 2011. 74
- [179] H. Peinado, M. Quintanilla, and A. Cano. Transforming growth factor β -1 induces Snail transcription factor in epithelial cell lines. Mechanisms for epithelial mesenchymal transitions. *Journal of Biological Chemistry*, 278(23):21113–21123, 2003. 83
- [180] W. Thielicke and E. J. Stamhuis. PIVlab – Towards User-friendly, Affordable and Accurate Digital Particle Image Velocimetry in MATLAB. *Journal of Open Research Software*, 2:e30, 2014. 87
- [181] Y. Sasai. Cytosystems dynamics in self-organization of tissue architecture. *Nature*, 493(7432):318–326, 2013. 89
- [182] P. Li, Z. Yang, and S. Jiang. Needle-tissue interactive mechanism and steering control in image-guided robot-assisted minimally invasive surgery: A review. *Medical and Biological Engineering and Computing*, 56(6):931–949, 2018. 91
- [183] R. D. King, J. Rowland, S. G. Oliver, M. Young, W. Aubrey, E. Byrne, M. Liakata, M.

- Markham, P. Pir, L. N. Soldatova, A. Sparkes, K. E. Whelan, and A. Clare. The automation of science. *Science*, 324(5923):85–89, 2009. 91
- [184] J. Zhong, J. Riordon, T. C. Wu, H. Edwards, A. R. Wheeler, K. Pardee, A. Aspuru-Guzik, and D. Sinton. When robotics met fluidics. *Lab on a Chip*, 20(4):709–716, 2020. 91
- [185] L. Kowalik and J. K. Chen. Illuminating developmental biology through photochemistry. *Nature Chemical Biology*, 13(6):587–598, 2017. 92
- [186] H. M. Lee, D. R. Larson, and D. S. Lawrence. Illuminating the chemistry of life: Design, synthesis, and applications of ”caged” and related photoresponsive compounds. *ACS Chemical Biology*, 4(6):409–427, 2009. 92
- [187] Q. Xu, K. E. Jensen, R. Boltyanskiy, R. Sarfati, R. W. Style, and E. R. Dufresne. Direct measurement of strain-dependent solid surface stress. *Nature Communications*, 8:555, 2017. 93
- [188] C. Kyprianou, N. Christodoulou, R. S. Hamilton, W. Nahaboo, D. S. Boomgaard, G. Amadei, I. Migeotte, and M. Zernicka-Goetz. Basement membrane remodelling regulates mouse embryogenesis. *Nature*, 582(7811):253–258, 2020. 93
- [189] L. A. Taber. Morphomechanics: Transforming tubes into organs. *Current Opinion in Genetics and Development*, 27:7–13, 2014. 94
- [190] C. Appiah, C. Arndt, K. Siemsen, A. Heitmann, A. Staubitz, and C. Selhuber-Unkel. Living Materials Herald a New Era in Soft Robotics. *Advanced Materials*, 31(36):1807747, 2019. 94
- [191] D. Shah, B. Yang, S. Kriegman, M. Levin, J. Bongard, and R. Kramer-Bottiglio. Shape Changing Robots: Bioinspiration, Simulation, and Physical Realization. *Advanced Materials*, 2002882, 2020. 94

Erik Mailand

Date of Birth: February 7, 1989
Nationality: Swiss and German

Email: mailand.erik@gmail.com

[LinkedIn](#) [Google Scholar](#)

Core Experience

- | | |
|-------------------|--|
| Apr 2016-Present | Doctoral Thesis at MicroBioRobotics Systems Laboratory (MICROBS) EPFL, Lausanne CH
“Mechanical principles of engineering fibrous tissues with programmable shape” Advisor: Prof. Mahmut Selman Sakar <ul style="list-style-type: none">• Development of methodology to study and engineer fibrous tissue shaping |
| Jan 2016-Mar 2016 | Assistant at High Power & High Voltage Laboratories. ABB, Baden CH <ul style="list-style-type: none">• Software development for temperature and pressure measurement instruments |
| Jul 2015-Dec 2015 | Intern at Laboratory for Biointerfaces, Biomolecules at Surfaces, EMPA, St. Gallen CH <ul style="list-style-type: none">• Recombinant engineering and production of proteins in E. coli for the biological functionalization of artificial hydrogels |
| Jun 2014-Nov 2014 | Master’s Thesis at Synthetic Biology Group. ETH Zurich, Basel CH
“Transplantation Of Prokaryotic Two-Component Signaling Pathways Into Mammalian Cells and Massive Parallel Transcription Factor Binding Site Screening” Advisor: Prof. Dr. Yaakov Benenson <ul style="list-style-type: none">• Protein mutation and localization, gene circuit optimization, transcription factor activity investigation and high- throughput DNA sequencing in two separate projects |

Education

- | | |
|-------------------|--|
| Apr 2016-Present | Doctoral Assistant, EPFL, Lausanne CH
Institute of Mechanical Engineering |
| Sep 2013-Jun 2015 | Master of Science ETH in Biotechnology, ETH Zurich, Basel CH
Department of Biosystems Science and Engineering, Major: Biotechnology |
| Sep 2010-Aug 2013 | Bachelor of Science ETH in Biotechnology, ETH Zurich, Basel CH
3 rd year Bachelor in Biotechnology, ETH Zurich, Basel CH
1 st and 2 nd year Bachelor in Biology, University of Zurich, Zurich CH |

Additional Education

2010-2014	Teaching guitar in private lessons, Zurich and Basel, CH
2010	Trimester in Master Performance Course at Tech Music School, London UK
2007	J&S 1 and 2 leadership training for snowboarding, Arosa CH

Interests and Activities

Music (guitar, piano, bass guitar), Snowboarding, Basketball, Climbing

Peer-reviewed Publications

Mailand, E., Li, B., Eyckmans, J., Bouklas, N. & Sakar, M. S. Surface and bulk stresses drive morphological changes in fibrous microtissues. *Biophys. J.* 117, 975–986 (2019).

Kim, J., **Mailand, E.**, Ang, I., Sakar, M. S. & Bouklas, N. A model for 3D deformation and reconstruction of contractile microtissues. *Soft Matter* (2020).

Jia, H., **Mailand, E.**, Zhou, J., Huang, Z., Dietler, G., Kolinski, J. M., Wang, X. & Sakar, M. S. Universal Soft Robotic Microgripper. *Small* 15, 1–8 (2019).

Faccio, G., Cont, A., **Mailand, E.**, Zare-Eelanjegh, E., Malini, R.I., Maniura-Weber, K., Rossi, R. M. & Spano, F. Complete inclusion of bioactive molecules and particles in polydimethylsiloxane: a straightforward process under mild conditions. *Sci. Rep.* 9, 1–8 (2019).

Angelici, B., **Mailand, E.**, Haefliger, B. & Benenson, Y. Synthetic Biology Platform for Sensing and Integrating Endogenous Transcriptional Inputs in Mammalian Cells. *Cell Rep.* 16, 2525–2537 (2016).

Hansen, J., **Mailand, E.**, Swaminathan, K. K., Schreiber, J., Angelici, B. & Benenson, Y. Transplantation of prokaryotic two-component signaling pathways into mammalian cells. *Proc. Natl. Acad. Sci.* 111, 15705–15710 (2014).

Oral and Poster Communications

Oral Presentation. APS March Meeting 2020 “Surface Stresses Drive Morphological Changes in Three-Dimensional Microtissues”	Denver, US, 2020
Oral Presentation. SSBE 2018 “A robotic platform to study mechanobiology of fibrous tissue reconstruction”	Biel, CH, 2018
Oral Presentation. Frontiers 2016 “Microfabricated platforms to study and control tissue architecture”	Lausanne, CH, 2016
Poster. BMES 2018 “A robotic platform to study mechanobiology of fibrous tissue reconstruction”	Atlanta, US, 2018
Poster. Engineering Multicellular Self-Organization 2017 “Micromanipulation platform to study and control tissue mechanics”	Lausanne, CH, 2017
Poster. EMBL Workshop “Non-Neuronal Optogenetics “ “Micromanipulation platform to study and control tissue mechanics”	Heidelberg, DE, 2017